博士論文

論文題目　　　Concept of magnetic artificial molecules by exploiting

particle-like spin dynamics of coupled vortex structures

（連結磁気渦構造における粒子的スピンダイナミクスを用いた磁気人工

分子のコンセプト）

氏　　名　　　杉本　聡志

Concept of magnetic artificial molecules by exploiting particle-like spin dynamics of coupled vortex structures

Satoshi Sugimoto

The University of Tokyo

2014

Advisory Committee:

Prof. Dr. Y. Otani, Chair/Advisor

Prof. Dr. C. Marrows

Prof. Dr. T. Ono

Ass. Prof. Dr. T. Okamoto

Ass. Prof. Dr. T. Masuda

Abstract

Satoshi Sugimoto, Doctor of Philosophy

The University of Tokyo, 2014

Supervisor: Prof. Y. Otani

In this thesis, collective magnetization dynamics written in a sentence of a quasiparticle motion on magnetic vortex structure are investigated with an attempt to construct novel magnetic artificial molecules. Frequency domain measurement using Spin torque diode sensor and time domain measurement exploiting magneto-optical Kerr effect are applied to detect nanosecond time scale of micro- and nanostructures.

A focus is put on the understanding of the stray field mediated coupling between neighboring ferromagnetic structures and its influence on the magnetization dynamics. The gyrotropic motion of vortices in pairs, and chains of coupled disk-shaped structures is investigated. Resonant spectra of rectified voltage reveal the interacting vortices behave as coupled harmonic oscillators and an analogy with rotating induced dipoles in the interacting energy. Furthermore, the energy scheme of such coupled vortices can be systematically tuned by operating two independent magnetization structure of a vortex: standing magnetization configuration at the center region, polarity, and in-plane circularly curling magnetization, chirality. These two parameters are originally degenerated in single magnetic vortex. The chirality dependence is also mechanically complemented by coordinating rotation phases of coupled cores. Coupled cores are mutually locked and number of degrees of phase difference is decided by total number of coupled vortices. Infinite length 1 dimensional vortex chain shows finite bandwidth in its dispersion relation and it can be somehow modified by changing configuration of polarities. Beside, shape of band structure is also changed by chirality combination. A rich tunablity of coupled vortices is unique as a model system and may be adoptable as an alternative method of frequency design on future spintronics devices.

Table of Contents

1.   Introduction

Magnetism is one of the most fundamental phenomena in natural science, and has been used many animal species in natural world, several birds directly sense the magnetic field of the earth for orientation via magnetoreception[1]. We human species have variously used this phenomena for a long time, from most primitive lock mechanism of the door and magnetic compass, to current labeling of cells via magnetic nanoparticles[2,3], magnetic resonance imaging[4] and so on. Recent rapid progress of nano-fabrication has paved new ways for magnetism, and enabled us to discuss previously hidden parameter in conduction phenomena in electronics, spin of electrons. The spintronics is worth to be said one of the hottest topic in modern science in past two decades. Especially in the applicational area, the dynamic properties of ferromagnetic micro- and nanostructures have gained a broad scientific interest: concepts of high-density and ultrafast nonvolatile data storage devices[5,6], information-signal processing devices[7,8], logical units[9,10], and microwave emission sources[11,12]. Dynamics properties are strongly affected by magnetization configuration, and the magnetic vortex configuration[13,14] is known to show unique properties in its collective dynamics among various types of magnetic domains. Magnetic vortex possesses a low frequency mode approximated as "dynamics of a rigid quasiparticle in a parabolic potential"[15,16] and its spatial symmetry is reversed by changing a part of magnetization structure core polarization. These features are unique for a model system, and various proposals of vortex used novel type of spintronics devices have been proposed[17,11,18,19,20]. Among them, stray field mediated interaction between neighboring vortices directly reflect on this switchable spatial symmetry[21,22,23], and can be used for artificial molecules exploiting spin wave propagation, so called magnonic crystal[24,25,26,27].

  This thesis summarizes my experimental work on constructing new type of magnetic artificial molecules via coupling collective magnetization dynamics of vortex structure during the past three years. Targeted materials lies in sub-micron scale in diameter and several tens of nanometers in thickness and its equilibrium magnetization configuration and dynamics can be described starting from semi-classical magnetism. In chapter 2, the theoretical background required for the understanding of the experiments is given. In chapter 3, the different measurement set ups and the techniques used for sample fabrication are introduced. All samples have been fabricated using the clean-room facilities at the Institute for Solid State Physics, University of Tokyo or Nanoscience Laboratory, Center for Emergent Matter Science, RIKEN. Two complementary methods, namely, measurements of spin torque diode effect[28,29] and time resolved magneto-optical Kerr effect[30] have been employed to study the magnetization dynamics in frequency domain and time domain, respectively. Besides studies dynamics process, direct imaging by magnetic force microscopy[13] and hysteresis loops measurement[31] are also used to gain information about the remanent state of magnetization configuration.

A main focus of the work is put on the understanding of the coupling mechanism due to stray field mediated interaction between neighboring ferromagnetic structures and its influence on the

magnetization dynamics. Disk-shaped structures with the vortex magnetization configuration are investigated. Chapter 4 of this thesis deals with development of electrical frequency sensor and magneto-optical Kerr magnetometer for detecting the gyroscopic motion of isolated vortices. On their specific time and length scales, the samples reveal characteristics known from other fundamental physical systems, theoretically introduced in chapter 2.

In chapter 5, the resonant mode in a pair of neighboring magnetic vortices with sub-micron meter in its interval distance is studied using techniques developed in chapter 4. 4 different alignments of frequency domain measurements have been investigated to obtained total insights of relations between energy scheme of coupled system and selection of vortex characteristics, polarity and chirality. The findings also show analogy with real diatomic molecules in energy scheme and form the basis for chapter 6.

Finally, chapter 6 deals with 1 dimensionally coupled system, starting from experimental demonstration for 3 chained vortices and the general form of dispersion relationship is analytically discussed.

The thesis closes with a conclusion in chapter 7.

2. Theoretical Background

This chapter deals with the theoretical background required for the experiments presented in the chapters 4 - 6. In Sec. 2.1, a brief discussion for the quantum-mechanical origin of ferromagnetism is given and the relevant magnetic field vectors are introduced. In Sec. 2.2, details of magnetostatic energy contributions and approaches to find distinct role in the formation of the equilibrium magnetization configuration are discussed, subsequently Section 2.3 deals with the concept of magnetic charges to describe the internal demagnetization field and external stray field of a ferromagnetic body. In Sec. 2.4, the general from of dynamics of the magnetization, described using the Landau-Lifshitz-Gilbert equation, including the concept of spin transfer torque is introduced. Next, short insight of anisotropic magnetoresistance is introduced in Sec. 2.5. In Sec. 2.6, the magnetic vortex is discussed in sentences of Sec. 2.1-2.4, focusing on the low frequency mode where the magnetization dynamics in vortex structures are treated as motion of rigid quasiparticle. The stray field mediated neighboring effect between separate magnetic vortices is numerically discussed in Sec. 2.7. Finally, Sec. 2.8 deals with magnon mediated artificial molecules, i.e. magnonic crystal and briefly introduce the concept of the vortex used magnonic crystal.

2.1. Fundamentals in ferromagnetism

Origin of the ferromagnetism

Ferromagnets exhibit a parallel alignment of spins in so called ferromagnetic domains in the absence of the external field, and it leads to a net magnetic moment as finite amplitude within these regions. A basic understanding of the theoretical description of ferromagnetism can be imparted regarding a two-electron system. According to the Pauli exclusion principle, the two electrons cannot be in identical quantum states which mean that the complete wave function of the system must be anti-symmetric. Thus the spins of the electrons must be antiparallel to satisfy this condition or vice versa. The electrostatic repulsion is smaller when the electrons are further apart from each other. In the case of ferromagnetic coupling the reduction in Coulomb energy is larger than the increase of kinetic energy due to the occupation of a different spatial quantum state. Thus, a parallel alignment of the spins is energetically favourable. The energy splitting between the two states with parallel and antiparallel spin alignment is called exchange energy. Based on the concept energetically preferred parallel alignment of the spins, the Heisenberg model with the effective Heisenberg Hamiltonian is written as

$$H_{eff} = -2 \sum_{i<J}^{N} J_{ij} \hat{s}_i \hat{s}_J \qquad (2.1)$$

for a many-electron system can be established[32]. Here, $\hat{s}_{i,j}$ are the spin operators and J_{ij} is the exchange integral depending on the distance between the electrons and the overlap of their wave functions. J_{ij} describes the energy splitting between parallel and antiparallel spin alignment and its sign decides the type of magnetic coupling, i.e. positive for ferromagnetic coupling and negative for antiferromagnetic coupling. Only the nearest neighbours significantly contribute to the exchange integral.

In this work, permalloy ($Ni_{80}Fe_{20}$) is practically investigated. The *3d* valence electrons of the ferromagnetic transition metals iron and nickel are localized strong enough to generate a substantial magnetic moment. In addition, the bonding interaction between the neighbouring 3d electrons causes the formation of an energy band. This is taken into account in the Stoner model illustrated in Fig. 2.1 (a). The exchange interaction leads to an energy shift between the bands of the two spin configuration and the difference in electron population results in the finite magnetic moment in total. The minority of spins points in the direction of the magnetization M considering the opposite directions of spin and spin magnetic moment in the quantum mechanical expression $m_s = -\gamma s$ with the gyromagnetic ratio

$\gamma = \frac{ge}{2m_e} = 1.76 \times 10^{11}$ s^{-1}T^{-1}. Here, $e = 1.602 \times 10^{-19}$As is the electron charge, $m_e = 9.109 \times 10^{-31}$kg

is the electron mass, and $g \approx 2$ is the Landé factor.

Magnetic fields, Magnetization, and magnetic hysteresis

The magnetic induction in the presence of a magnetic field H is given by $B = \mu_0 H$ with the vacuum permeability in vacuum $\mu_0 = 4\pi \times 10^{-7}$VsA^{-1}m^{-1}. The magnetization M is introduced which is defined as the density of magnetic moments per volume. The above relation then reads

$$B = \mu_0(H + M) \tag{2.2}$$

where $M = \chi H$ and χ is the magnetic susceptibility tensor depending on the strength, the direction of the applied field H, and also the history of magnetic field that the ferromagnet has been exposed to. The absolute value of the magnetization in each unit of volume of the material is equal to the saturation magnetization M_S. This material dependent constant is lowered with increasing temperature and the ferromagnetic phase vanishes due to thermal agitation above the Curie temperature T_C. For permalloy a common value of the saturation magnetization is $M_S = 8.6 \times 10^5$ Am^{-1}[33] and the Curie temperature is $T_C \approx 833$ K[34]. In this thesis, all measurements have been performed at room temperature and any thermal effects are finally neglected.
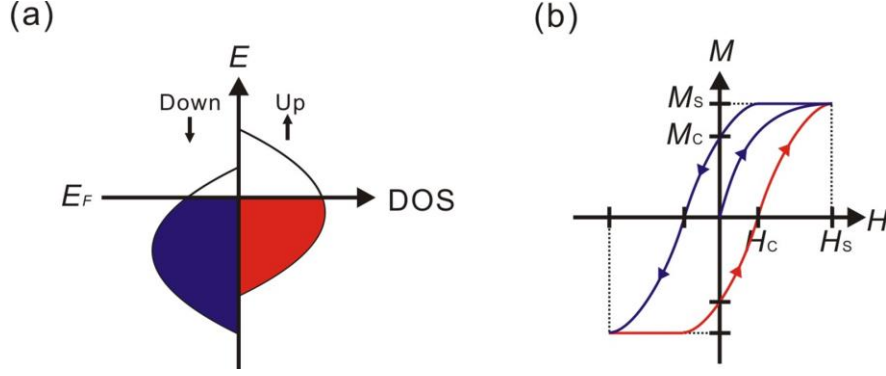
FIG. 2.1: (a) Cartoon of the Stoner model for the $3d$ shell of ferromagnetic transition metals. Filled electron states below the Fermi energy E_F are shown shaded by red and blue colors and empty states above E_F are shown unshaded. The minority spins point in the direction of the magnetization $\boldsymbol{M}$. (b) Schematic hysteresis loop of a ferromagnetic sample. Arrows indicate the sweep direction of the external magnetic field $\boldsymbol{H}$.

Also below the Curie temperature ferromagnets can have a zero net magnetization $\boldsymbol{M}$ when the magnetic moments of the single domains cancel out each other. An increasing external magnetic field causes the magnetic moments to gradually point in the field direction. Figure 2.1(b) shows a typical form of hysteresis loop of a ferromagnetic sample. The net magnetization increases until all magnetic moments are aligned parallel which corresponds to $|\boldsymbol{M}| = M_\mathrm{S}$. Increasing the external field beyond the saturation field H_S does not lead to a further increase of the magnetization. After switching off the external field, the remanent magnetization M_R is retained. The field in the opposite direction needed to demagnetize the material (zero net magnetization) is called coercive field H_C. Such hysteresis is used to check the magnetization $\boldsymbol{M}$ of samples.

2.2. Energy contributions of magnetic material

In order to describe the magnetization configuration of ferromagnetic structures, the energy of the system has to be regarded. In the following, four different energy contributions will be discussed in the framework of the micromagnetic model. Here, the magnetization $\boldsymbol{M}(\boldsymbol{r})$ is assumed as a continuous vector function in space. The magnetization configuration is determined by a minimization of the total energy

$$U_{tot} = U_\mathrm{ex} + U_\mathrm{z} + U_\mathrm{d} + U_\mathrm{an} + \cdots \tag{2.3}$$

under the constraint that the absolute value of the local magnetization remains constant.

Exchange Energy

The exchange interaction has been already introduced in Sec. 2.1. In the micromagnetic model, the exchange energy can be expressed by

$$U_{ex} = A \int \left[(\nabla m_x)^2 + \left(\nabla m_y \right)^2 + (\nabla m_z)^2 \right] dr \qquad (2.4)$$

with the normalized magnetization $\boldsymbol{m}(\boldsymbol{r}) = \boldsymbol{M}(\boldsymbol{r})/M_S$ and the integral taken over the volume of the sample. The exchange constant A is determined by the quantum mechanical exchange integral and the crystal structure. For permalloy a common value is $A = 13 \times 10^{-12}$ Jm^{-1}[35]. A deviation from the parallel alignment ($\nabla m_i \neq 0$) clearly leads an increase of the exchange energy. In this thesis, the exchange interaction is one of the two dominant factors to decide magnetization $\boldsymbol{M}$ of soft ferromagnet samples.

Zeeman energy

The interaction between the magnetization of a ferromagnet and an external magnetic field $\boldsymbol{H}$ gives rise to an additional energy contribution, the Zeeman energy written as

$$U_z = -\mu_0 \int \boldsymbol{H} \cdot \boldsymbol{M} dr. \qquad (2.5)$$

Equation (2.5) describes the magnetostatic energy of an effective magnetic dipole under an external field $\boldsymbol{H}$. A parallel alignment of $\boldsymbol{M}$ and $\boldsymbol{H}$ leads to a reduction of the energy. In this thesis, the Zeeman interaction is used to manipulate and excite the magnetization configuration in ferromagnetic micro- and nanostructures via static and current induced alternating magnetic field.

Demagnetization energy

The demagnetization energy is sometimes called self magnetostatic energy since it emanates from the interaction between the magnetization configuration with the magnetic field generated by itself. Using the fundamental Maxwell equation $\nabla B = 0$ and Eq. (2.2), the relation $\nabla H = -\nabla M$ can be derived. Sinks and sources of the magnetization act as sources and sinks, respectively, for the demagnetization field $\boldsymbol{H}_d$ inside the ferromagnetic body as well as the stray field $\boldsymbol{H}_{int}$ outside the magnetic material. The demagnetization energy is calculated similarly to the Zeeman energy using the expression

$$U_d = -\frac{\mu_0}{2} \int \boldsymbol{H}_d \cdot \boldsymbol{M} dr. \qquad (2.6)$$

The long-range magnetic dipolar interaction favours an antiparallel alignment of magnetic moments which again illustrates the nomenclature for $\boldsymbol{H}_d$ as demagnetization field. On the short length scale this interaction is small in comparison to the exchange interaction. However, the interaction between all magnetic moments within the sample adds up to a relevant contribution to the total energy. The formation of the magnetic vortex patterns discussed in Sec. 2.6 cannot be explained without considering contribution of theses energy. The demagnetization field results in the shape anisotropy where a preferred magnetization direction is induced by the shape of the ferromagnetic body.

Magnetocrystalline anisotropy

The last energy contribution noted on the right-hand side of Eq. (2.3) is due to the magnetocrystalline anisotropy. In ferromagnetic crystals, a preferred alignment of the magnetization along certain so-called easy axes arises from the spin-orbit interaction which couples the spin magnetic moments to the crystal lattice. Tilting the magnetization away from these axes leads to an increase of energy. For a cubic crystal the energy can be expressed by

$$U_{an} = \int \left[K \left(m_x^2 m_y^2 + m_y^2 m_z^2 + m_z^2 m_x^2 \right) + K_2 \left(m_x^2 m_y^2 m_z^2 \right) \right] d\vec{r}, \qquad (2.7)$$

where m_i are the magnetization components along the cubic axes and K and K_2 are the anisotropy constants. In permalloy, the magnetocrystalline anisotropy is small $\left(K = 500 \text{ Jm}^{-3}\right)$[36,33] which means that the magnetization can align along arbitrary crystal directions and U_{an} can be neglected in the majority of cases.

In chapters 5 and 6, the dipolar interaction between spatially separated structures is investigated which requires the introduction of an additional energy contribution U_{int}. The stray field $\boldsymbol{H}_{\mathrm{int}}$ of a neighbouring structure leads to an additional Zeeman energy term. Further energy contributions exist, the surface and interface anisotropy as well as magnetostriction. These contributions are negligible small for the material and structures investigated in this thesis[37].

Effective field

As already mentioned in the beginning of this section, the equilibrium magnetization configuration is given by a minimum of the total energy U_{tot}. At this point, it should be stressed that a minimization of U_{tot} is not merely equivalent to the minimization of each single energy contribution. The influence of the different energy contributions can be expressed in terms of a continuous effective field $\boldsymbol{H}_{\mathrm{eff}}$ acting on the magnetization $\boldsymbol{M}(\boldsymbol{r})$ and the track of magnetization process has to be discussed to obtain precise magnetization structure. Using variational calculus[38], it can be shown that in the equilibrium configuration $\boldsymbol{M} \times \boldsymbol{H}_{\mathrm{eff}} = 0$, which mean that at every point the magnetization is aligned along the direction of the effective field and, consequently, no torque is acting on the magnetization. As far as the region of interest in this thesis, the effective field is composed of the exchange field which can be calculated to $\boldsymbol{H}_{\mathrm{ex}} = 2A/\left(\mu_0 M_S^2\right)\nabla^2 \boldsymbol{M}$, the external field $\boldsymbol{H}$, and the demagnetization field $\boldsymbol{H}_{\mathrm{d}}$. The magnetocrystalline anisotropy can be considered by $\boldsymbol{H}_{\mathrm{an}} = -\mu_0^{-1}\partial\epsilon_{\mathrm{an}}/\partial\boldsymbol{M}$, where ϵ_{an} is the energy density given by E_{an} per volume.

2.3. Concept of magnetic charges

For an arbitrarily shaped ferromagnetic body, the demagnetization field $\boldsymbol{H}_{\mathrm{d}}$ is a complex function in space and an analytical calculation is only possible for a few special cases. A general solution is given by potential theory[39]: $\boldsymbol{H}_{\mathrm{d}}$ can be derived by $\boldsymbol{H}_{\mathrm{d}} = -\nabla\Phi_{\mathrm{d}}(\boldsymbol{r})$ from the potential

$$\Phi_{\mathrm{d}}(\boldsymbol{r}) = \frac{M_S}{4\pi}\left[\int \frac{\sigma_S(\boldsymbol{r}')}{|\boldsymbol{r} - \boldsymbol{r}'|}dS' + \int \frac{\sigma_V(\boldsymbol{r}')}{|\boldsymbol{r} - \boldsymbol{r}'|}d\boldsymbol{r}'\right] \tag{2.8}$$

which fulfills the Poisson equation $\Delta\Phi_{\mathrm{d}} = -\sigma_V$. Here, σ_S is the magnetic surface charge density $\sigma_S = \boldsymbol{m}\cdot\boldsymbol{n}$ with the surface normal $\boldsymbol{n}$ and σ_V is the volume charge density $\sigma_V = -\nabla\cdot\boldsymbol{m}$. The magnetization tends to align parallel to the surface in order to minimize the surface charges. Sinks and sources of the magnetization lead to the appearance of volume charges. In contrast to electric charges, magnetic charges never appear isolated but are always balanced by opposite charges. Within the scope of this thesis, emergent magnetic monopoles, e.g., in spin ice structures[40] are not regarded.

In Fig. 2.2, the example of a ferromagnetic rectangle is shown to illustrate the above concept. A uniform magnetization along the short axis of the rectangle, as shown in Fig. 2.2(a), leads to the appearance of a large number of surface charges generating a large demagnetization field $\boldsymbol{H}_{\mathrm{d}}$. This magnetization configuration is obviously energetically unfavorable in comparison to the configuration shown in Fig. 2.2(b) with the magnetization pointing uniformly along the long axis. Note that in both cases the exchange energy is zero according to Eq. (2.4). The configuration in Fig. 2.2(a) is only energetically favorable in the presence of a strong magnetocrystalline anisotropy defining the easy axis in the corresponding direction. At this point, in Figs. 2.2(a) and (b) the demagnetization field defines the easy axis along the long axis of the rectangle which is referred to as shape anisotropy.

By segmenting the crystal in two domains with opposite magnetization direction, the demagnetization energy due to surface charges can be significantly reduced, see Fig. 2.2(c). However, the magnetization configuration in the transition region between the two domains, the so-called domain wall, on the other hand costs energy. The exchange interaction opposes an abrupt transition. The magnetization gradually changes its direction where the width of the domain wall is determined by the competing energy contributions. Small angles between the magnetization vectors and thus a wide
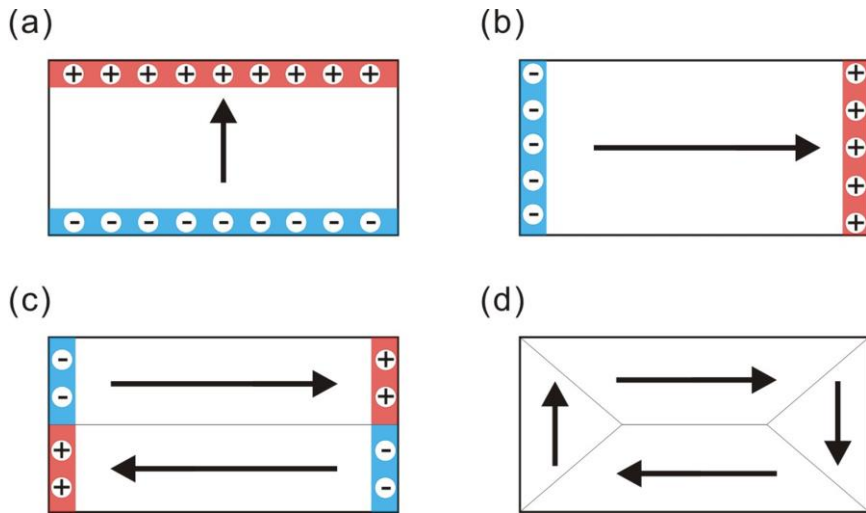

FIG. 2.2: Cartoon of different magnetization configurations in a ferromagnetic rectangle. A uniform magnetization along (a) the short axis and (b) the long axis as well as (c) a state with two antiparallel domains and (d) a flux closure domain pattern are shown. Arrows indicate the magnetization direction. The sign of the magnetic surface charges is illustrated via (+) and (−).

transition region are favoured by the exchange interaction. On the other hand, the magnetocrystalline anisotropy and the shape anisotropy tend to avoid deviations from the easy axes and lead to a narrowing of the wall. Basically, there are two prominent types of domain walls, a Bloch wall and a Néel wall. The Bloch wall with a continuous 180° transition of the magnetic moments in the plane of the wall mainly occurs in bulk-like structures and thicker films. B. A. Lilley first introduced the width of a Bloch wall as $w = \pi\sqrt{A/K}$[41] ($w \approx 5.3$ nm for permalloy). A rotation of the magnetization out of the sample plane induces surface charges and thus increases the demagnetization energy. For this

reason, Néel walls with the moments aligned perpendicular to the wall plane, that is in the plane defined by the magnetization in the domains, occur in thin-film structures. The core of the Néel wall, where magnetization stands perpendicular to the plane, scales with the exchange length $l_{\text{ex}} = \sqrt{2A/(\mu_0 M_S^2)}$ ($l_{\text{ex}} \approx 5.3$ nm for permalloy) giving the characteristic length scale where changes of the magnetization direction occur. Surface charges completely vanish in the flux closure domain pattern shown in Fig. 2.2(d). The ferromagnet splits up in domains of different magnetization directions in order to minimize the demagnetization field. This state is energetically favorable when the reduction of the demagnetization energy exceeds the energy needed to form the domain walls. The concept of magnetic charges will be applied to give an analytical description of the demagnetization field inside and the stray field outside ferromagnetic disks in the vortex state, see Sec. 2.6 and 2.7.

2.4. Magnetization dynamics

2.4.1. Landau-Lifshitz-Gilbert equation

In a magnetic field H, the magnetization experiences a torque which is described by the Equation

$$\frac{d\boldsymbol{M}}{dt} = -\gamma \mu_0 \boldsymbol{M} \times \boldsymbol{H}, \tag{2.9}$$

where γ is the gyromagnetic ratio defined in Sec. 2.1. The magnetization precesses around the magnetic field H with the Lamor frequency $\omega = \mu_0 \gamma H$. So far, only static magnetization configurations have been discussed where the torque on the magnetization vanishes. Equation (2.9) is the starting point for any description of dynamic processes in micromagnetics.

In a real system, a continuous precession does not exist. In the last paragraph of Sec. 2.2, the vanishing torque $\boldsymbol{M} \times \boldsymbol{H}_{\text{eff}} = 0$ in the equilibrium configuration has been discussed. To account for the intrinsic damping of the system, first Landau and Lifshitz[42] and later on Gilbert[43] introduced a damping term on the right-hand side of Eq. (2.9) that forces the magnetization in the direction of the magnetic field. The widely used Landau-Lifshitz-Gilbert (LLG) equation reads

$$\frac{d\boldsymbol{M}}{dt} = -\gamma \mu_0 \boldsymbol{M} \times \boldsymbol{H}_{\text{eff}} + \frac{\alpha}{M_S} \boldsymbol{M} \times \frac{d\boldsymbol{M}}{dt}. \tag{2.10}$$

Here, α is the phenomenological Gilbert damping parameter which is typically $\alpha \approx 0.01$ for permalloy [44]. The Landau-Lifshitz equation $\frac{d\boldsymbol{M}}{dt} = -\gamma\mu_0\boldsymbol{M} \times \boldsymbol{H}_{\text{eff}} + \alpha_{\text{LL}}\frac{\mu_0\gamma}{M_S}\boldsymbol{M} \times (\boldsymbol{M} \times \boldsymbol{H}_{\text{eff}})$ is equivalent to the LLG equation on the case of low damping $(\alpha \ll 1)$. The magnetization experiences a damped precessional motion about $\boldsymbol{H}_{\text{eff}}$ as shown in Fig. 2.4 (a).
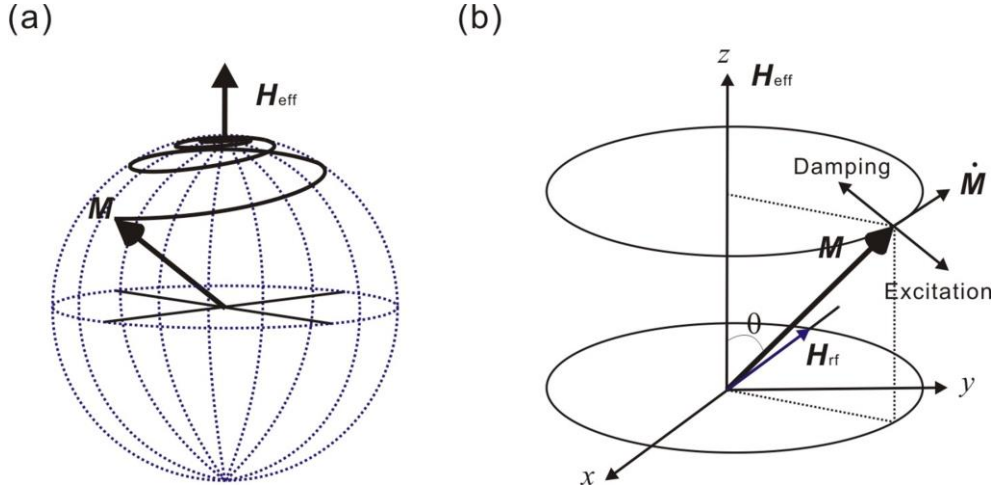

FIG. 2.4: (a) Precessional motion of a magnetization $\boldsymbol{M}$ about an effective field $\boldsymbol{H}_{\text{eff}}$. Due to the damping of the system, the magnetization relaxes in the direction of the effective field. (b) Schematic to illustrate the resonant excitation of the magnetization vector $\boldsymbol{M}$ at ferromagnetic resonance. An exciting field $\boldsymbol{H}_{\text{rf}}$ leads to a torque which compensates the torque due to damping. The magnetization precesses with a constant cone angle θ around the effective field $\boldsymbol{H}_{\text{eff}}$.

2.4.2. Ferromagnetic resonance

Before entering introductions of current-induced additional torques, the general solution of LLG equation is once discussed to support understanding of typical form of ferromagnetic resonance. The precessional motion is sustained using a time-dependent driving field $\boldsymbol{H}_{\text{rf}}$ perpendicular to the effective field $\boldsymbol{H}_{\text{eff}}$ already in place. In the case of low damping, the deviation between the eigenfrequency and the frequency of resonant excitation is sufficiently small. Figure 2.4(b) shows the geometry relation of an additional torque acts on the magnetization $\boldsymbol{M}$ which is due to $\boldsymbol{H}_{\text{rf}}$. In resonance, this torque compensates the torque due to the damping of the system, compare Eq. (2.10). Note that energy has to be continuously brought into the system to sustain the precessional motion to keep a constant cone angle θ.

We now consider a uniformly magnetized sample where the local magnetization components are strongly coupled and are thus pointing parallel to each other. In this case, the contribution of the exchange interaction to the effective field $\boldsymbol{H}_{\text{eff}}$ vanishes. The volume integral in Eq. (2.8) is zero since no volume charges appear. The magnetization can be taken out of the surface integral and differentiation yields the demagnetization field

$$H_{\mathrm{d}} = -\frac{M}{4\pi} \int \nabla_{r'} \frac{n'}{|r-r'|} \, dS' = -\widehat{N}M. \tag{2.11}$$

The demagnetization tensor $\widehat{N}$ can be calculated analytically for a few special cases, e.g., an infinitely extended plate or an ellipsoid. Taking the demagnetization energy of the inscribed ellipsoid, the energy of compact bodies can be often well approximated. For ellipsoidal-shaped samples the coordinate system can be rotated in such a way that the demagnetization tensor $\widehat{N}$ is diagonal. According to Eq. (2.11), in this case the trace of $\widehat{N}$ is $\mathrm{Tr}[\widehat{N}] = N_x + N_y + N_z = 1$. The components of the effective field can be written as $H_x^{\mathrm{eff}} = H_x^0 - N_x M_x$, $H_y^{\mathrm{eff}} = H_y^0 - N_y M_y$, and $H_z^{\mathrm{eff}} = H_z^0 - N_z M_z$. Solving the equation of motion (2.10) without damping by using the above field $\vec{H}_{\mathrm{eff}}$ yields the resonance frequency[45]

$$f_{res} = \frac{\gamma \mu_0}{2\pi} \sqrt{\left(H_0 + \left(N_x - N_y\right)M_{\mathrm{S}}\right)\left(H_0 + \left(N_z - N_y\right)M_{\mathrm{S}}\right)}. \tag{2.12}$$

The external field H_0 points in y direction and the magnetization component in y direction is assumed to be constant $M_y = M_{\mathrm{S}}$ (and consequently $dM_y/dt = 0$). Equation (2.12) is referred to as Kittel formula. Note that it is only valid for a uniformly magnetized ferromagnet with a homogeneous effective field. The resonance frequency strongly depends on the shape of the sample. For a thin film in the xy-plane, the demagnetization factors are $N_x = N_y = 0$ and $N_z = 1$ and Eq. (2.12) reads[45]

$$f_{res} = \frac{\gamma \mu_0}{2\pi} \sqrt{H_0(H_0 + M_{\mathrm{S}})}. \tag{2.13}$$

2.4.3. Spin-Transfer Torque

In the applicational area, rapid progress of magnetic devices accelerates downsizing of the unit scale and causes increasing of the switching field due to the larger demagnetization field. Above Field induced ferromagnetic excitation cannot be suitable in such region because of increasing of consumed power for switching. As the direct solution of this problem, the idea of current-induced magnetization switching based on injection of spin transfer torque was first proposed in 1990s by L. Berger[46,47] and J. C. Slonczewski[48], and soon experimentally demonstrated within few years[49,50,51,52]. Here the smaller the unit scale becomes, the more the required current decreases opposite to field-induced switching, and this revolutionary technique enables to remarkable downscale of devices. Spin transfer torque is simply caused when spin angular momentum of spin polarized conduction electrons is transported to the local magnetization moment and now becomes one of the most fundamental phenomena in spintronics. The terms of spin transfer torque are treated as opposite action to the damping term in LLG equation thus self-resonant excitation would be derived[53] in conditions where these two effects are balancing (see a schematic image in Fig. 2.7). In this thesis, spin transfer torque is adopted to excite magnetization dynamics in order to not only use for electrical frequency sensor as detection system but also excites neighboring ferromagnetic disks independently, as in chapter 5.

Principles of spin transfer torque and current-induced magnetization switching

The basic scheme of current-induced magnetization switching is easy to be explained in trilayer system of first ferromagnet (F1) / non-magnet (N) / second ferromagnet (F2). As show in Fig. 2.5, the magnetization direction in F1 is uniformly aligned to z axis and spin momentum of conduction
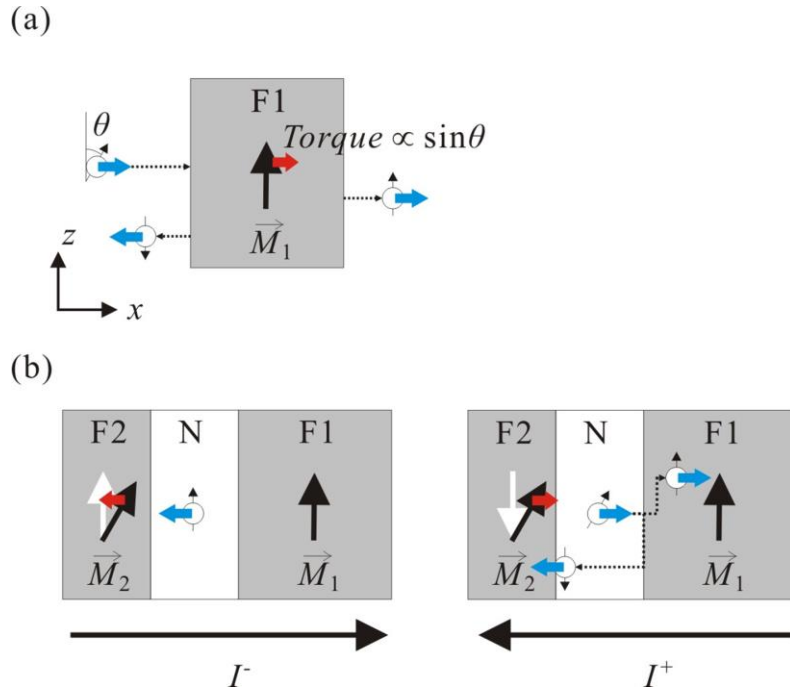

FIG. 2.5: (a) Cartoon of principle of spin transfer torque. (b) Cartoons of current induced magnetization switching at F1/N/F2 trilayer for positive and negative current.

electrons are tilted with a constant angle θ. Here spin state $S(\theta)$ is expressed by liner combination of up spin state $|\uparrow\rangle$ and down spin state $|\downarrow\rangle$ as

$$S(\theta) = \cos(\theta/2)\,|\uparrow\rangle + \sin(\theta/2)\,|\downarrow\rangle. \qquad (2.14)$$

In the ferromagnet F1, there exists effective magnetic field by ferromagnetic atoms thus conduction electrons with up spin states $|\uparrow\rangle$ are easily transferred while those with down spin states $|\downarrow\rangle$ are reflected at the interface of F1. When electrons are transferred in F1, local magnetization direction in F1 needs to tilt with a constant angle $+\theta$ to to z axis as an opposed action on conduction electrons since net spin angular momentum has to keep constant. This is equal for magnetization direction in F1 to be applied torque by conduction electrons, i.e. spin transfer torque. This spin transfer torque is applied at the interface area. One can notice that injected electrons should have various momentum vector however all phase differences are cancelled out though integration and x component of injected spin states are lost. In other words, the orthogonal component to magnetization direction in F1 is absorbed at the interface while this absorbed angular momentum is applied as torque on magnetization in F1[54].

The simplified processes of current-induced magnetization switching are illustrated in Fig. 2.5 (b). Here, magnetization direction in F2 M_2 is tilted from z axis and that in F1 M_1 is fixed parallel to z axis. When the conduction electron flows from F1 to F2 (I^-), this electron transfers up spin

angular momentum and spin transfer torque is applied to M_2 to be parallel to M_1. On the other hand the conduction electrons flow from F2 to F1 (I^+), up spin electrons go through F1 without giving any momentum and down spin electrons are reflected at the interface of N/F2. Consequently, down spin angular momentum is transferred to F2, and spin transfer torque here is applied to M_2 to be antiparallel to M_1. In these ways, a current direction controls the direction of the spin transfer torque applied and further determines the end state of magnetization configuration of trilayer system.

The conventional LLG equation in Eq. (2.10) is revised to take into account spin transfer torque as[48]

$$\frac{d\boldsymbol{M}}{dt} = -\gamma\mu_0\boldsymbol{M}_1 \times \boldsymbol{H}_{\text{eff}} + \frac{\alpha}{M_{1S}}\boldsymbol{M}_1 \times \frac{d\boldsymbol{M}_1}{dt}$$

$$+ \frac{2\mu_B}{V}g(\theta)\frac{I_e}{e}\boldsymbol{m}_1 \times (\boldsymbol{m}_1 \times \boldsymbol{m}_2),$$

(2.15)

where V is the volume of ferromagnet, μ_B is Bohr magnetron, I_e is the applied current and $g(\theta)$ is the permeability coefficient function of the angle between M_1 and M_2. m_1 and m_2 are the unit vectors of M_1 and M_2. The third right hand term shows the spin transfer torque and acts as the opposite force to second damping term. The geometry relation of precession torques on magnetization is shown in Fig. 2.7. Magnetization switching occurs on condition that spin transfer torque exceeds damping torque, i.e. the third term becomes lager than the second term. Equation (2.15) gives an analytical solution in cases the effective field H_{eff} consists of external field H_0 and anisotropic field H_{ani}, as

$$J_{c0}^{\pm} = \alpha e M_S t[H_0 \pm (H_{\text{ani}} + 2\pi M_S)]/\hbar \cdot g(\theta).$$

(2.16)

One can easily notice that the critical current $J_{c0}^{\pm}$ is proportional to sample thickness t thus switching current decrease with downsizing opposite to field switching. This is the crucial factor why the use of spin transfer torque enables scaling of nano-devices. With assumption of ballistic transport, $g(\theta)$ is given as below[55].

$$g(\theta) = \left[-4 + (1 + P)^3(3 + \cos\theta)/4P^{3/2}\right] - 1 \quad \text{(GMR)}$$

(2.17)

$$g(\theta) = P/(1 + P^2\cos\theta) \quad \text{(TMR)}$$

(2.18)

Current-induced domain wall motion

The concept of driving domain walls by spin transfer torque in ferromagnet is presented in the early stage of spintronics[46]. However, it takes nearly 30 years to realize in experimental set up using a permalloy nanowire[56]. The schematic image is prepared in Fig. 2.6 to briefly explain the current-induced domain wall motion. In a ferromagnetic nanowire with single domain wall, magnetization directions at edges are aligned opposite direction and gradually rotate in the domain wall structure. When the current flows from right side, i.e. conduction electrons move from left to right, the spin direction of electrons rotate since the exchange interaction with magnetization direction at each position. This difference of spin angular momentum results in applying spin transfer torque to local magnetization due to the principle of conservation of angular momentum. In this way, the domain wall is driven to opposite to the current direction. Current-induced domain wall motion was

first observed using imaging technique by the magnetic force microscope. In experiments, the domain walls are pinned by preparing notches in the wire and the value of critical current J_c is given as[57]

$$J_c = 2eK\delta/\pi\hbar P, \tag{2.19}$$

where K is the anisotropic coefficient of hard axis and P is the spin polarization of current. The velocity of domain wall v is written as

$$v = g\mu_B PJ/2eM_S, \tag{2.20}$$

Character of g expresses Landé g-factor and J does the current density. The typical value of critical current J_c of permalloy is around 10^{12} A/m^2 and velocity v is around 100 m/s at that time[58]. It is
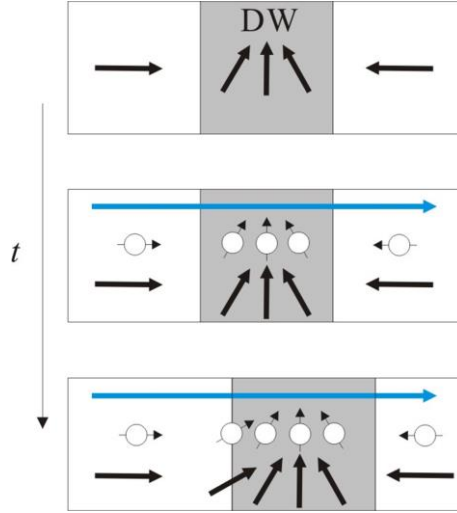

FIG. 2.6: Schematic image of transport of spin angular momentum from conduction electrons to local magnetization under the current induced domain wall motion in magnetic nanowire with single domain wall.

difficult to say critical current J_c is enough small to directly applied into real devices with neglecting thermal effect, however the value of J_c are expected to be greatly improved by using perpendicularly magnetized materials like Co/Ni multi layers[59].

Non-adiabatic spin transfer torque

In discussions so far, only the spin angular momentum transfers at equilibrium states are considered. Added to this, recent studies of spin transfer torque observe appearances of non-equilibrium processes of spin angular momentum transport from itinerant electrons to local electrons. The discussion of these non-adiabatic spin transfer torque have been first introduced by S. Zhang *et al.*[60] in the time-dependent semiclassical transport theory. Reconstructed LLG equation taking into non-instantaneous processes of itinerant spin relaxation into local spin is described as

$$\frac{d\boldsymbol{M}}{dt} = -\gamma\mu_0\boldsymbol{M}_1 \times \boldsymbol{H}_{\text{eff}} + \frac{\alpha}{M_{1S}}\boldsymbol{M}_1 \times \frac{d\boldsymbol{M}_1}{dt} + \frac{2\mu_B}{V}g(\theta)\frac{l_e}{e}\boldsymbol{m}_1 \times (\boldsymbol{m}_1 \times$$

$$\boldsymbol{m}_2) - \frac{c_J}{M_{1S}}\left(\boldsymbol{M}_1 \times \frac{d\boldsymbol{M}_1}{dx}\right). \tag{2.21}$$

Here coefficient c_J has the unit of velocity and decides the amplitude of non-adiabatic process, which is related to the spatial mistracking of spins between conduction electrons and local magnetization. The geometric relations of all current-induced torques are illustrated in Fig. 2.7. The non-adiabatic contribution to this spin-transfer torque, which support Larmor rotating torque, is currently under strong debate, as its value differs by orders of magnitude in theoretical predictions[60,61,62] and in measurements[63,64,65,66]. Recently because of its high symmetry and spatial confinement, a vortex in a micro- or nanostructured magnetic thin film is drawing attractions as a promising system for the investigation of the spin-torque effect[67] and several experimental trials have been performed to
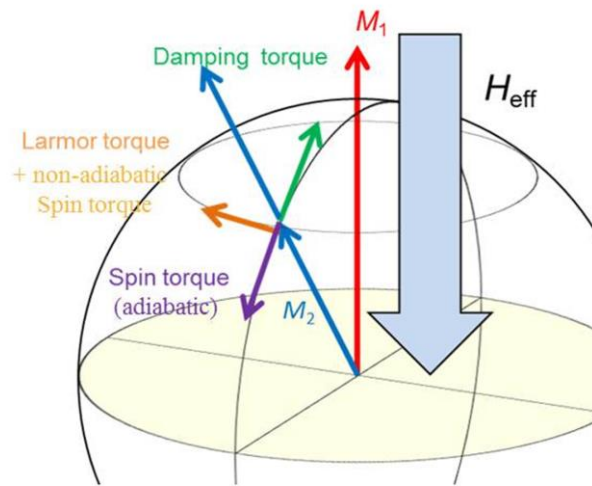

FIG. 2.7: Cartoon of the current-induced excitation torques on the magnetization vector $\boldsymbol{M}$. Geometries of all driving torques, such as Larmor torque, damping torque, adiabatic and nonadiabatic spin transfer torques are illustrated by arrows.

evaluate non-adiabatic contribution using vortex structure[68,69,70].

2.5. Anisotropic magnetoresistance

The resistance of a ferromagnetic sample depends on the angle between the magnetization and the direction of the current. In 1936, N. Mott first reported that the current in the investigated transition metals is mainly carried by *s* electrons, and the electrical resistance is attributed to scattering due to spin-dependent interband *sd* transitions[71]. Non-rotational symmetric charge distributions which are linked to the magnetization direction lead to an anisotropic scattering cross section and thus yield a difference in the resistivity $\Delta\rho = \rho_\parallel - \rho_\perp$ depending on the alignment of magnetization and current[72]. For any angle θ between the magnetization and the current, the resistivity is given by

$$\rho(\theta) = \rho_\parallel - \Delta\rho\sin^2\theta. \tag{2.22}$$

The resistivity rises to maximum for parallel alignment and fall to minimum for perpendicular alignment. Anisotropic magnetoresistance (AMR) effect is exploited to detect the presence of a domain wall and detect the dynamics of magnetic vortices in this thesis, as later studied in detail in chapter 4.

2.6. Magnetic vortex

2.6.1. Vortex bubble structure as a remanent state
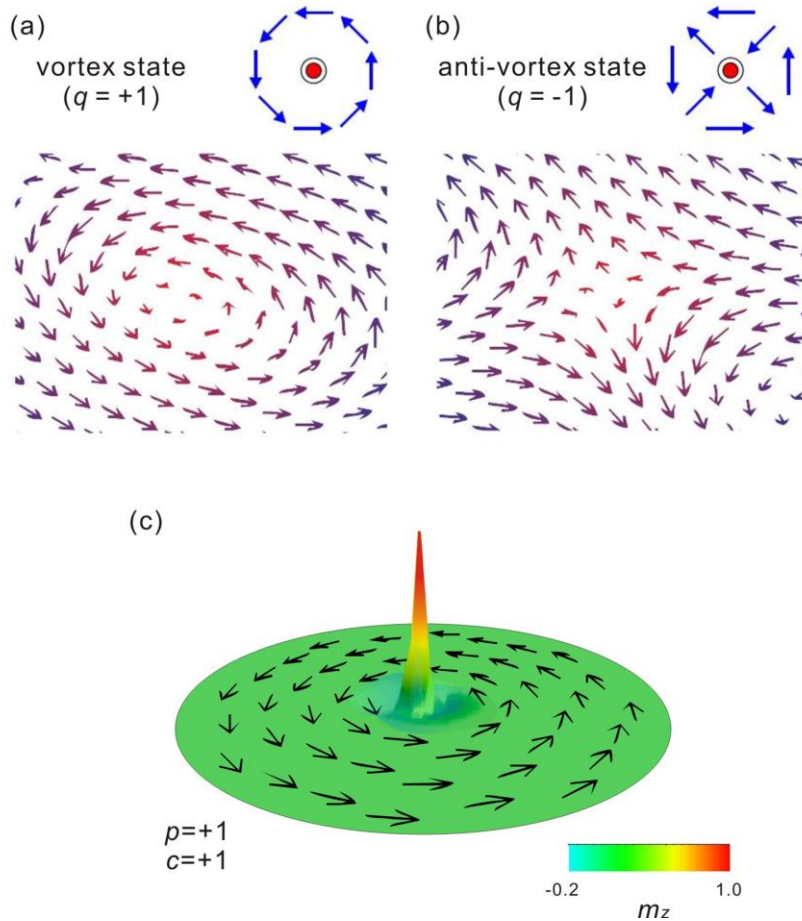
FIG. 2.8: Magnetization configuration of (a) vortex structure and (b) anti-vortex structure. The singular point is pigmented by red color. (c) A Magnetization vortex as a remanent state of circular shaped ferromagnetic disk with $(p, c) = (+1, +1)$.

As mentioned in previous section 2.2 and 2.3, the remanent state of magnetizations $\boldsymbol{M}(\boldsymbol{r})$ is generally quite complicated depending on material parameters and the history of magnetization process. For permalloy single film, that is originally developed to possess a large magnetic permeability μ in order to show a quick response to external magnetic field change, contributions of magnetostrictive energy and magnetic anisotropic energy can be negligible. Therefore only the exchange energy U_{ex}, the

16

Zeeman energy U_z and the demagnetization energy U_d are worth to be discussed in a soft ferromagnet : $U_{tot} \sim U_{ex} + U_z + U_d$.

Here we assume the cylindrical shaped disk structure without external field $(U_z = 0)$. Focusing on the edge area, magnetization align should parallel to the edge surface to suppress the emergence of magnetic charges, which is equal to minimize the demagnetization energy U_d, i.e. eliminate the side charge. Subsequently neighboring magnetizations aligns parallel along the radial direction to the center so as to decrease exchange energy loss U_{ex}. As a consequence, the magnetization takes a circular form inside the disk. However, one may wonder that at the very center of the disk, neighboring magnetization need to be aligned opposite direction inevitably within this rule. Since the exchange interaction is larger than the demagnetization interaction at short range, the magnetizations stand up perpendicular to the plane at this very center. Scale of this unique point is comparable with exchange length l_{ex}, less than 10 nm in case of permalloy as shown in Fig. 2.9. (b). In these ways, the magnetic vortex structure with in-plane carling magnetization: chirality, which can take clockwise direction or counter clockwise direction $(c = \pm 1)$, and standing magnetization structure at the core region: polarity, which can align up or down direction perpendicular to plane $(p = \pm 1)$, finally appears as a remanent state (Fig. 2.8 (c)). Note that our discussion is targeting on amorphous or polycrystalline films and any chiral force such like the Dzyaloshinskii-Moriya interactions[73,74] is not regarded here. Naturally, the net energy U_{tot} does not change depending on any combination of
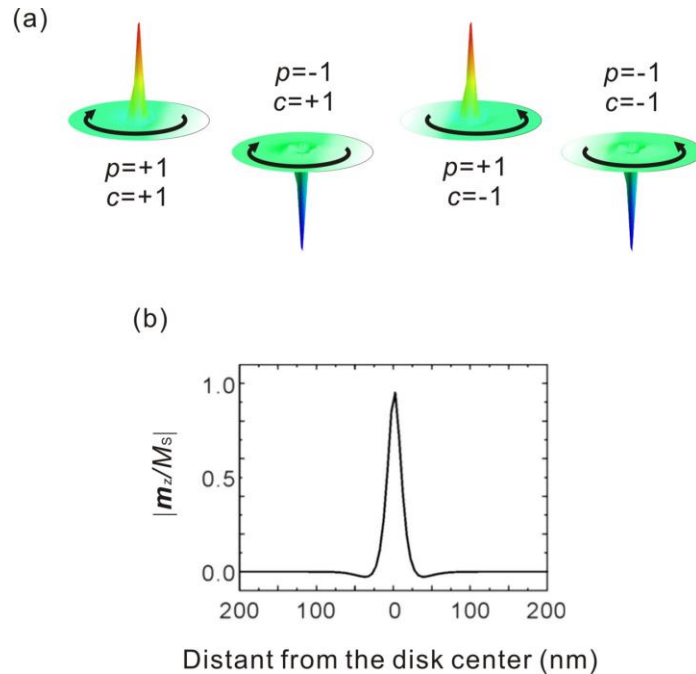
FIG. 2.9: (a) 4 possible combination of polarity and chirality of magnetic vortex. These 4 states are treated energetically identical in this thesis. (b) Simulated cross sectional magnetization of core region.

polarity and chirality (Fig. 2.9. (a)), and two values (p, c) can be regarded as independent parameters to switch symmetry of vortex system (explained in Sec. 2.7). By necessity, thickness and disk radius

shall become critical parameters to decide the appearance of vortex configuration. To support understanding, an early theoretical works of magnetic phase diagram of permalloy cylindrical dots by W.Scholz *et al.*[75] is reprinted in Fig. 2.10. The thicker disks, the energy of magnetic charges at side surface becomes so large that the remanent state is perpendicularly magnetized single domain structure (top image). On the contrary, the thinner disks, the contribution of in-plane demagnetization energy exceeds that of exchange energy even though the center region thus in-plane magnetized single domain structure is stabilized as a remanent state (middle image). It is clear that the vortex structure is stabilized due to competitiveness of the exchange energy and the demagnetization energy (bottom image).
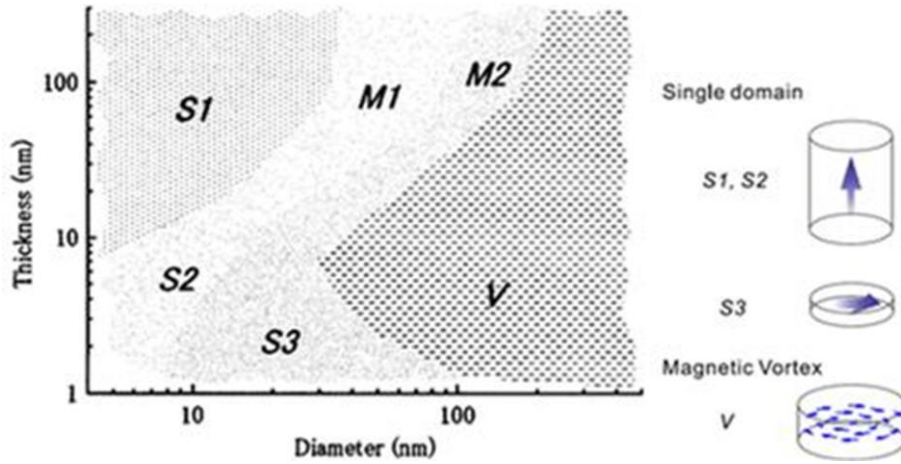

FIG. 2.10: Micromagnetic calculations of magnetic phase diagram of circular shaped permalloy dots. Modified from ref. 75.

2.6.2. The energy of the magnetic vortex

To obtain more insights of the magnetic vortex structure, we introduce an analytical calculation recently developed by Goto *et al.*[76]. With excluding the Zeeman energy U_Z, only the exchange energy U_{ex} and the demagnetization energy U_d are considered and magnetization distribution along z-axis is neglected here. We put the disk center $r_d = (x_d, y_d)$, core position $r = (x, y)$, and $\rho = r_d - r = (\rho, \varphi)$ for the polar coordinate system. The core is assumed as a "rigid point" and a vortex structure is kept how large the core deflected from the equilibrium position. Large core shift breaks in-plane symmetry thus side magnetic charges necessarily appear without assuming relaxation process at the edge region. The density of side magnetic charge is thus calculated as

$$M_{\mathrm{p}}(\theta) = cM_S \frac{(y_d - y)\cos\theta - x_d\sin\theta}{\sqrt{x_d{}^2 + (y_d - y)^2}}.$$ (2.23)

Here, θ is the cone angle from the x-axis: $\theta = \tan^{-1}(y_d/x_d)$, Using Taylor expansion for r, the demagnetization energy is calculated as

$$U_d = -\frac{\mu_0}{2} \int_{disk} \boldsymbol{M} \cdot \boldsymbol{H}_d d^3 x_d$$

$$= \frac{\pi \mu_0 M_S^2 L^2}{8R} y^2 \equiv \frac{1}{2} \kappa_d y^2$$

(2.24)

Note that U_d is proportional to the square of core deviation $\boldsymbol{r} = (x, y)$ thus the demagnetization energy can be treated as a form of parabolic potential for distance of core deflection. The effective stiffness coefficient κ_d as the following:

$$\kappa_d = \frac{\pi \mu_0 M_S^2 L^2}{4R}.$$

(2.25)

Next, we move onto calculations of the exchange energy U_{ex}. The density of the exchange energy by above equation takes infinite value at the very center of the disk since the magnetization shall stand up perpendicularly. Therefore, we consider contribution from the side surface are by making differential between (the integral area after the core shifts) and (the integral area before it shifts). In this way, the singular point (vortex core) can be excluded from calculations. The exchange energy U_{ex} is given by

$$U_{ex} = A \int_{disk} \frac{d^3 x_d}{\rho^2}$$

$$= AL \int_{-R}^{R} dx_d \left\{ \int_{-\sqrt{R^2-x_d^2}}^{-\sqrt{R^2-x_d^2}+y} dy_d \frac{1}{x_d^2 + (y_d - y)^2} \right.$$

$$\left. - \int_{\sqrt{R^2-x_d^2}}^{\sqrt{R^2-x_d^2}+y} dy_d \frac{1}{x_d^2 + (y_d - y)^2} \right\}$$

(2.26)

$$\cong -\frac{ALy^2}{R^2} \int_{-R}^{R} dx_d \frac{2\sqrt{R^2 - x_d^2}}{R^2}$$

$$= -\frac{\pi AL}{R^2} y^2 \equiv \frac{1}{2} \kappa_{ex} y^2$$

Here, we define

$$\kappa_{ex} = \frac{2\pi AL}{R^2}.$$

(2.27)

Interestingly both the demagnetization energy U_d and the exchange energy U_{ex} form the parabolic potential as a function of core position $\boldsymbol{r} = (x, y)$. In these ways, the vortex core usually treated as the "rigid quasiparticle" confined in the parabolic potential U as,

$$U \equiv U_d + U_{ex}$$

$$= \frac{1}{2} \left(\frac{\pi \mu_0 M_S^2 L^2}{4R} + \frac{2\pi AL}{R^2} \right)$$

(2.28)

$$\equiv \frac{1}{2} \kappa \boldsymbol{r}^2$$

Note that above model neglects the magnetization relaxation at the edge region and assume the completely circling magnetization configuration inside the disk. In some literatures, different approaches have been employed to obtain an analytical expression for the demagnetization energy.

The side-charge free model[77] assumes small distortions of the carling magnetization in order to avoid emergence of surface charges, and leads to a good quantitative agreement between micromagnetic simulations and analytical calculations for the eigenfrequency of a single vortex. On the other hand, the latter model is not suitable to describe coupled vortex systems[21] which are in the focus of interest of this thesis in chapter 5. We here give attention to the rigid vortex model which is useful for a qualitative understanding of both, the dynamics in single structures and coupled systems.

2.6.3. Vortex-core gyration

In Sec. 2.4, the uniform magnetization precession at ferromagnetic resonance has been discussed. Higher order excitations can cause the magnetic moments to precess with the same frequency but different phase. Consequently, collective magnetization dynamics is excited which usually approximated as a core gyration around the equilibrium position with keeping "rigid" vortex structure. A low frequency mode associating a core gyrotropic motion, usually called as the translational mode, appears in magnetic vortex structures that have been introduced. Starting from the LLG equation (2.10), A. A. Thiele[78] derived an equation describing the dynamics of magnetic bubbles as rigid quasiparticles. The Thiele equation was adopted by Huber[79] to a vortex system, and further effects of spin transfer torque (both adiabatic[80] and nonadiabatic[67,81]) was recently introduced. The general form of Thiele equation today reads

$$\boldsymbol{G}(p) \times (\boldsymbol{u} - \dot{\boldsymbol{r}}) = -\frac{\delta U(\boldsymbol{r})}{\delta \boldsymbol{r}} - \alpha D \dot{\boldsymbol{r}} + \beta D \boldsymbol{u}. \tag{2.29}$$

$\boldsymbol{G}(p)$ is the polarization-dependent gyrovector calculated for the investigated structures with $\boldsymbol{G}(p) = -(2\pi p L M_S/\gamma)\boldsymbol{e}_z \equiv -G_0 \boldsymbol{e}_z$[82], where p, L, M_S, μ_0, γ, and $\boldsymbol{e}_z$ are, respectively, the polarity of the core, the thickness of the ferromagnetic disk, the saturation magnetization of the ferromagnet, space permeability, the gyromagnetic ratio, and the unit vector along the z direction. The unit of spin transfer torque is expressed using u_0, whose unit is same with velocity. In case of ac current injection with frequency ω, time depending spin transfer torque term is written as $\boldsymbol{u}(t) = -(\mu_B J P/eM_S)e^{i\omega t}\boldsymbol{e}_x \equiv u_0 e^{i\omega t}\boldsymbol{e}_x$, where μ_B, J, P, e, and $\boldsymbol{e}_x$ are the Bohr magneton, the current density, the spin polarization of the ferromagnet, the electric charge, and the unit vector along current injection (x-axis). The contribution of spin transfer torque is evaluated by non-dimensional constant of nonadiabatic effect β. $-\frac{\delta U(\boldsymbol{r})}{\delta \boldsymbol{r}}$ is the restoring force due to the parabolic potential energy $U(\boldsymbol{r})$ given by Eq. (2.28), where D is the diagonal dissipation tensor with $D_{xx} = D_{yy} = D_0$ and $D_{zz} = 0$[83]. The value of D_0 depends on the geometry of the sample. For a disk, the damping parameter is $D_0 = -2\pi\alpha L M_S \left[1 + \ln\left(\frac{R}{R_C}\right)/2\right]/\gamma$[84], where R is the radius of the disk and $R_C = 0.68(L/l_{ex})^{1/3}$ is the thickness-dependent core radius. When the total energy $U(\boldsymbol{r})$ is known, analytical expressions for the eigenfrequency and the trajectory of the vortex core can be deduced by solving Eq. (2.29). As derived in the last section, $U(\boldsymbol{r})$ is usually written using form of $U(\boldsymbol{r}) = \left(\frac{\kappa_x}{2}\right)x^2 + \left(\frac{\kappa_y}{2}\right)y^2 + U_z$ where κ_x

and κ_y are the coefficients of the effective harmonic potential. U_z is the Zeeman energy and its derivative is give as $-\frac{\delta U_Z}{\delta r} = -cq\boldsymbol{e}_z \times \boldsymbol{H}$ where c is the chirality of the core and $q = \pi\mu_0 M_S L$ (R: the radius of the ferromagnetic disk). In our analyses, only the current-induced Oersted field along the y direction: approximated as $\boldsymbol{H} \sim \frac{2RJ}{\pi}\boldsymbol{e}_y$ is considered as an external field. Geometric relation of each torque applied to the vortex core as a quasiparticle is illustrated in Fig. 2.11 (a) as response of ac current injection. Note that the core rotating direction is decided by the gyrovector $\boldsymbol{G}(p)$, i.e. the sign of the polarity $p = \pm1$: the core rotates toward the counter clockwise direction with $p = +1$ and the
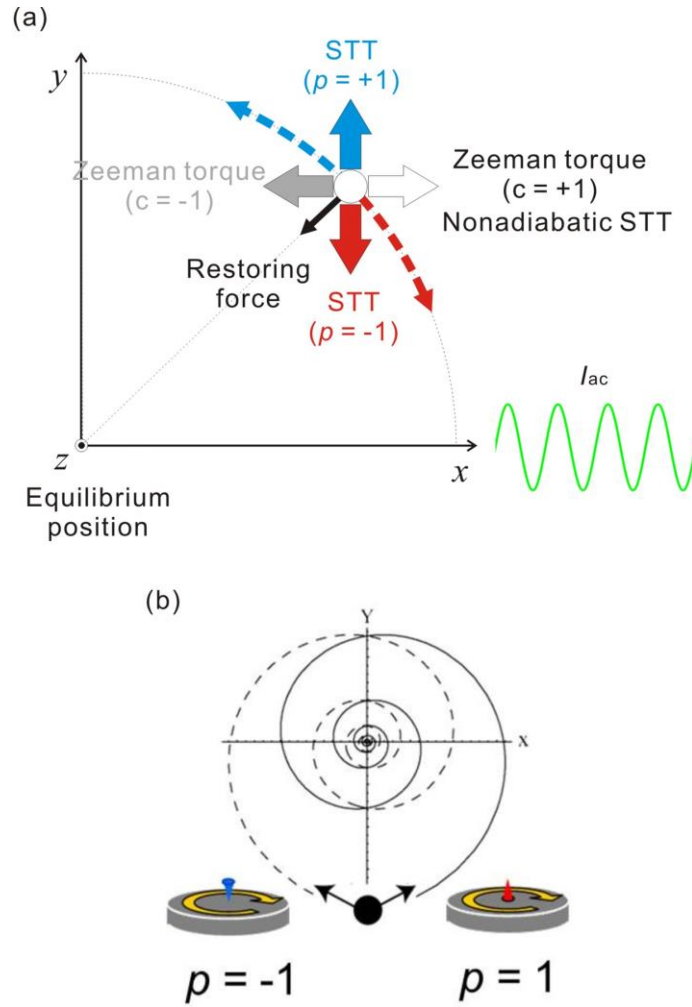
FIG. 2.11: (a) Cartoon of geometric relations of driving forces in current induced harmonic oscillation. (b) polarity-dependent core trajectory at the damping process of the translational mode. There exists a clear relation between current induced spin transfer torques direction and core rotating direction: core rotates counter-clockwise with $p = -1$ and rotates clockwise with $p = +1$

clockwise direction with $p = -1$ keeping right hand rule as shown in Fig. 2.11 (b). The adiabatic spin transfer torque always supports the gyroforce $\boldsymbol{G}(p) \times (-\dot{\boldsymbol{r}})$ and its direction is also switched by

21

a selection of polarity p. On the other hand, Zeeman torque does not depend on polarity p but chirality c. In case of linear ac current injection toward x-axis, current induced Oersted field applied to y-axis and these two torques do not necessarily compete against each other. However in case of rotating current injection[85], a sign of pc is crucial to decide whether the gyroforce and the spin torque are applied opposite direction to the Zeeman torque or not. As a result, suppression of excitation by selecting the sing of pc was reported. Besides, chirality c itself does not affect core dynamics in the translational mode directly but change the stray field distribution (see Sec. 2.7). Note that the parabolic potential U is independent from (p, c) thus these two parameters act as switching the symmetry of magnetization geometry without changing the energy scheme. These features play important roles to determine the coupling energy in chapter 5.

2.6.4. Current-induced harmonic oscillation of the vortex

The vortex system is unique in various domain structures in terms of acting as a current induced harmonic oscillatory system. The core dynamics excited by ac current injection can be analytically solved with starting from Thiele's equation. We assume the vortex core position is also rotate synchronized with excitation current with a frequency ω, as

$$\boldsymbol{r} = \begin{pmatrix} x \\ y \end{pmatrix} = \begin{pmatrix} x_0 + \text{Re}\{Xe^{i\omega t}\} \\ y_0 + \text{Re}\{Ye^{i\omega t}\} \end{pmatrix}. \tag{2.30}$$

Here, (x_0, y_0) is the equilibrium position of the vortex core and (X, Y) is the complex oscillation amplitude. For a small interlude, the equilibrium position (x_0, y_0) under the static field (H_x, H_y) is easily calculated as

$$\begin{pmatrix} x_0 \\ y_0 \end{pmatrix} = \frac{cq}{\kappa} \begin{pmatrix} H_y \\ -H_x \end{pmatrix}, \tag{2.31}$$

The distance of vortex core shift shows the linear response to the static field and shift directions is only depends on the chirality c. We exploit this feature when discussing degenerated degrees of chirality's in coupled system in chapter 5. With assumption of rotating core, we can eliminate the explicitly time dependent part and obtain

$$\begin{pmatrix} \kappa + i\omega\alpha D_0 & -i\omega G_0 P \\ i\omega G_0 P & \kappa + i\omega\alpha D_0 \end{pmatrix} \begin{pmatrix} X \\ Y \end{pmatrix} = \begin{pmatrix} cqh + \beta D_0 u_0 \\ G_0 P u_0 \end{pmatrix}, \tag{2.32}$$

Where h is current induced Oersted field. Therefore we obtain the oscillation amplitude of the core,

$$\begin{pmatrix} X \\ Y \end{pmatrix} = \begin{pmatrix} X' + iX'' \\ p(Y' + iY'') \end{pmatrix}. \tag{2.33}$$

Here, $X'(X'')$ and $Y'(Y'')$ are the x and y component of the real (imaginary) part of the oscillation amplitude. The value of polarity p is required to express the polarity-dependent core gyration. These details are

$$X' = u_0 \frac{\tilde{\beta}\tilde{\kappa}(\omega_\gamma{}^2 - \omega^2) + (1 + \tilde{\alpha}\tilde{\beta})\alpha_*\omega^2}{(1 + \tilde{\alpha}^2)\left\{(\omega_\gamma{}^2 - \omega^2)^2 + (\alpha_*\omega)^2\right\}}$$

$$+ h \frac{c\tilde{q}\left\{\tilde{\kappa}(\omega_\gamma{}^2 - \omega^2) + \alpha_*\tilde{\alpha}\omega^2\right\}}{(1 + \tilde{\alpha}^2)\left\{(\omega_\gamma{}^2 - \omega^2)^2 + (\alpha_*\omega)^2\right\}}$$

$$X'' = u_0\omega \frac{-\tilde{\beta}\tilde{\kappa}\alpha_* + (1 + \tilde{\alpha}\tilde{\beta})(\omega_\gamma{}^2 - \omega^2)}{(1 + \tilde{\alpha}^2)\left\{(\omega_\gamma{}^2 - \omega^2)^2 + (\alpha_*\omega)^2\right\}}$$

$$+ h\omega \frac{c\tilde{q}\left\{-\tilde{\kappa}\alpha_* + \tilde{\alpha}(\omega_\gamma{}^2 - \omega^2)\right\}}{(1 + \tilde{\alpha}^2)\left\{(\omega_\gamma{}^2 - \omega^2)^2 + (\alpha_*\omega)^2\right\}} \tag{2.34}$$

$$Y' = u_0 \frac{\tilde{\kappa}(\omega_\gamma{}^2 - \omega^2) + (\tilde{\alpha} - \tilde{\beta})\alpha_*\omega^2}{(1 + \tilde{\alpha}^2)\left\{(\omega_\gamma{}^2 - \omega^2)^2 + (\alpha_*\omega)^2\right\}}$$

$$- h \frac{c\tilde{q}\alpha_*\omega^2}{(1 + \tilde{\alpha}^2)\left\{(\omega_\gamma{}^2 - \omega^2)^2 + (\alpha_*\omega)^2\right\}}$$

$$Y'' = u_0\omega \frac{-\tilde{\kappa}\alpha_* + (\tilde{\alpha} - \tilde{\beta})(\omega_\gamma{}^2 - \omega^2)}{(1 + \tilde{\alpha}^2)\left\{(\omega_\gamma{}^2 - \omega^2)^2 + (\alpha_*\omega)^2\right\}}$$

$$- h\omega \frac{c\tilde{q}(\omega_\gamma{}^2 - \omega^2)}{(1 + \tilde{\alpha}^2)\left\{(\omega_\gamma{}^2 - \omega^2)^2 + (\alpha_*\omega)^2\right\}}$$

with normalized parameters,

$$\tilde{\alpha} = \alpha\frac{D_0}{G_0}, \;\; \tilde{\beta} = \beta\frac{D_0}{G_0}, \;\; \tilde{\kappa} = \frac{\kappa}{G_0}, \;\; \tilde{q} = \frac{q}{G_0}, \;\; \alpha_* = \frac{2\tilde{\alpha}\tilde{\kappa}}{1+\tilde{\alpha}^2}, \;\; \omega_\gamma = \frac{\tilde{\kappa}}{\sqrt{1+\tilde{\alpha}^2}}. \tag{2.35}$$
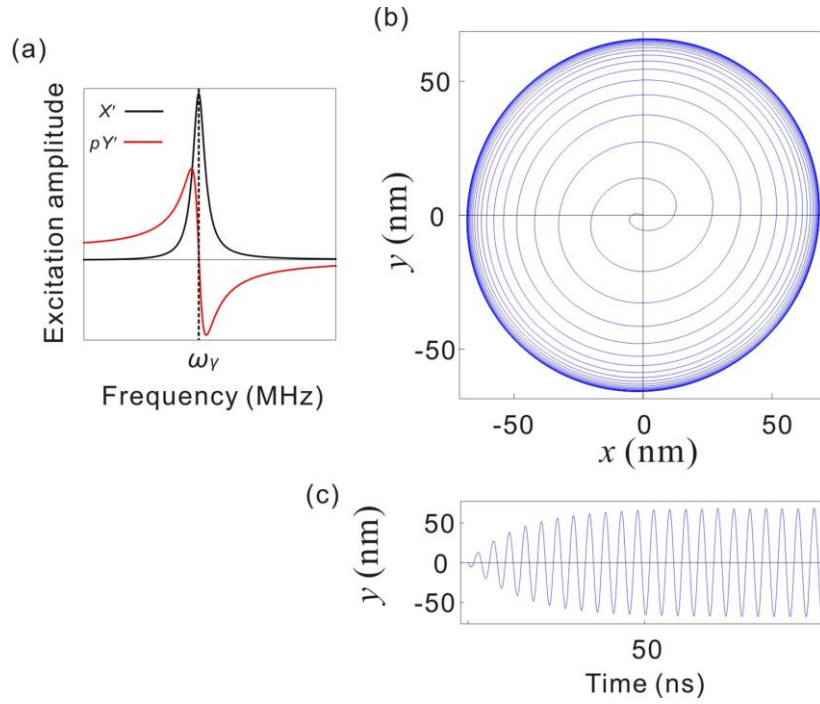
FIG. 2.12: (a) Resonant spectra of real parts of core amplitude (X', Y'). (b) A resonantly excited core trajectory. (c) A resonantly excited time evolution of core position orthogonal to current direction. All results are calculated using Eq. 2.34.

Obviously, frequency ω dependence of the core amplitude (X, Y) shows similarity with that of the magneto susceptibility $\chi = \chi' - i\chi''$ of a single domain structure: where both the imaginary and real parts form symmetric shapes respect to the resonant frequency ω_γ and one of them shapes Lorentzian type symmetric peak and the other does differential function of Lorentzian with weak damping condition $\alpha \ll 1$. This similarity let to know that the core also keep circular trajectory at the resonance condition as a response of ac current (or field) injection. The calculated core dynamics are shown in Fig. 2.12. Using Eq. 2.34, we can derive the time evolutions of core dynamics. Time scale to reach steady excitation is estimated less than 60 ns with $\alpha \cong 0.01$. The length scale is dominantly decided by the excitation efficiency, spin polarization, current amplitude, and efficient constant of parabolic potential. In case of typical permalloy material, required current density is almost comparable with usual values of current-induced domain wall dynamics[86,87,88], typically an order of $10^{10} \sim 10^{11} \text{A/m}^2$, and $50 \sim 150 \text{ nm}$ in an oscillatory radius.

Damping process

These gyrotropic motion of the core in translational mode is also observed at the relaxation process from the core is deflected from the equilibrium position from some kinds of external forces, where the gyroforce $\boldsymbol{G}(p) \times (-\dot{\boldsymbol{r}})$ is the only factor to drive the core toward angular direction. Once deflected and released, the vortex core exhibits a spiral-like motion around its equilibrium position with the sense of gyration determined by the sign of the core polarization p following a right-hand grip rule.

24

In the case of small deflections of the core the approximation of a harmonic potential can be likewise adopted. With the initial condition $\boldsymbol{a}(0) = (0, A_0)$, the core trajectory in both structures can be described as a two dimensional harmonic oscillator[82]

$$\boldsymbol{a}(0) = A_0 \begin{pmatrix} -\sin(p\omega_0 t) \\ \cos(p\omega_0 t) \end{pmatrix} e^{-\Gamma t}, \tag{2.36}$$

where the damping parameter is $\Gamma = \omega_\gamma |(D_0/G_0)|$[82]. Using Eq. (2.19), the eigenfrequency and the damping parameter can be determined from time domain measurement. In this thesis, the damping parameter Γ is experimentally evaluated by means of time resolved Kerr effect measurement in chapter 4.

2.7. Concept of magnetostatic coupling of magnetic vortices

For small interelement distances, the stray field of a neighboring ferromagnetic structure can significantly affect the static magnetization configuration and the magnetization dynamics[89,90,91]. An increase of the initial susceptibility and a decrease of the vortex nucleation and annihilation fields occur in arrays of ferromagnetic disks depending on the element spacing[31]. It has been observed that
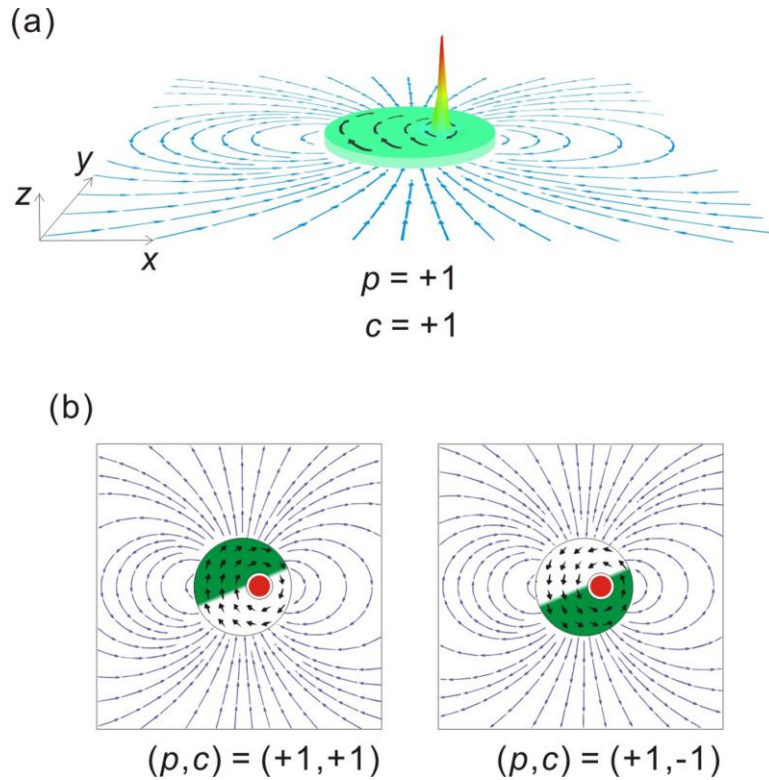

FIG. 2.13: (a) Stray field distribution around a circular shaped ferromagnetic dot with vortex structure. (b) Chirality dependence of stray field distributions.

vortex gyrations can be induced by dipolar interaction between physically disconnected disks in

chapter 5. We introduce our simulation results of stray field distribution around a circular shaped ferromagnet with vortex structure, to discuss spatial symmetry of stray field distributions in Fig. 2.13. And obtain quantitative insights of coupling intensity between separate disks in Fig. 2.14.

When the core positions at the equilibrium (equal to the center of disk in simulations), normally stray field is negligible since side magnetic charges does not appear so as to suppress the magnetostatic energy. Once the vortex core is shifted from the disk center, symmetry breaking results the emergence of side magnetic charges around the side surface. The effect of the perpendicularly standing magnetization at the core region is neglected because of much smaller exchange length than core disk radius $l_{ex} \ll R$. The stray field distributes like single magnetic dipole aligned orthogonal to the shift direction (see Fig. 2. 13 (a)). This similarity of vortex's stray field with linear dipole element is regarded to quantitatively discuss the energetic scheme of coupled vortices in terms of spatial symmetry decided by polarities and chiralities (details are discussed in chapter 5). Note that the stray field distribution is reversed with switching chirality c as shown in Fig. 2.13(b). Chirality c itself does not explicitly affect core dynamics as discussed in Sec. 2.6 but determine the relation of core position and bonding symmetry of coupled system. Thus the value of c becomes crucial parameter to describe the energy scheme of coupled vortices, which is comparable with other two parameters: polarities p_i and the phase difference of two cores $\Delta\Phi$.

Figures 2.14 shows calculated stray field $H_{x,y}$ as functions of distances from the core edge along x-axis (Fig. 2.14 (b)) and y-axis (Fig. 2.14(c)). As comparison, results of ground state (i.e., the core locates at the center of the disk) and excited state (core shifted 165 nm from the center along x-axis). The amplitude of stray filed $|H_{x,y}|$ drastically increases with core shift from the equilibrium position, up to near 100 Oe at zero separate distance. The $|H_{x,y}|$ is not easily to decayed along y-axis compared with x-axis and keep the values around 20 Oe even 600 nm at the separate distance, where the equilibrium position of the neighboring vortex core with same disk radii $R = 500$ nm with core to core distance $D = 1100$ nm. The translational mode in permalloy dots can be excited by ac field with several Oe in field amplitude $|H_{x,y}|$. Therefore stray field of vortex structure is estimated to be enough strong to excite coupled dynamics at neighboring vortex. This type of excitation alignment is experimentally demonstrated as the manner of local excitation, only the left vortex is resonantly excited by ac current and the right vortex is subsequently excited purely by the stray field.
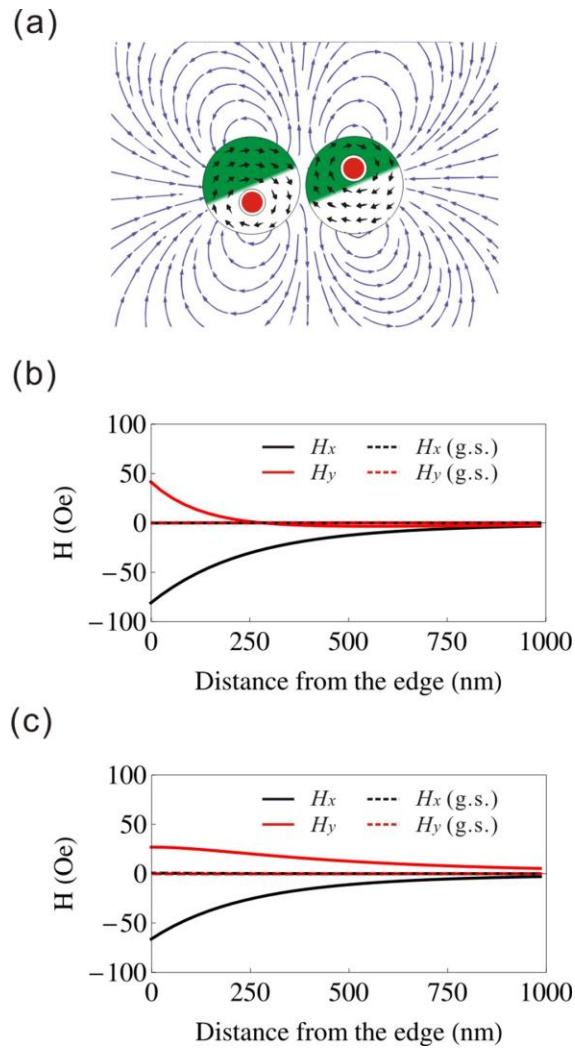
FIG. 2.14: (a) Stray field distribution of two neighboring vortices with center to center distance $D = 1100$ nm and disk radii $R = 500$ nm. (b) and (c) Stray field $H_{x,y}$ as functions of separate distances from the edge of the disk toward *x*-axis (b) and *y*-axis (c). The core shifted around 165 nm along *x*-axis.

2.8. Magnonic crystal

It has been well known that electrons as a de Broglie wave in the periodic crystal potential form an energy band. Analogous to this original idea, the concept of the photonic crystal[92] is denoted as electromagnetic waves in periodic dielectric material. As a subsequently extension, a special energy gap was also investigated in periodic ferromagnetic media. Drawing an analogy from photonic crystals known in optics, such magnetic structures can be called as magnonic crystals. The so-called magnonic crystal is a subject of growing interest owing to its applications to spin wave waveguides, filters[93], attenuators and phase shifters[94]. Due to a rich material selectivity and technological property of ferromagnets, many studies of magnonic crystal have been conducted so far: not only 1 dimensional structures, such as periodic multilayers[95,24], periodic arrays of nanostrips[96], but also 2- or 3 dimensional structures[97,98]. As information carries in magnonic crystal, similar arrays of nanomagnets may be used to propagate high frequency magnetic excitations in the form of collective long wavelength spin waves when the magnetic elements are strongly magnetostatically coupled. Such coupled arrays of nanomagnets undergo a collective dynamics[99,100,101], where the individual nanomagnets maintain constant amplitude and phase relationships, and show rich magnonic band structures with tunable band gap properties.

Neighboring circular disks with magnetic vortices magnetostatically interact each other as calculated in Sec. 2.7, showing vortex in circular dots can be adoptable for unit of above harmonic oscillatory magnonic crystal. Uniquely for magnetic vortices, a special symmetry of interacting stray field can be modulated by polarities and chiralities, suggesting coupled vortices as harmonic oscillatory system shows tunable dispersion relations by not only geometric relation of samples but also changing parts of remanent states, i.e. polarities and chiralities[21,22,23]. Operations of polarity[102,103,104,105,106,107] and chirality[108,109,110] have been a hot topic in vortex study from the early age, and many fruitful works have been reported. Such previous studies help coupled vortices for being possible media of new type of magnonic crystal.

3. Methods

This chapter deals with brief explanations of experimental/simulation methods adopted in this thesis. In Sec. 3.1, a brief overview of the fundamental techniques used for sample preparation is given. The specific sample layout is presented together with the experimental results in chapters 4 − 6, respectively. In Sec. 3.2, principles of two complementary experimental measurement setups, namely, spin torque diode effect, and time resolved magneto optical Kerr effect are introduced. Finally, conditions of micromagnetic simulation are written in Sec. 3.3.

3.1. Sample preparation

Standard clean-room techniques

Samples are fabricated using several steps of the electron-beam lithography and the lift-off processing of positive electron-beam resists onto silicon substrates with a 300 nm silicon-oxide coating. Whole process is illustrated in Fig. 3.1. Firstly, remained surface dusts and organic substances are removed through ultrasonic cleaning processes in acetone or isopropanol (A). Positive resists, positive methyl methacrylate (MMA) and polymethyl methacrylate (PMMA) for electron-beam lithography process or AZ-1500 for photolithography process, are applied uniformly in thickness with spin coat and subsequent bake processes (B). These resists are developed in a wet-chemical process after exposure, and 2 dimensional resist masks of structure are obtained (C). For ferromagnetic nanostructures, polycrystalline permalloy ($Ni_{80}Fe_{20}$) is deposited via electron beam evaporation. For striplines, coplanar waveguides, and contact pads, gold or copper are deposited via thermal evaporation, respectively (D). To prevent a removal of an entire gold layer during lift-off processing, a 5 nm titanium adhesion layer is preliminarily prepared in situ condition. For some cases, alumina as insulator is prepared at the interlayer between permalloy and waveguides by rf-magnetron sputtering process. In the case of current excitation circuit, the interface of ferromagnets and contact pad is cleaned via argon rf-plasma etching before deposition to obtain clear interfaces and to prevent possible perturbation of the magnetization dynamics by an antiferromagnetic layer which could be formed via oxidation of the permalloy surface during the preparation process. Patterned masks are finally removed by clean process (E). For detailed process parameters of fabrication steps are shown see appendix A.
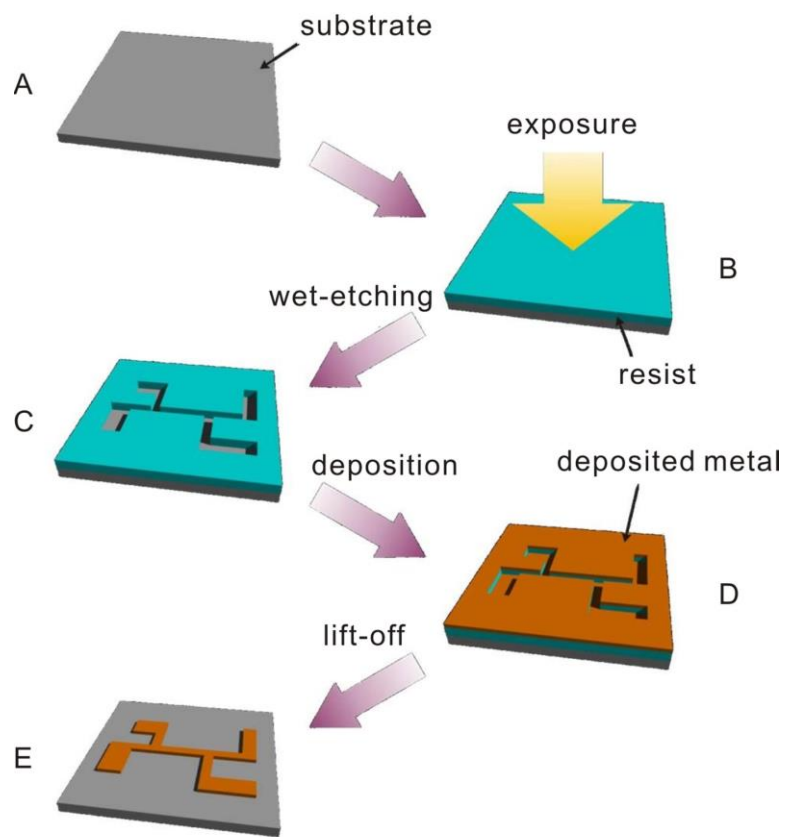
FIG. 3.1: Schematic illustration of lithography and lift-off processing of positive resist.

3.2. Measurement techniques

3.2.1. Spin torque diode effect

Current- or field-induced magnetization dynamics of vortex structures were studied by exploiting spin torque diode effect in frequency space. Spin torque diode effect was first observed as the reversal process of the active oscillation of CoFeB/MgO/CoFeB magnetic tunnel junction[28] and GMR[29]. Spin dynamics excited by microwave generates large amplitude of dc voltage proportional to magnetoresistance ratio. When there exist a cone angle θ_0 between the free layer and the fixed layer, microwave current with frequency ω resonantly excites the magnetizations at layers by spin transfer toque. In this process, both the cone angle $\theta = \theta_0 + \Delta\theta \sin(\omega t + \delta)$ and flowing current $I = I_0 \sin \omega t$ sinusoidally oscillate with same frequency ω. The former cause magnetoresistance also oscillate with frequency ω thus a time integrated voltage $V(t) = IR$ results in finite value $V_{dc} \propto I_0 \Delta\theta \sin \theta_0 \cos \delta$. The sensitivity of the spin torque diode is given as below.

$$\epsilon = [V_{dc}]_{max}/P_{inc} \propto (MR/\sigma)\sin^2\theta \qquad (3.1)$$

Here P_{inc} is injected power, MR is magnetoresisitance ratio, σ is resonant line width and θ is the cone angle between the free layer and the fixed layer. The spin diode effect is a kind of ferromagnetic resonant measurement thus physical parameters of dynamics can be determined, such as damping constant or exchange coefficient. The spin torque diode effect in this thesis is exploited to study the translational mode of the magnetic vortex and detection principles are discussed in Sec. 4.1.

Design of microwave circuit

The frequencies of interest are typically in the microwave range. Since the wavelength of a MHz to GHz signal is comparable to the dimensions of the measurement setup (10 to 100 cm), the radio-frequency signals have to be considered as electromagnetic waves. Transmission-line theory applies and effects of signal reflection, scattering, and diffraction become of practical significance. To avoid signal attenuation due to backscattering of the electromagnetic waves used to excite and to
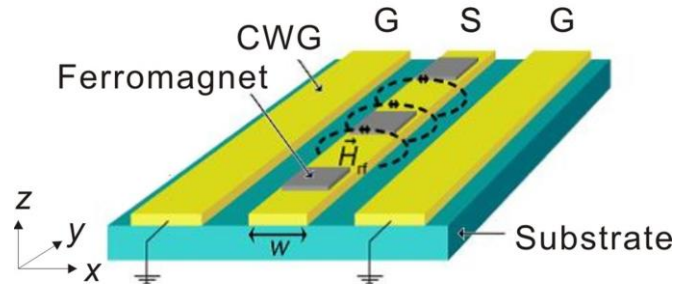

FIG. 3.2: Diagram of a typical on top coplanar waveguide with microstructures. Dashed lines illustrate the magnetic field lines around the central conductor (S).

detect the magnetization dynamics, a coplanar waveguide (CPW) is used to drive rf signal through the

sample (Fig. 3.2). Its geometry is optimized to match the industrial standard microwave impedance of $Z_0 = 50\,\Omega$ considering the material of the CPW and the substrate with its characteristic dielectric constant[i]. A signal generator (Agilent N5181A) serves as source and detector for the sinusoidal rf signal (100 kHz to 6 GHz) which causes a rf magnetic field $H(t)$ around the central conductor. Without considering the Skin effect, the achievable rf field in the plane of the ferromagnetic structures is approximately $H(t) = I(t)/2\omega \cdot e_x$[111], where $I(t)$ is the rf current flowing through the central conductor and ω is the width, denoted in Fig. 3.2.

For field excitation circuit, the ferromagnetic structures are placed below or on top of the central conductor, and CPW can be designed exact dimension with $Z_0 = 50\,\Omega$. However for current excitation circuit, there exist geometric limitations since the signal line (S) have to be directly connected to the permalloy disks whose resistance is much higher than those of electrode. For calibration of the inevitable impedance mismatch, the excitation circuit are connected to a directional bridge (Agilent 86205A) to estimate return loss of the injected current (see details in Appendix. B).

Samples are placed in the homogeneous part of a controllable static magnetic field H_0 (up to about 1000 Oe) which is generated between the four two shoes shown in Fig. 3.3. The CPW is contacted via
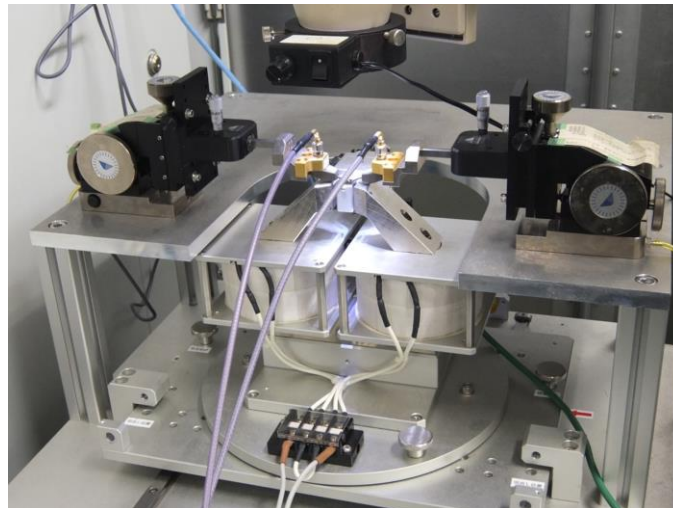
FIG. 3.3: A Picture of rf probe station for spin torque diode measurement set up

rf microprobes (CASCADE GSG (SG, GS)-150), see photograph in Fig. 3.3. An optical microscope and micropositioners provide micrometer-precise positioning of the probes onto the sample. The whole setup is placed on a vibration-cushioned table to minimize the noise due to mechanical changes. The present setup enables to sweep the frequency of the exciting rf field or current for a constant external magnetic bias field H_0. Repeated frequency sweeps lead to an improved signal-to-noise ratio. To eliminate the noise and frequency response coming from the experimental setup, a reference sweep

---

[i] The free transmission line calculator AppCAD[TM] is used to determine the matching CPW geometry.

is performed at a predefined bias field H_0 (saturation of the sample to single domain structures in this thesis).

3.2.2.Time resolved magneto-optical Kerr effect

Magneto-optical Kerr effect

Field-induced damping process of vortex structures was studied by exploiting time resolved-magneto-optical Kerr effect. Even though magneto-optical Kerr[30] effects (MOKE) were discovered about 200 years ago, they continue to be useful techniques for nondestructive investigation in current spintronics[39]. The fundamental phenomenon of MOKE is the rotation of the plane of polarization of a plane polarized light upon reflection from the surface of a magnetic material. A linearly polarized light is reflected as an elliptically polarized light, and the Kerr rotation and ellipticity give a measure of the magnetization property. There are three important MOKE geometries, namely, the polar, longitudinal, and transverse MOKE, which are defined according to the relative orientation of the plane of incidence with the magnetization $\boldsymbol{M}$ in the sample as shown in Fig. 3.4.

Consider the polar case in Fig. 3.4 (a) with linearly *p*-polarized light. This injected light induces oscillation of electrons in the sample surface along polarized electric field $\boldsymbol{E}$. In addition to the regular reflected light $\boldsymbol{r_n}$ the Lorentz force on the oscillating electrons induces small vibration perpendicular to the magnetization $\boldsymbol{M}$. This secondary electron oscillation $\boldsymbol{v}$ radiates to create the small Kerr reflected component $\boldsymbol{r_k}$. As a consequence, the vector sum of the reflected light is thus rotated in its polarization direction due to the sample magnetization. Such rotational direction differs by given magnetization and the geometry of MOKE. In case of polar alignment, both s- and p- polarized lights gives identical Kerr rotation.

For longitudinal alignment, *p*-polarized light induces the Lorentz motion $\boldsymbol{v}$ in the plane (Fig. 3.4 (b)) whereas *s*-polarized light cause the Lorentz motion $\boldsymbol{v}$ perpendicular to surface and results in opposite Kerr rotation from *p*-polarized case, as shown in Fig. 3.4 (c).

For transverse orientation in Fig. 3.4 (d), where the magnetization $\boldsymbol{M}$ is perpendicular to the plane, the s-polarized light gives no effect and the p-polarized light give Kerr reflected component $\boldsymbol{r_k}$ in the same direction as the regular reflected light $\boldsymbol{r_n}$. Therefore, the transverse effect gives an amplitude variation instead of Kerr rotation.

The major axis of the ellipse is slightly rotated with respect to the principal plane and is referred to as the Kerr rotation as shown in Fig. 3.5. The flatness of the ellipse is quantified as the Kerr ellipticity. The Kerr rotation θ_K and ellipticity ε_K can be expressed as

$$\theta_K + i\varepsilon_K = r_k/r_n \qquad (3.2)$$

when $k \ll r$[112]. In experiments of this thesis, the Kerr rotation of longitudinal orientation has been measured to track time evolution of the magnetization.
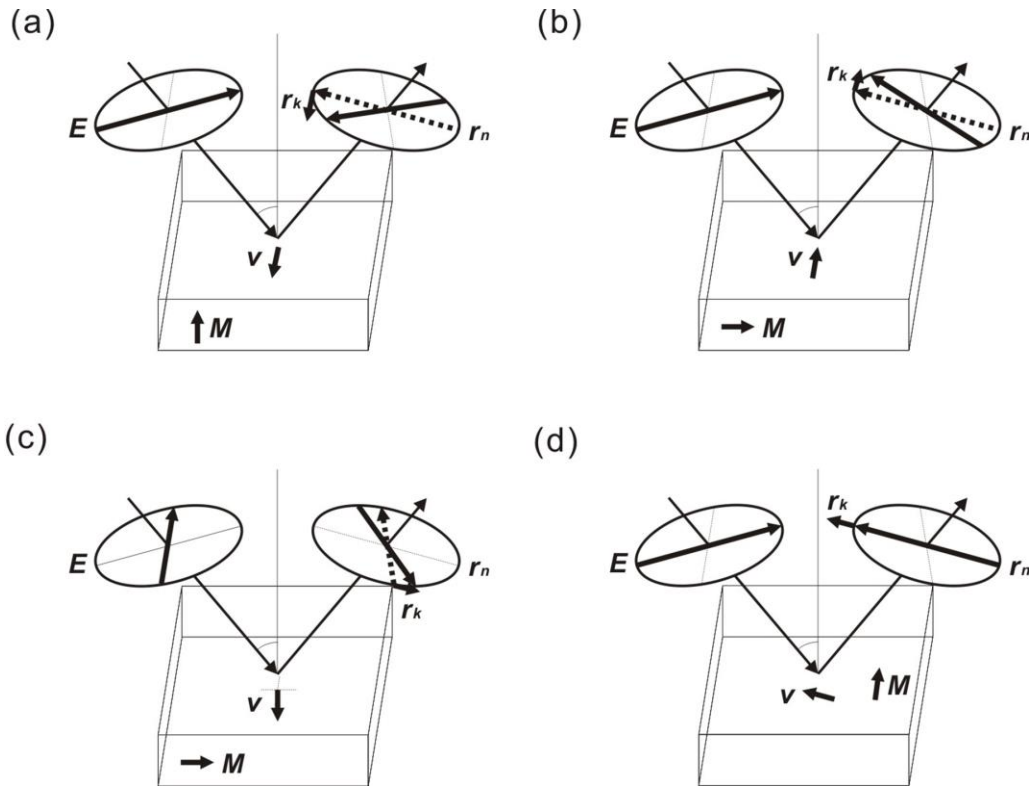
FIG. 3.4: Schematic images of (a) polar, longitudinal for (b) *p*-polarized and (c) *s*-polarized, (d) transverse MOKE geometries. (d) Geometry of the Kerr rotation θ_K and ellipticity ε_K is shown. Here, **E** is polarized electric field, r_n is the regular reflected electric field, r_k is the additional field component owing to the magneto-optic effect, and **v** shows the Lorentz motion of secondary electron.

The measurement of Kerr rotation is performed by analyzing the polarization state of the reflected light, by using an optical bridge detector consisting of a polarized beam splitter and two photodiodes.
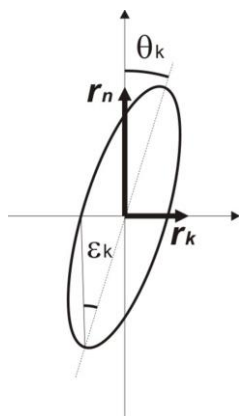
The difference in the signal between the two photodiodes is proportional to the Kerr rotation[113]. The Kerr rotation modifies the intensities in the two orthogonal components of polarization and gives rise to a finite electronic signal at the output of the optical bridge detector

FIG. 3.5: Geometry of the Kerr rotation θ_K and ellipticity ε_K is shown.

Benchtop type of time resolved magneto-optical Kerr magnetometer

Our measurement set up is based on "benchtop" type of Kerr magnetometer developed by Barman *et al.*[114], where all optical apparatus are placed on small shield box and time resolution is given by electrical modulations of signals (see Fig. 3.6 (a)). The pump probe-approach was adopted here: measurement system is built upon a picosecond pulsed injection diode laser (for probe light source) and electronic pulse generator (for pumping). Polarized optical pulses is synchronized to the electronic pulses with changing time delay of two pulses by using a variable electronic delay generator (Colby Instruments PDL30A) with total delay of 40 ns at 0.5 ps time step. The synchronization scheme is shown in Figs. 3.6 (b).

A pulsed injection diode laser (Advanced Laser diode system PIL040) with central wavelength of 408 nm, pulse width of 42 ps, spectral width of 7 nm, repetition rate of up to 1 MHz, and peak power of 1.3 W is used for the MOKE measurements. The dynamic measurements need the launching of an ultrafast magnetic field pulse to the sample. We have used an electronic pulse generator (Picosecond Pulse Labs 10,060A) with rise time of 55 ps, variable duration from 100 ps to 10 ns, and +10 V maximum signal to achieve this.

(a)

(b)
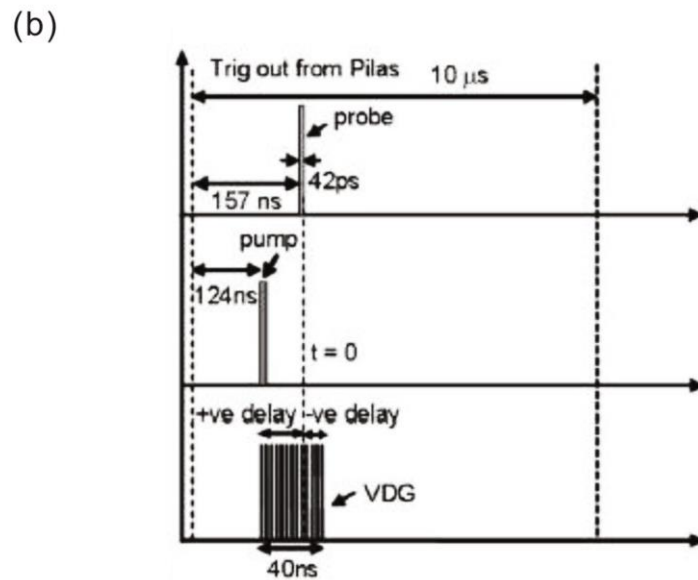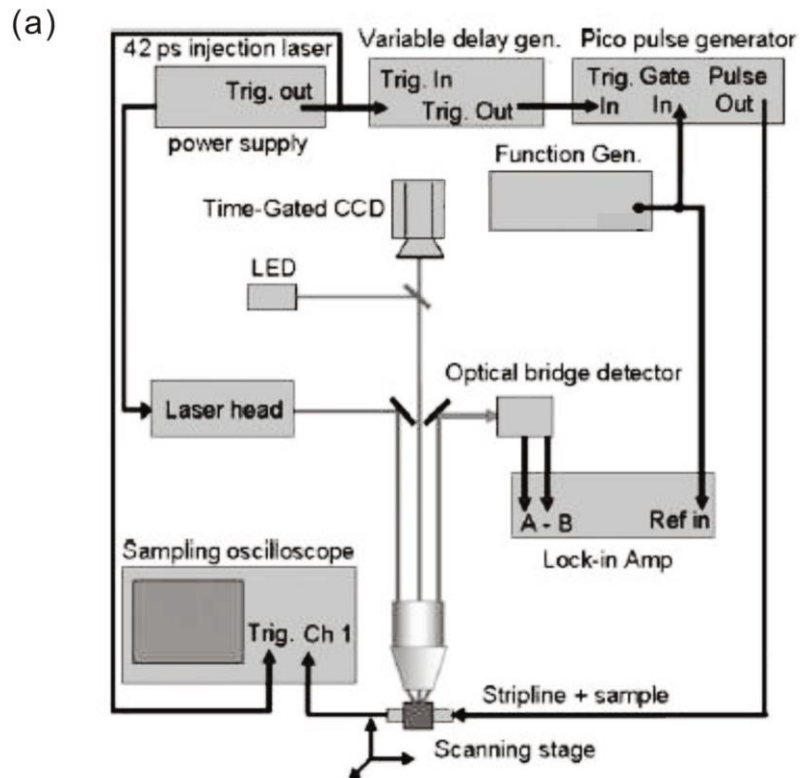
FIG. 3.6: (a) The schematic illustration of the time resolved-MOKE magnetometer with electrical delay line. (b) The synchronization scheme between the pump and probe pulse. Figs. (a) and (b) are modified from ref.114.

3.3. Micromagnetic simulations

Micromagnetic simulations were performed to obtain insights of time evolutions of real space magnetization dynamics quantitatively. The continuous magnetization configuration of ferromagnet is divided into exchange length unit cells with single domain structure, and magnetization dynamics of each cell is calculated using LLG equation in Eq. 2.21. Here the exchange field $\boldsymbol{H}_{\text{ex}}$, the external field $\boldsymbol{H}$ (including current induced Oersted field), and the demagnetization field $\boldsymbol{H}_{\text{d}}$ were calculated as the effective field $\boldsymbol{H}_{\text{eff}}$ Simulations were performed using LLG micromagnetic simulator[115]. Typical parameters used for calculations are listed in Table A.

Physical quantity	Symbol	Value
Unit cell size[ii]	Δ	$5 \times 5 \times 30\ nm^3$
Polarization	P	0.4
Saturation magnetization	M_{S}	8.6×10^5 A/m
Exchange constant	A	1.3×10^{-11} J/m
Anisotropy constant	K	0
Gyromagnetic ratio	γ	$1.76 \times 10^{11}\ \text{s}^{-1}\text{T}^{-1}$
Gilbert damping constant	α	0.01[iii]
Nonadiabatic coefficient	c_J	0
Iteration time	Δt	250 fs

Table. Parameters for micromagnetic simulations

[ii] 2 dimensional calculation: magnetization distribution along z-axis was neglected.

[iii] For calculations of remanent states, $\alpha = 1.0$ was chosen for efficiency of the calculation time.

4. Studies of particle like dynamics of the magnetic vortex

In preparation for coupled magnetic vortices, studies of the single magnetic vortex are once discussed in this chapter, by means of frequency domain measurement (Sec. 4.1 and 4.2) and time domain measurement (Sec. 4.3). In Sec. 4.1, theoretical studies and micromagnetic simulations of dc rectified voltage associated with core oscillation are discussed. In Sec. 4.2, current- and field-induced core gyrations are experimentally studied by means of electrical frequency sensor. Besides, Sec. 4.4 deals with studies of time evolutions of core dynamics by means of time resolved magnetometer.

4.1. Spin torque diode effect associated with vortex dynamics.

The translational mode is associated with only exchange length scale vortex core, typically less than 10 nm for permalloy. Therefore it is not easy to detect single core gyration of vortex structure. First observation of time evolution of vortex gyration was reported by Choe *et al.*[15] by means of time resolved x-ray imaging exploiting x-ray magnetic circular dichroism (XMCD)[116,117] effect. The absorption at the L_2- and L_3-edge of cobalt in the permalloy alloy was targeted in this method. Since then, x-ray imaging technique has been one of the strongest tools to study nano-scale magnetization dynamics comparable with exchange length scale[68,69,] as highly sensitive and non-destructive measurement method. However, such soft x-ray measurement requires extensive synchrotron radiation facilities thus there exist large gap to be mounted on actual devices. Therefore development of electrical measurement is still meaningful in terms of the future applicational area. The first electrical frequency domain observation of the vortex core dynamics was reported by using broadband ferromagnetic-resonance measurements by Novosad *et al.*[16]. However, in this technique signal amplitude of a single vortex dynamics is usually too small to detect and an array of vortices is necessarily required to enhance the signal. Note that with arrayed elements, it is technically difficult to determine the configurations of polarities and chiralities (p_i, c_i), those can directly tune the core dynamics and magnetic dipolar interaction. Therefore it is not suitable to adopt broadband ferromagnetic-resonance measurements for coupled vortices, the agenda of this thesis. Among electrical methods, a frequency sensor via spin torque diode effect is applicable to detect signals of the translational mode for a single vortex state. As briefly mentioned in Eq. 3.3, signal amplitude of spin torque diode effect is proportional to the magnetoresistance ratio of samples MR thus a multilayer with large giant[11] or tunnel[18] device structure can be proper way to enhance diode signal. Even though with small magnetoresistance MR of AMR, several percents of material resistance, rectified voltage detected thorough spin torque diode effect can be enhanced by inserting strong shape anisotropy enough to pick up signals of single magnetic vortex. Exploiting such AMR based spin torque diode

effect is quite conventional method for fabrication and detection, and also appropriate to detect exact dynamics without preparing any interlayer couplings. In this thesis, details of AMR based spin torque diode effect are first studied to establish electrical measurement system for the translational mode.

The ac current injection exerts linear oscillatory spin transfer torque and current induced Oersted field on the vortex structure. Under the condition for resonance, the vortex core rotates around its equilibrium at the resonant frequency as a harmonic oscillator synchronized with the ac exciting current. This periodical change in the core position further results in the oscillatory AMR of in-plane magnetization. When the position of the core $r = (x, y)$ is shifted from the center of the disk (x_R, y_R), the resistance of the disk accommodating the vortex is approximated[76] as

$$R = R_0 - a_x(x - x_R)^2 + a_y(y - y_R)^2, \tag{4.1}$$

Here proportionality constant (a_x, a_y) has the unit of Ω/m^2. Substituting current synchronized core oscillation in Eqs. 2.30 and 2.33 into Eq. 4.1, the time evolution of resistance $R(t)$ is obtained as a function of core position r,

$$R(t) = R_0 - a_x\{(x_0 - x_R)^2 + X'^2\cos^2\omega t + X''^2\sin^2\omega t + 2(x_0 - x_R)X'\cos\omega t \tag{4.2}$$
$$-2X'X''\cos\omega t \sin\omega t - 2(x_0 - x_R)X''\sin\omega t\}$$
$$+a_y\{(y_0 - y_R)^2 + Y'^2\cos^2\omega t + Y''^2\sin^2\omega t + 2p(y_0 - y_R)Y'\cos\omega t$$
$$-2Y'Y''\cos\omega t \sin\omega t - 2p(y_0 - y_R)Y''\sin\omega t\}.$$

Here, two different ac current for rectification are considered: first order harmonic detection using current synchronized just with core gyration $I(t) = I_{ac2}e^{i\omega t}$ and second order harmonic detection using current with two times faster than core gyration $I(t) = I_{ac2}e^{i2\omega t}$. Assuming symmetric system $(a_x = a_y = a)$, and using the trigonometric formula, the rectified dc voltage $(V_{dc} = \int dt I(t)R(t))$ is derived as,

$$V_{dc,1f} = -aI_{ac2}[(x_0 - x_R)X' - p(y_0 - y_R)Y'] \tag{4.3}$$

for first order harmonic detection with $I(t) = I_{ac2}e^{i\omega t}$ and

$$V_{dc,2f} = (aI_{ac2}/4)[Y'^2 - Y''^2 - (X'^2 - X''^2)] \tag{4.4}$$

for the second order harmonic detection with $I(t) = I_{ac2}e^{i2\omega t}$. The practical core position (X, Y) is analytically calculated from the Thiele's equation in Eq. 2.29. As can be seen in Eq. 4.3, the rectified dc voltage $V_{dc,1f}$ of first order harmonic detection takes a finite value only when there exists a finite difference between the equilibrium position and the center of the core $(x_0, y_0) \neq (x_R, y_R)$. To support understanding of this point, Figure 4.1(a)-(c) shows time evolutions of excitation current, AMR and voltages obtained from micromagnetic simulations and analytical model of Eqs. 4.1 - 4.4. The relationship between the core positions and the AMR oscillation is illustrated in Figs. 4.1 (d). The AMR rise up to the maximum when the core shifts orthogonal to the current direction (A), and fall to the minimum when the core moves parallel (C). One can notice the majority of in-plane magnetization aligns parallel to the current in the former configuration (A) whereas averaged magnetization aligns orthogonal to the current (C), thus the relation between the core position and magnetoresistance can be understood using same frame with AMR of single domain structure introduced in Sec. 2.5. These results show that the period of the AMR oscillation ($T_a = \frac{2\pi}{2\omega}$) is half of that of the translational mode

$(T_t: 2T_a = T_t = \frac{2\pi}{\omega})$. Thus it seems to be normally hard to obtain finite rectified dc voltages by means of the first order harmonic detection with $I(t) = I_{ac2}e^{i\omega t}$ owing the period of the current $(\frac{2\pi}{\omega})$ does not coincide with the value of T_a at the resonant condition of TM $(\frac{2\pi}{\omega} = T_t \neq T_a)$. However, only when asymmetry of core trajectory as a small displacement, that is equal to $(x_0, y_0) \neq (x_R, y_R)$ in Eq. 4.3 is introduced, the rectified voltage is detectable: time average of $V_{dc2,1f}$ (a blue line in the bottom graph) in Fig. 4.1 (c) turns to be a finite value. Such an asymmetric gyration was usually introduced by
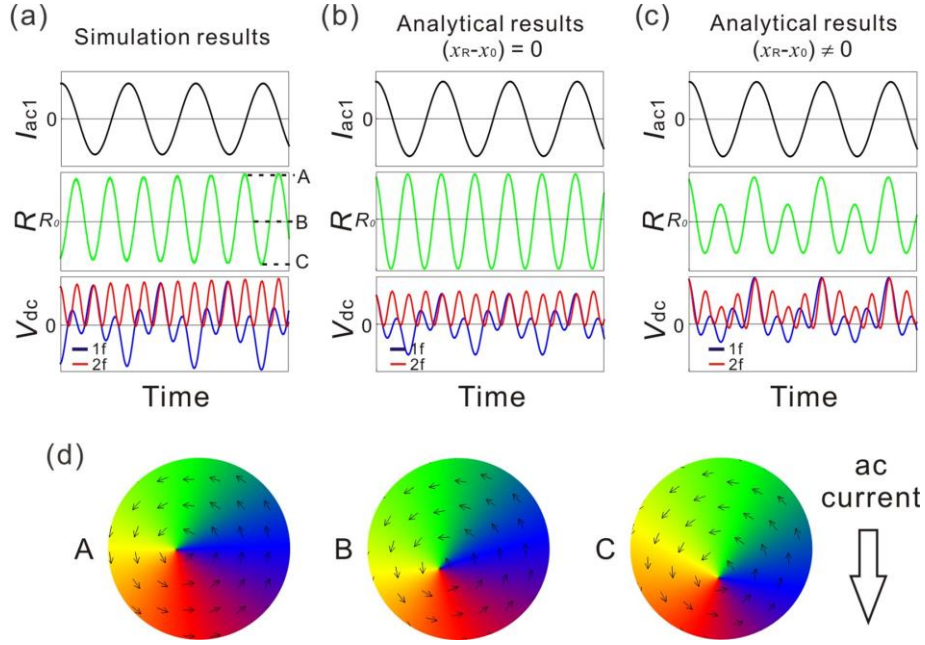

FIG. 4.1: (a)-(c) Time evolutions of the detection current I_{ac2}, ferromagnetic resistance R and rectified voltages $V_{dc2} = I_{ac2} \times R$ under the resonant condition of the translational mode calculated from different methods, from (a) micromagnetic simulation, and (b)-(c) analytical calculations. The 1st and 2nd order harmonic voltages are plotted by blue and red lines respectively. The core trajectories of (a) and (b) draw symmetric circles around the equilibrium position whereas a displacement from equilibrium $(x_0 - x_R)$ is set to be 150 nm in (c). (d) Positions of the vortex core at the maximum (A), the zero value (B), and the minimum (C) of AMR in micromagnetic simulations.

applying in-plane the bias field or making intentional asymmetry in device structure[76,87,88]. In these manners, when the frequency of the ac current is synchronized with the "original" AMR oscillation $T_a = \frac{2\pi}{2\omega}$, that is two time faster than the translational mode, large rectified voltages should be expected with or without breaking symmetry of the core trajectory. We here demonstrate both the first order

AMR oscillation (experimentally single radio frequency signal is required thus we call it "homodyne detection" in the thesis) and the second order harmonic oscillation (In the same manner, we call it "heterodyne detection" here).

4.2. Study of electrical detection of harmonic oscillation of the vortex core

4.2.1. Measurement circuit and device structure

The schematic illustration of our spin torque diode frequency sensors is shown in Fig. 4.2: the measurement circuits for homodyne detection (Fig. 4.2 (a)) and heterodyne detection (Fig. 4.2 (b)) are basically identical except for the existence 2nd coplanar type of wave guide antenna for heterodyne
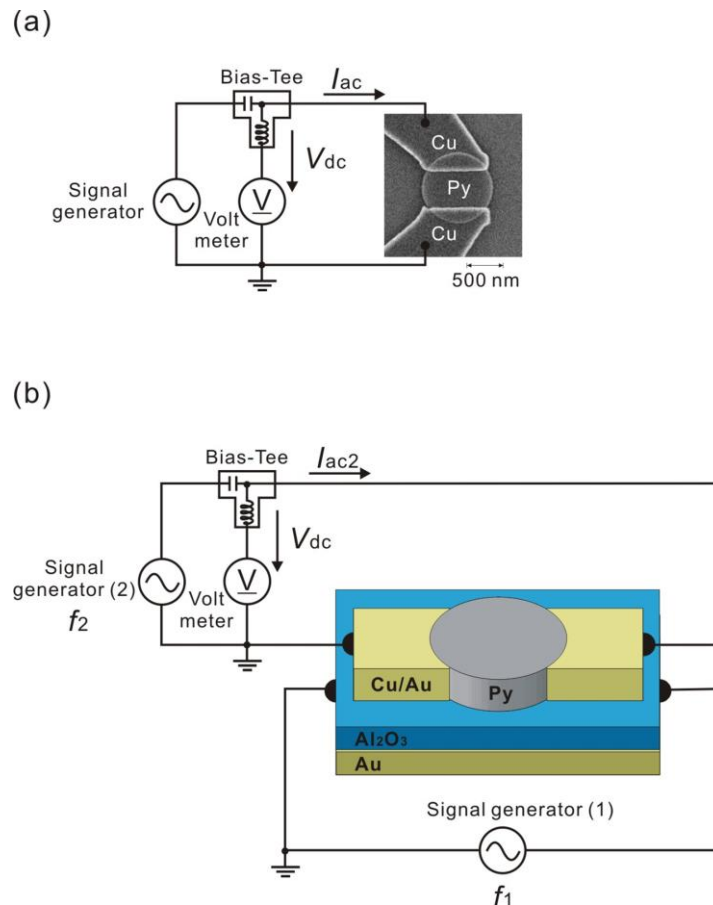

FIG. 4.2: The measurement circuit diagram of (a) homodyne detection with a SEM image of a sample and (b) heterodyne detection including a schematic illustration of the device structure. Two different rf sources (Signal generator 1 & 2) are used for excitation (1) and detection (2).

detection. The magnetic vortex structures were confined in circular shaped permalloy disk with R in radius and L in thickness. The remanent state of magnetization structure was examined through observation of hysteresis loops[31] and by MFM[13] (see Fig. 4.3). The vortex state is confined as the remanent state of field sweepings from 1000 Oe to 0 Oe (in-plane) or from 3000 Oe to 0 Oe

(perpendicular to plane). The copper (50 nm)/titanium (5 nm)/gold (150 nm) electrodes for current injection are attached along *y*-axis. For heterodyne detection, 2nd excitation circuit was fabricated from titanium (5 nm)/gold (150 nm) with a 50 nm alumina insulating layer. For homodyne detection circuit,

(a) $p=-1$: down   (b) $p=+1$: up

(c)
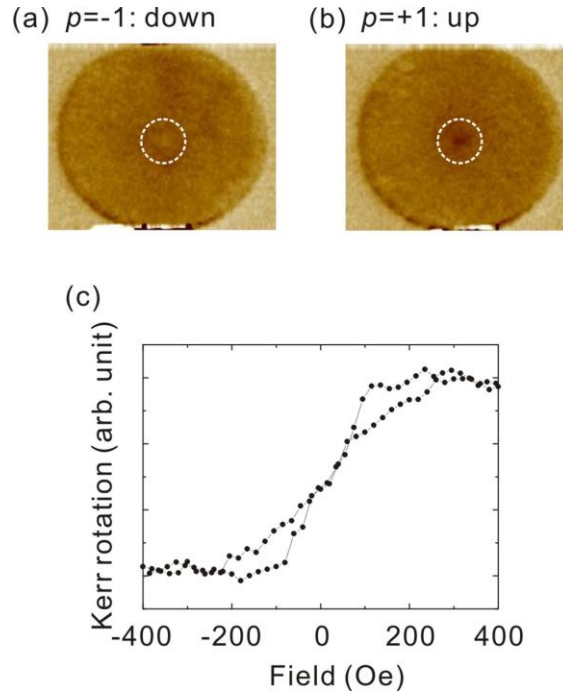
FIG. 4.3: (a) and (b) MFM image of vortex confining permalloy dots. The sign of polarity $p = -1$ (a) or $p = +1$ (b) can be decided from the color of a center point. (c) A hysteresis loop of vortex structure with $(R, L) = (1500 \text{ nm}, 30 \text{ nm})$. Different from typical hysteresis loop of single domain structure of soft ferromagnet in Fig. 2.1 (b), 2 separated loops are appeared due to the difference of the nucleation (~ 80 Oe) and the annihilation field (~ 220 Oe) of the magnetic vortex[31].

a signal generator (Agilent N5181A) is connected to a Bias Tee (KEYCOM KDC-H5004G-01) and ac component of injected power as an excitation current I_{ac} was injected to the sample with a permalloy disk embedded in CWG. Parallely dc component V_{dc} as the rectifying voltage was measured by means of diode detective. The lock in technique was adopted at room temperature. Experimental circuit for heterodyne detection (Fig. 4.2 (b)) includes two independent signal generators, signal generator (1) in the field excitation circuit and signal generator (2) in the detection circuit. Injected ac current I_{ac1} and I_{ac2} were precisely monitored using 7 GHz sampling oscilloscope (Tektronix TDS7704B) by exploiting return loss set up in Appendix B so as to keep the phase relation of the detection current and the excitation field coordinated. The calibration error in phases was estimated less than 0.02π. This phase coordination technique was father adopted for measurements of coupled vortices in chapter 5 and 6.

4.2.2. Resonant spectra of core gyration mode

Figure 4.4 shows resonant spectra of rectified dc voltage $V_{dc,1f(2f)}$ normalized by flowing current, I_{ac} for homodyne detection and I_{ac2} for heterodyne detection, as functions of frequency of detection circuit. These results were obtained under the zero magnetic field. For heterodyne detection, the excitation frequency (f_1) was set at the half of the detection frequency (f_2). The clear peaks are observed around 238 MHz for homodyne detection (Fig. 4.4(a)) and the its doubled value, 471 MHz, for heterodyne detection (Fig. 4.4(b)), respectively. Values of the resonant frequency precisely coincide with the eigenfrequency of the translational mode introduced in Sec. 2.6. The reason of finite rectifying voltages $V_{dc,1f}$ in Fig. 4.4 (a) is due to asymmetry of the inevitable device structure caused
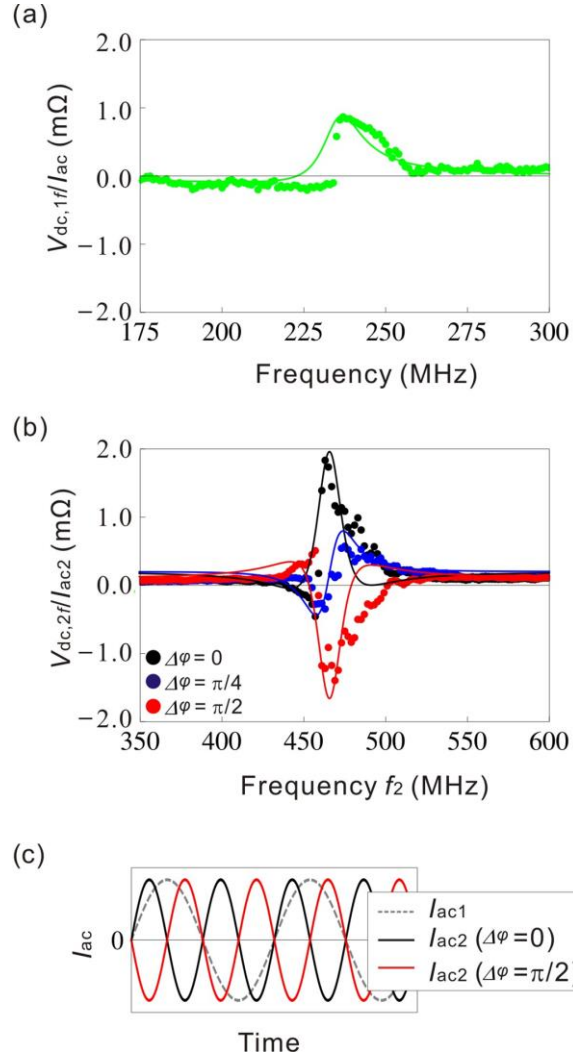

FIG. 4.4: (a) The first order rectified voltage $V_{dc,1f}$ for homodyne detection and (b) the second order rectified voltage $V_{dc,2f}$ for heterodyne detection as a function of the frequency of detection current. The detection current I_{ac2} was set to be 1.6 mA. The excitation field in (b) was estimated as $H = (2.1 \pm 0.5)$ Oe. The solid curves show fitting results using Eq. 4.3 for (a) and Eq. 4.4 for (b). (c) Definition of the phase relation $\Delta\varphi$ between detection and excitation current in (b).

by the attached electrodes, i.e. $(x_0, y_0) \neq (x_R, y_R)$ as listed in Table B. The small tailing in Fig. 4.4 (a) also has same origin. Finite core shift from orthogonal to current direction $y_0 - y_R \neq 0$ adds Y' component, which takes differential function of symmetric peak at the resonant frequency, onto X' component, which forms symmetric peak as introduced in Fig. 2.12 (a). Therefore, resonant spectra become a sum of symmetric and asymmetric peaks and results in tailing depending on the asymmetry of system $(x_0 - x_R, y_0 - y_R)$. In addition, current induced Oersted field is the other factor for tailing since effective phase difference between core oscillation (resistance oscillation) and ac current. Apart from homodyne detection spectra, symmetric peak is observed in heterodyne detection since resonant spectra of second harmonic detection does not directly affected by the asymmetry of system $(x_0 - x_R, y_0 - y_R)$. The phase relation between I_{ac1} and I_{ac2} is shown in Fig. 4.4 (c). In cases when the phase difference between detection current and excitation field ($\Delta\varphi$) switches from in-phase ($\Delta\varphi$ = 0) to opposite phase ($\Delta\varphi = \pi/2$), signs of $V_{dc,2f}$ at the peak reverses respect to the zero voltage. It assures spectra come from projection of detection current into the AMR oscillation. The continuous phase dependence is shown in Fig. 4.5.
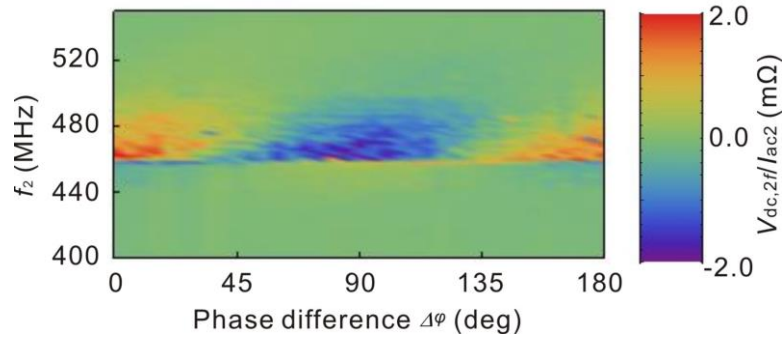

FIG. 4.5: Rectifying voltage for heterodyne detection as functions of detection frequency and phase difference$\Delta\varphi$. Measurement conditions are same with Fig. 4.4(b).

Field tuning of rectifying spectra

Further insights of rectifying spectra can be obtained by tuning the core position using in-plane external field. The energy of vortex system is described by a sum of the demagnetization energy, the exchange energy and the Zeeman energy thus its eigenfrequency is somehow tunable by applying static field or engineering material shape. Here we demonstrate in-plane field H_s tuning as far as keeping particle like motion describable in Thiele equation. Figures 4.6 show the in-plane field dependencies of resonant spectra for homodyne detection (a) and heterodyne detection (b). With increasing external field H_s, the core is driven to a direction to increase parallel component to external field of in-plane magnetization of the vortex, i.e. the core shifted orthogonal to the external field direction and its direction is switched by changing chirality. Subsequently, the value of the resonant frequency monotonically increases with H_s due to the additional Zeeman energy. Since we adopted

in-plane symmetry disks for samples, the resonant frequencies increase with respect to the zero
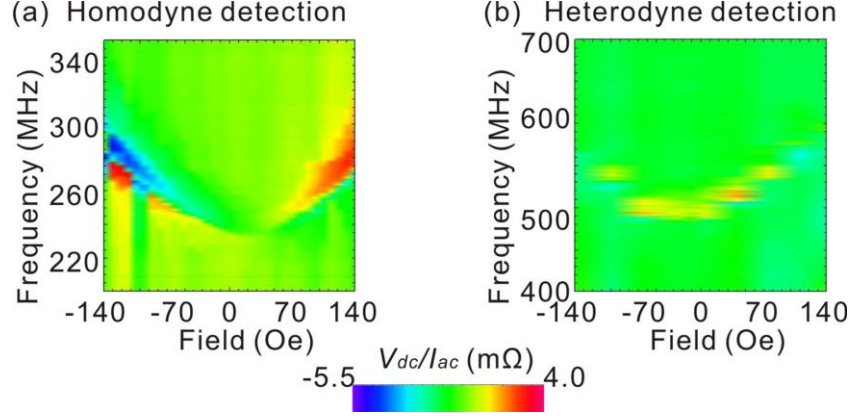

FIG. 4.6: In-plane static field dependences of resonant spectra obtained by (a) homodyne detection method and (b) heterodyne detection methods. Measurement conditions are same with Fig. 4.4.

magnetic field except for small shift due to sample asymmetry $(x_0, y_0) \neq (x_R, y_R)$. The frequency property of Fig. 4.6 (a) and (b) are comparable each other except for the base frequency at the zero magnetic filed $H_s = 0$ is doubled for heterodyne detection. On the contrary, the field dependences of (i) amplitudes of rectified voltage V_{dc}/I_{ac} and (ii) shapes of resonant spectra are totally different depending on the detection method, the former is shown in Fig. 4.7 and the latter in Fig. 4.8.

Note that Thiele's equation with static field H_s is difficult to be solved analytically due to the existence of time independent term. In a previous report, Buchanan *et al*[118] propose re-estimation of effective coefficient of parabolic potential κ by taking account of the additional Zeeman energy and founded out κ under the external field is reproducible by calculating the exchange energy and the demagnetization energy in conditions of shifted vortex core position by the applied field, as far as the vortex core confined in a ferromagnet. We here omit the quantitative estimation of our results but they are well comparable with the report of Buchanan *et al*.

Figure 4.7 shows field dependences of signal amplitudes at resonance (peak to dip amplitude $\Delta V_{dc}/I_{ac} \equiv \left| \frac{V_{dc,max}(f)}{I_{ac}} - \frac{V_{dc,min}(f)}{I_{ac}} \right|$). Results of homodyne detection (Fig. 4.7 (a)) linearly increase with field ($\Delta V_{dc}/I_{ac} \cong 5.0$ mΩ at maximum) while those of heterodyne detection keeps almost constant value ($\Delta V_{dc}/I_{ac} \cong 1.5$ mΩ) in this region. These results indicating 1st order AMR oscillation increases with distance of the core shift from the disk center $(y_0(H_s) - y_R)$ whereas rectifying dc voltage of heterodyne detection is independent from $x_0(x_R)$ and $y_0(y_R)$. As analytically predicted in Eq. 2.31, the shift distance $y_0(H_s) = -(cq/\kappa)H_s$ is also proportional to external field H_s, thus increase of resonant signal amplitude of homodyne detection $\Delta V_{dc}/I_{ac}$ is expected to show linear response to applied field, as confirmed in Fig 4.7. (a).

To focus on physics at equilibrium position $(y_0(H_{s0}) - y_R = 0)$, field dependences of resonant spectra around lowest point on curves in Fig.4.6 are plotted in Fig. 4.8. Note that the external field is
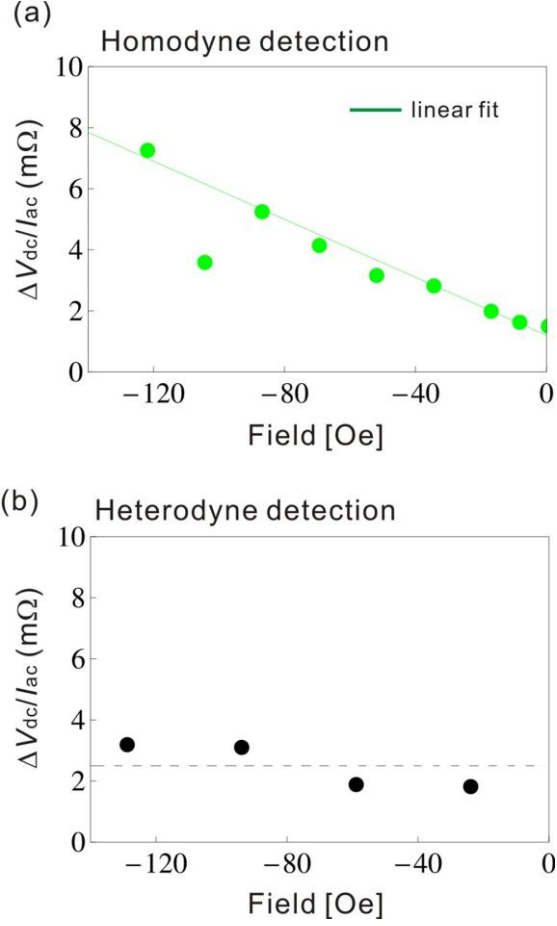
FIG. 4.7: In-plane static field dependences of peak to dip values of resonant spectra $\Delta V_{dc}/I_{ac}$ obtained by (a) homodyne detection method and (b) heterodyne detection methods. The black dashed line in (a) indicates a guide line for constant $\Delta V_{dc}/I_{ac}$ and a green solid line in (a) shows the linear fitting result.

so small that it does not tune the effective potential curve in Fig. 4.8, different from Fig.4.6. The values of H_{s0} are read out from Fig. 4.6 as $H_{s0} = 44$ Oe for homodyne detection (Fig. 4.8 (a)) and $H_{s0} = -11$ Oe for heterodyne detection (Fig. 4.8 (b)). The spectrum shape notably changes from +15 Oe to -15 Oe for homodyne detection: spectrum forms dip and peak structure at +15 Oe, once signal disappears at ± 0 Oe, and appears again -15 Oe but spectrum forms peak and dip structure opposite to result at +15 Oe. These results are well explained using Eq. 4.3. The core locates the very center of the disk $(x_0, y_0) = (x_R, y_R)$ at 0 Oe thus signal of rectifying voltage disappear. Around equilibrium position, sing of $(y_0(H_s) - y_R)$ switched from positive to negative, and spectra of $(y_0(H_s) - y_R)Y'$ also changes from peak and dip to dip and peak, causing changes in spectrum in Fig, 4.8 (a). Different from homodyne detection, both sign of rectifying voltage and signal amplitude keep constant around equilibrium position as can been seen in Fig. 4.8 (b), as predicted by Eq. 4.4. In other words, heterodyne detection method can be adoptable to detect non-distorted nature of harmonically oscillating core dynamics $((y_0(H_s) - y_R) = 0$, here), and also the rectifying voltage depends on the

squares of core position and thus the shape of spectra is more sensitive to the directionality of excitation torques, which allows us to discuss details of current induced torques onto vortex dynamics such as adiabatic spin torque, current induced Oersted field, and nonadiabatic spin torque, especially latter twos are under big debate.
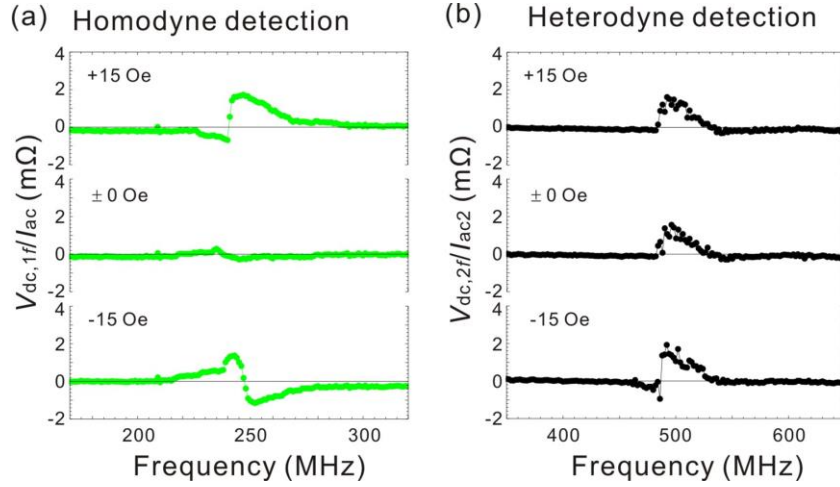

FIG. 4.8: Resonant spectra at form +15 Oe, -15 Oe shifted from the field H_{s0}, where the core locates the very center of the disk: $(y_0(H_{s0}) - y_R) = 0$. The values of H_{s0} are read out from Fig. 4.6 as $H_{s0} = 44$ Oe for homodyne detection (a) and $H_{s0} = -11$ Oe for heterodyne detection (b).

Estimation of physical quantity

From experimental results of homodyne and heterodyne detection of the translational mode, physical quantities concerned about vortex dynamics are determined. Obtained results are listed in Table B. The distance from the equilibrium position $(x_0 - x_R, y_0 - y_R)$ is first read out from field dependence in Fig. 4.6. Estimated values change from homodyne detection to heterodyne detection due to differences in sample design. Inevitable sample defects by attached electrode may result in larger $y_0 - y_R$ along current direction than $x_0 - x_R$. After determining $(x_0 - x_R, y_0 - y_R)$ and excitation current I_{ac}, other fitting parameters are obtained from Fig. 4.4 using Eq.4.3 and 4.4, i.e. Gilbert damping constant α, Coefficient of parabolic potential (κ_x, κ_y), Proportionality constant a, and contribution of current induced Oersted field $G_0 u_0 / qH$.

The analytical prediction of coefficients of parabolic potential (κ_x, κ_y) nicely agrees with measurement results. Therefore the energy of vortex structure is dominantly described by means of demagnetization energy and exchange energy on assumption of the vortex core as a rigid quasiparticle. This result also indicates relaxation of side magnetic charges is not crucial since analytical prediction in Sec. 2.6 assumes circular rotation of in-plane magnetization does not change by core shift. Apart from estimation of the vortex energy, the excitation ratio of spin torque and field is evaluated as $G_0 u_0 : qH = 5 : 2$, estimated from tailing of spectrum in Fig. 4.4 (a). The dominancy of spin torque is

not necessarily coincide with other reports of dc[65] or ac current[70,76] induced core dynamics while shows consistency with where uniform current injection selectively excites coupled modes reflecting combinations of chiralities in Sec. 5.2.3. It is worth mentioning current flowing in real ferromagnet is not necessarily uniform and possibly changes depending on sample geometry, even though having the same magnetic configuration, i.e. vortex structure.

These parameters are shared also for the going studies in chapter 5 and 6 of coupled systems since we use same fabrication scheme.

Physical quantity	Symbol	Value
Excitation current	I_{ac}	1.6×10^{-3} A
Polarization*	P	0.4
Saturation magnetization*	M_S	8.6×10^5 A/m
Gyromagnetic ratio*	γ	1.76×10^{11} s^{-1}T^{-1}
Radius of the disk	R	5.0×10^{-7} m
Thickness	L	3.0×10^{-8} m
Vortex core radius	R_C	1.0×10^{-8} m
Gilbert damping constant	α	0.016
Nonadiabatic spin torque*	β	0.14
Coefficient of parabolic potential (fitting)	(κ_x, κ_y)	$(1.3 \times 10^{-3}$ J/m^2, 1.3×10^{-3} J/m$^2)$
Coefficient of parabolic potential (analytical)	(κ_x, κ_y)	$(1.3 \times 10^{-3}$ J/m^2, 1.3×10^{-3} J/m$^2)$
Distance from the disk center (homodyne detection)	$(x_0 - x_R, y_0 - y_R)$	$(4.2 \times 10^{-8}$ m, 8.5×10^{-8} m,$)$
Distance from the disk center (heterodyne detection)	$(x_0 - x_R, y_0 - y_R)$	$(9.5 \times 10^{-9}$ m, 5.0×10^{-8} m$)$
Proportionality constant	a	5.2×10^{10} Ω/m^2

Table B: A list of the physical quantity set estimated from resonant spectra.

* Literature data

4.2.3. Micromagnetic simulation

Micromagnetic calculation of ac current-induced dynamics of the vortex with same sample dimension is parallely performed to obtained insights of time evolution of core dynamics. Figure 4.9 (a) shows excitation frequency dependence of radius of the core trajectory $|X'|$ at 50 ns after start of excitation. The core is resonantly excited at 245 MHz and forms symmetric peak structure in spectrum. Note that the value of resonant frequency well coincides with experimental results in Fig. 4.4, 238 MHz, showing rigid quasiparticle approximation with solid in-plane magnetization in analytical description and experimental fitting is quantitatively comparable with the sentence of micromagnetic modelling, where the variational method about total energy is performed. Time evolutions of core dynamics are plotted in Fig. 4.9 (b) and (c), the core trajectory in real space and core position as a function of time. One may wonder the core trajectory is distorted from complete circular rotation to slightly tilted elliptical form. The elliptical shape of trajectory is caused by linear excitation, the core is not uniformly applied rotational torque but driven by stronger torque along current direction. Apart from
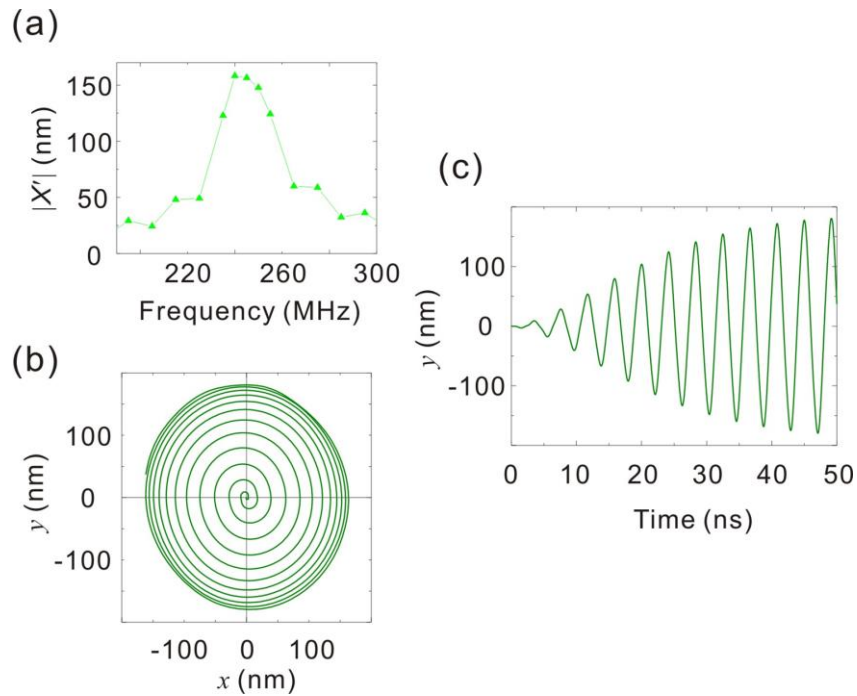

FIG. 4.9: Micromagnetic simulation results of (a) the excitation amplitude along x-axis $|X'|$ as a function of injected current frequency, (b) a resonantly excited core trajectory at 240 MHz from 0 to 50 ns after the start of excitation, (c) the time evolution of core position y.

linear excitation, small tilting from current direction is caused by the Oersted field. The phase of this ac field is differing $\pm\pi/2$ depending on chirality c. Time to reach steady precession in simulation is estimated to around 30 - 40 ns here and strongly affected damping parameter.

4.3. Study of magneto-optical detection of damping process of the vortex core

4.3.1. Measurement set up and device structure

Measurements in frequency space demonstrated in Sec. 4.1 and 4.2 enable to discuss details of the vortex dynamics. Besides, the energy dissipation process, i.e. a damping process of the vortex core from a deflected position to the equilibrium position is next discussed via time-resolved MOKE measurement introduced in Sec. 3.2.2.

Top view of measurement devices is shown in Fig. 4.10 (a). Ferromagnetic disks where magnetic vortices are confined were deposited onto a microwave stripline and core dynamics have been investigated using a magnetic field pulse excitation method. Note that radii of MOKE measurement samples are set to be larger than those of frequency measurement sample, owing to the sensitivity and the space resolution of our magnetometer ($2\sim3$ μm). All measurement results in this thesis were obtained from samples with $(R, L) = (1500 \text{ nm}, 50 \text{ nm})$ and its eigenfrequency remarkably decreases from samples with $(R, L) = (500 \text{ nm}, 30 \text{ nm})$ of frequency domain measurements, due to the smaller demagnetization energy[77]. It is worth mentioning we here have not directly detected core dynamics via the polar Kerr effect but in-plane magnetization component via the longitudinal Kerr effect (see Fig. 4.10 (b)). Remanent states of samples were checked by observations of hysteresis
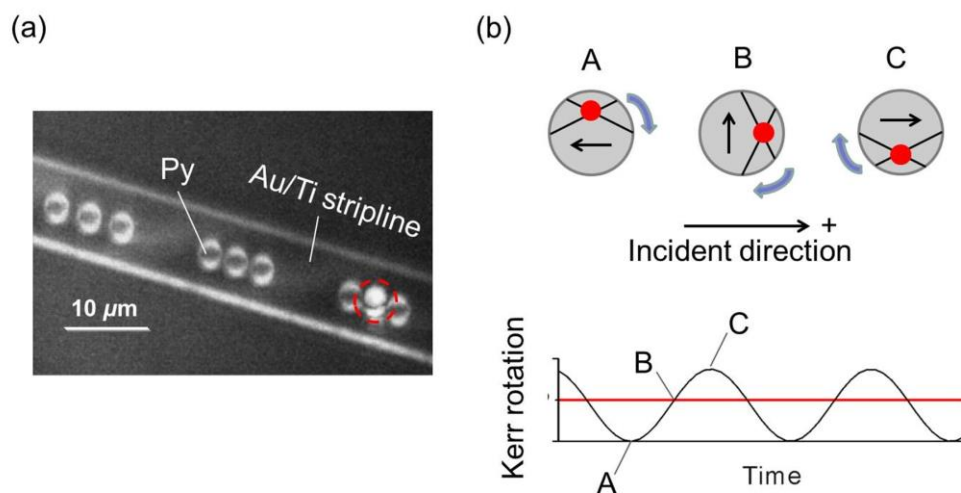

FIG. 4.10: (a) Top view of sample obtained by CCD camera. A microwave stripline is used for excitation circuit. A spot of probe light is marked by a red circle. (b) Schematic illustrations of a relation of core position and MOKE signal.

loops same with methods of frequency sensor.

4.3.2. Time resolved measurement of the damping process of the core

Figure 4.11 shows time-resolved Kerr rotation at a damping process obtained from the magnetic vortex. A clear sinusoidal oscillation is observed as a function of time, and the oscillation amplitude is
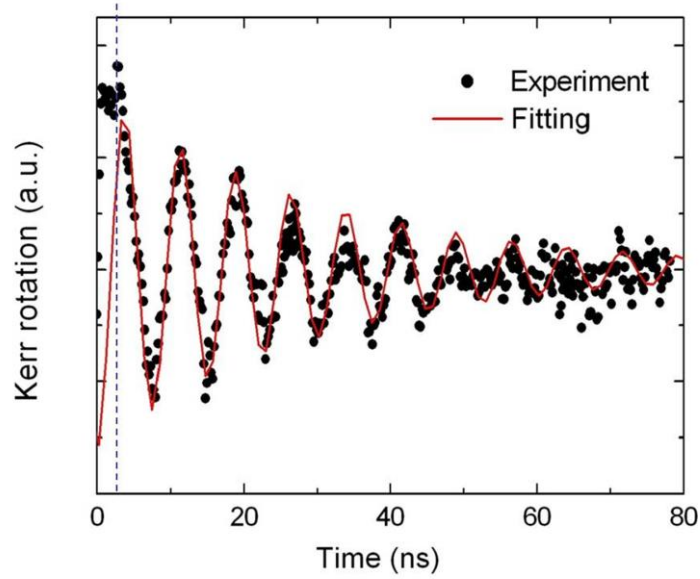

FIG. 4.11: Time-resolved Kerr rotation from a permalloy circular disk. The excitation field pulse is removed at 2.3 ns (blue dashed line). Red curve shows fitting results with Eq.4.5. The excitation amplitude of field pulse is estimated 55 ± 7 Oe.

exponentially decayed with time as predicted in Eq. 2.36. The time evolution of Kerr rotation V in Fig. 4.11 can be fitted using

$$V = A_0 \cos \omega_\gamma t \cdot e^{-\Gamma t}, \tag{4.5}$$

with $\frac{\omega_\gamma}{2\pi} = 132.6$ MHz and $\Gamma = 2\pi \times 5.1$ MHz. Both obtained values of the eigenfrequency ω_γ and the damping parameter Γ are quantitatively comparable with analytical prediction. This result can be regarded as criteria of two coupled vortices discussed in Sec 5.3.

5. Magnetic diatomic molecules of magnetostatically coupled vortices

This chapter deal with the main topic of this thesis, studies of coupled two vortices via the magnetic dipolar interaction as the unit of vortex-used magnonic crystal. In Sec. 5.1, we first introduce the theoretical discussion of magnetostatically coupled vortices by starting from Thiele's equation. In Sec. 5.2, experimental demonstration of current-induced coupled dynamics is discussed using frequency sensor developed in Sec. 4.2. We study several different geometries and discuss analogies with homonuclear diatomic molecules. In addition to frequency properties of coupled vortices, energy dissipation process is discussed via time resolved- MOKE measurement in final Sec. 5.3.

5.1. Analytical description of magnetic dipolar coupling of different vortices

Theoretical model

As briefly introduced in Sec. 2.7, the large core shift from the equilibrium position causes side magnetic charges strong enough to affect a neighboring magnetic vortex confined in separate ferromagnet. Studied of single magnetic vortex in chapter 4 reveals the vortex core can be approximated as a rigid quasiparticle and emergence of side magnetic charges is assured by discussion of magnetostatic energy. To obtain insights of dynamics of coupled vortices, theoretical description of magnetostatically coupled vortices introduced by Shibata *et al.*[21,22] was first introduced.

Calculation system is composed of two neighboring ferromagnetic disks 1 and 2 confining a magnetic vortex for each, with center to center distance $D = dR$. These two disks align parallel to *x*-axis. The stray field $\boldsymbol{H}_{int}$ of a neighboring structure leads to an additional Zeeman energy term U_{int} onto the parabolic potential U_{tot} in Thiele equation (Eq. 2.29). The interaction energy U_{int} between the two disks can be calculated in the same manner with the demagnetization energy. Magnetization here is assumed to be uniform toward thickness direction (normalized thickness $g \equiv L/R \ll 1$) and circularly carling magnetization as we adopted in rigid vortex mode. Using the trigonometric identities, magnetic side surface charge density $\sigma(\varphi_i)$ is described as functions of each core position $\boldsymbol{r}_i = (x_i, y_i) = \rho_i(\varphi_i)$, in Cartesian and polar coordinate, respectively.

$$\sigma(\varphi_i) = -\frac{c_i}{R} \frac{x_i \sin \varphi_i - y_i \cos \varphi_i}{\sqrt{1 + \frac{|r_i|^2}{R^2} - \frac{2}{R}(x_i \cos \varphi_i + y_i \sin \varphi_i)}}, \qquad (5.1)$$

Where c_i is the chirality of i-th core. Therefore, the additional interaction energy U_{int} is calculated as

$$U_{int} = \frac{\mu_0 M_S^2}{8\pi} \int dS_1 \int dS_2 \frac{\sigma(\varphi_1)\sigma(\varphi_2)}{|r_1 - r_2|} \equiv \frac{c_1 c_2}{R^2}\left(\eta_x x_1 x_2 - \eta_y y_1 y_2\right) + O\left(\frac{|r|^3}{R^3}\right). \tag{5.2}$$

Values of (η_x, η_y) can be expressed as below.

$$\eta_x = \frac{\mu_0 M_S^2 R^3}{8\pi} \int dS_1 dS_2 \tag{5.3}$$

$$\cdot \frac{\sin\varphi_1 \sin\varphi_2}{\sqrt{d^2 + 2d(\cos\phi_2 - \cos\phi_1) + 2 - 2\cos(\phi_2 - \phi_1) + (z_2 - z_1)^2}}$$

$$\eta_y = -\frac{\mu_0 M_S^2 R^3}{8\pi} \int dS_1 dS_2$$

$$\cdot \frac{\cos\varphi_1 \cos\varphi_2}{\sqrt{d^2 + 2d(\cos\phi_2 - \cos\phi_1) + 2 - 2\cos(\phi_2 - \phi_1) + (z_2 - z_1)^2}}$$

Here, integration of side surfaces is written as $\int dS_1 dS_2 = \int_0^{L/R} dz_1 \int_0^{L/R} dz_2 \int_0^{2\pi} d\phi_1 \int_0^{2\pi} d\phi_1$.

The coefficient (η_x, η_y) is function of normalized separation distance d and has the unit of energy (J). It is worth mentioning (η_x, η_y), called as coupling integral in this thesis, is independent form polarities and chiralities of vortices (p_i, c_i) but only depends on sample design.

Fig.5.1 shows normalized center to center distance $(d = D/R)$ dependence of coupling integral (η_x, η_y) for a pair of disks calculated from Eq. 5.3. In accordance with the simulations in Fig. 2.13
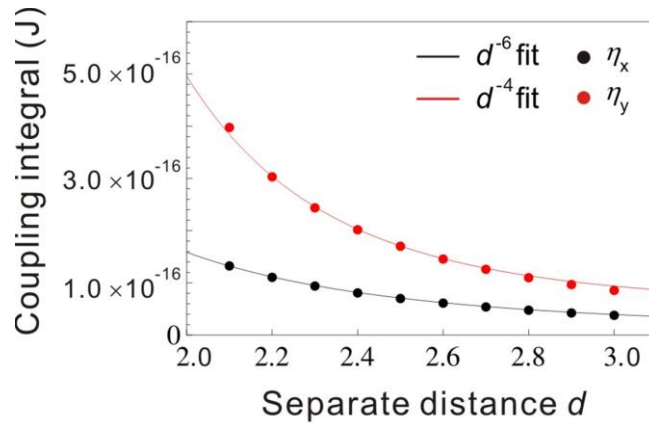
FIG. 5.1: Normalized center to center distance dependence of the coupling integral (η_x, η_y). Fitting results by d^{-4} and d^{-6} are plotted by solid curves.

and 2.14, the amplitude of the stray field is larger for a core displacement perpendicular to the coupling direction (x axis). The value of η_y always exceeds the value of η_x, showing the stray field at a core shift in y direction dominates the magnetostatic interaction. The values of the coupling integrals (η_x, η_y) decrease with increasing normalized center to center distance d. From 500 nm to

240 nm in edge to edge distance ($2.0 \leq d \leq 3.0$), the value of η_y takes almost two times larger than that of η_x whereas both coupling integrals drastically increase with decrease of separate distance. For the given dimensions of the disks, the variation of η_x and η_y with the distance can be determined via fitting with a power law as $\eta_x \propto d^{-4}$ and $\eta_y \propto d^{-6}$ within the region of interest. One can notice the inverse sixth power dependence of the dominating coupling integral η_y also is a prominent feature of the interaction between induced dipoles, and shows analogy with van der Walls force in real molecules. In addition, obtained coupling energy U_{int} becomes comparable with parabolic potential U at around 240 nm and the core dynamics can be surely affected in this region.

Revised Thiele equation

Note that U_{int} is derived by means of second order Taylor expansion for $\frac{|r|}{R}$, and it effectively acts as

an elastic force $\boldsymbol{F}_{int} = -\frac{\partial U_{int}}{\partial \boldsymbol{r}} \propto -\begin{pmatrix} x_i \\ y_i \end{pmatrix}$ in Thiele's equation. It allows us to analytically resolve

revised Thiele equation with an assumption of current synchronized oscillating cores ($(x_i, y_i) = \left(x_{0i} + \mathrm{Re}\{X_i e^{i\omega t}\}, y_{0i} + \mathrm{Re}\{Y_i e^{i\omega t}\}\right)$ with $(X_i, Y_i) = \left(X'_i + iX''_i, p(Y'_i + iY''_i)\right)$). The calculated eigenfrequencies are expressed as

$$(5.4)$$

$$\omega_{\gamma, p_1 p_2} = \omega_\gamma \sqrt{(1 + p_1 p_2 \lambda_x)(1 - \lambda_y) - \tilde{\alpha}^2 \left(\frac{p_1 p_2 \lambda_x + \lambda_y}{2}\right)^2}$$

$$\omega_{\gamma, p_1 p_2}{}^* = \omega_\gamma \sqrt{(1 - p_1 p_2 \lambda_x)(1 + \lambda_y) - \tilde{\alpha}^2 \left(\frac{p_1 p_2 \lambda_x + \lambda_y}{2}\right)^2}$$

with $\lambda_i \equiv \eta_i / \check{\kappa}$ ($i = x, y$). Following discussion in Sec. 2.6, polarity depending gyrovector $\boldsymbol{G}(p)$ switches the symmetry of stray field distribution and total interaction energy changes. Coupled modes with eigenfrequencies $\omega_{\gamma, p_1 p_2}{}^*$ keeps higher energy states $\left(\omega_{\gamma, p_1 p_2} < \omega_\gamma < \omega_{\gamma, p_1 p_2}{}^*\right)$ as antibonding modes, and opposite polarities $p_1 p_2 = -1$ results a larger frequency shift from the single eigenfrequency than parallel polarities $p_1 p_2 = 1$ $\left(|\omega_{\gamma, +1}{}^{(*)} - \omega_\gamma| < |\omega_{\gamma, -1}{}^{(*)} - \omega_\gamma|\right)$. That is, two coupled vortices can possess two bonding and antibonding type eigenstates for given polarities $p_1 p_2 = \pm 1$, therefore totally 4 discrete eigenstates are given. This discrete energy scheme can be understood by considering spatial symmetry of stray field. Figure 5.1 indicates there exist clear directionality in coupling energy associated with core gyration, and interaction energy is different when two cores are shifted parallel to coupling direction or not. Details of core dynamics and interaction energy are studied in Sec. 5.2, and summarized in Sec. 5.2.4. Note that the original eigenfrequency of the magnetic vortex is independent from polarity and chirality (p, c) while the two coupled vortices have 4 different eigenstates, and those can be tuned by changing polarities $p_1 p_2$.

The complex core amplitudes $(X_i, Y_i) = \left(X'_i + iX''_i, p(Y'_i + iY''_i)\right)$ can be obtained from revised Thiele equation in the same manner with the single vortex in Eq. 2.30 to Eq. 2.35. The general form of (X_i, Y_i) is written as

$$\begin{pmatrix} X_1 \\ Y_1 \\ X_2 e^{i(\Delta\varphi+\Delta\Phi)} \\ Y_2 e^{i(\Delta\varphi+\Delta\Phi)} \end{pmatrix} = \begin{pmatrix} -p_1 G_0 u_1 \\ \beta D u_1 - c_1 q H_1 \\ -p_2 G_0 u_2 e^{i\Delta\varphi} \\ \beta D u_2 e^{i\Delta\varphi} - c_2 q H_2 e^{i\Delta\varphi} \end{pmatrix}$$

$$\cdot \begin{pmatrix} \kappa_x + i\alpha\omega D & -i\omega p_1 G_0 & \dfrac{c_1 c_2 \eta_x}{R^2} & 0 \\ i\omega p_1 G_0 & \kappa_y + i\alpha\omega D & 0 & \dfrac{-c_1 c_2 \eta_y}{R^2} \\ \dfrac{c_1 c_2 \eta_x}{R^2} & 0 & \kappa_x + i\alpha\omega D & -i\omega p_2 G_0 \\ 0 & \dfrac{-c_1 c_2 \eta_y}{R^2} & i\omega p_2 G_0 & \kappa_y + i\alpha\omega D \end{pmatrix}^{-1} .$$

Note that two additional parameters are introduced, the phase difference of current in disk 1 and 2 $(\Delta\varphi)$ and the phase difference of core gyrations $(\Delta\Phi)$.

5.2. Frequency domain measurements

5.2.1. Device structure & measurement set up

Figure 5.2 shows the measurement circuit diagram of two coupled system. We adopt the homodyne
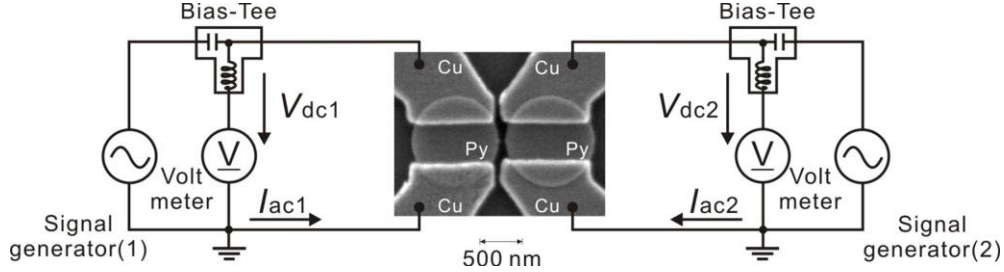

FIG. 5.2: The measurement circuit diagram of two coupled vortices and a SEM of a sample. The circuit includes 2 rf sources (Signal generator (1) & Signal generator (2)) and they are monitored using same manner with the heterodyne detection in Fig. 4.2 (b). The amplitude of I_{ac2} is varied for different excitation methods: $I_{ac2} = 0$ for local excitation (Sec. 5.2.2), $I_{ac2} = I_{ac1}$ for global excitation (Sec. 5.2.3), $I_{ac2} = I_{ac1}e^{i\Delta\varphi}$ for phase detection (Sec. 5.2.4) and free excitation (Sec.

detection method basis of detection scheme is same with homodyne detection in chapter 4. Spacially and electrically separated two ferromagnetic circular disk with vortex structures are neighbored with the center to center distance $D \equiv dR$, and each disk is connected to CWG in order to detect rectified dc voltage via 1st order harmonic AMR oscillation. The phase difference of ac current injected each disks $\Delta\varphi$ is monitored by the same manner with study of 2nd order harmonic AMR oscillation using heterodyne detection.

In this section, four different set up are demonstrated, as illustrated in Fig. 5.3. Note that the spatial symmetry of two coupled system shall be decide only three parameters, polarities p_1p_2, chiralities c_1c_2, and the phase difference of core gyrations $\Delta\Phi$. First, we introduce the local excitation (Fig.5.3 (a)) method. In this method, only the left vortex 1 is excited by ac current I_{ac1} and the right vortex 2 is purely driven through magnetic dipolar interaction. There is no limitation in the phase difference of core gyrations $\Delta\Phi$, and only the information of polarities p_1p_2 can appear in the spectra in this method in this manner.

In the second method, global excitation (Fig.5.3 (b)) is demonstrated, two identical current flows in vortex 1 and 2 i.e. $I_{ac2} = I_{ac1}$ with $\Delta\varphi = 0$. With an assumption that the phase difference of excitation current $\Delta\varphi$ decides the synchronized core rotation phase $\Delta\Phi$, the information of chiralities c_1c_2 directly affects the energetic stability of coupled modes and decides whether excitation of bonding modes ω_{γ,p_1p_2} or antibonding mode $\omega_{\gamma,p_1p_2}{}^*$. Thus we can extract information of both polarities and chiralities (p_1p_2, c_1c_2).

In the third set up, phase detection requires, we additionally applied a weak detection current I_{ac2} on the right vortex 2 with conditions of $I_{ac2} \ll I_{ac1}$ so as not to excite any core dynamics by a detection current I_{ac2} (Fig.5.3 (c)) but to read out the phase information of core precessions in sign of rectified voltage. The phase difference of core gyration $\Delta\Phi$ can appear in the second right spectra and configurations of $(p_1p_2, c_1c_2, \Delta\Phi)$ can be discussed experimentally.

Finally we introduce the free excitation method (Fig.5.3 (d)). The same amplitude of two currents $|I_{ac2}| = |I_{ac1}|$ with keeping finite phase difference $\Delta\varphi$ excites two vortices respectively. In this alignment, and we can coordinate all geometrical parameters of coupled mode $(p_1p_2, c_1c_2, \Delta\Phi)$ and
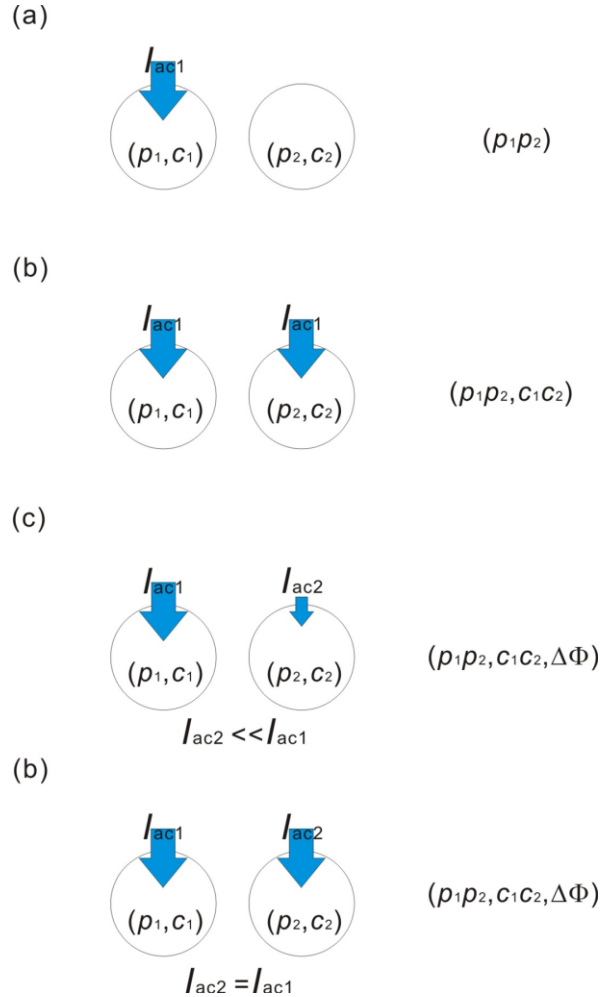

FIG. 5.3: Schematic images of measurement set up for (a) local excitation, (b) global excitation, (c) phase detection, and (d) free excitation.

selective excitation of four different states by changing $(p_1p_2, c_1c_2, \Delta\Phi)$ can be expected. All these four alignment, sample dimension: radius of disks, thickness and center to center distance are fixed as $(R, L, D) = (500 \text{ nm}, 30 \text{ nm}, 100 \text{ nm})$ here. More quantitative discussions and analogies with diatomic molecules are discussed in Sec. 5.2.6.

5.2.2. Local excitation

The resonant spectra of two neighboring magnetic vortices detected via local excitation are shown in Fig. 5.4 (b) as a function of the frequency of injected ac current I_{ac1}. For comparison, a spectrum of
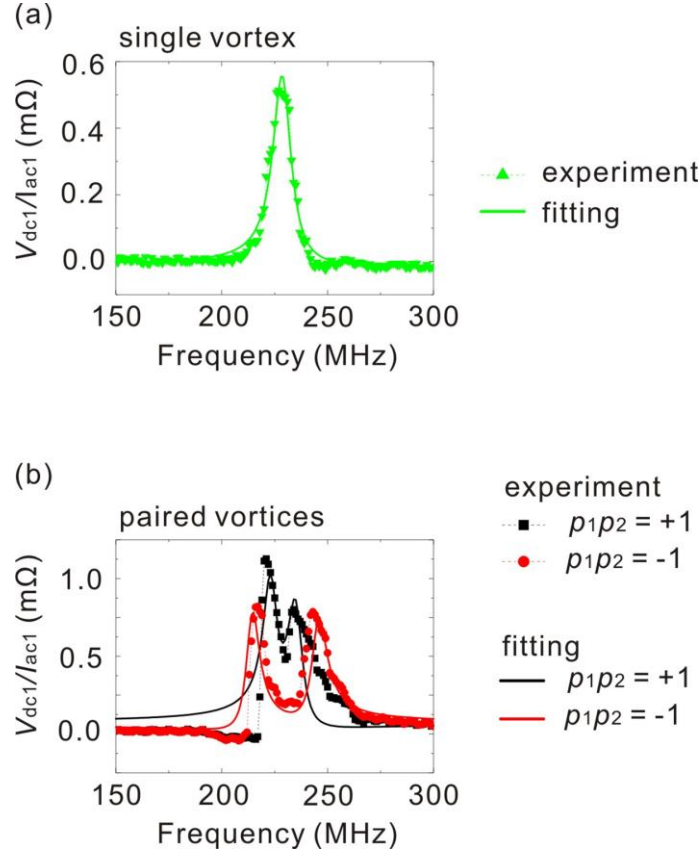

FIG. 5.4: Resonant spectra of (a) single vortex (b) two coupled vortices by means of local excitation (vortex 1). Results for $p_1 p_2 = -1$ and $p_1 p_2 = +1$ are plotted by red and black symbols, respectively. The excitation current is set to be $I_{ac1} = 2.5$ mA for both (a) and (b). Solid lines are fitting curves calculated by substituting Eq. 5.5 into Eq. 4.3.

single magnetic vortex is plotted in Fig. 5.4 (a). The eigenfrequency ω_γ observed through 1st order harmonic AMR oscillation clearly spits into two branches, higher frequency $\omega_{\gamma,p_1 p_2}{}^*$ and lower frequency $\omega_{\gamma,p_1 p_2}$ with respect to the original eigenfrequency. The former can be antibonding modes and the latter corresponds to bonding modes. The splitting amplitude is only depends on polarities $p_1 p_2$: a larger splitting amplitude more than 20 MHz for antiparallel polarities $p_1 p_2 = -1$ (red symbols in Fig. 5.4 (b)) and a smaller spitting amplitudes around 15 MHz for parallel polarities $p_1 p_2 = +1$ (black symbols in Fig. 5.4 (b)) are observed. Therefore, totally 4 different eigenfrequencies are observed for two neighboring vortices, as precisely predicted by analytical calculation in Eq. 5.4. Apart from these frequency properties, the amplitude of rectifying voltage $|V_{dc1}/I_{ac1}|$ also changes depending on the each state. Signal amplitude becomes generally larger for two neighboring vortices than single vortex $|V_{dc1}/I_{ac1}|_{single} \sim 0.58$ mΩ $< |V_{dc1}/I_{ac1}|_{couple}$. In

addition, the amplitude of bonding modes becomes larger than that of antibonding mode $|V_{dc1}/I_{ac1}||_{p_1 p_2 = +1} \sim 1.3$ mΩ $> |V_{dc1}/I_{ac1}|^*_{p_1 p_2 = +1} \sim 0.83$ mΩ.

Frequency splits in Fig. 5.4 are originated from neither neighboring effect nor the nonlinear effect[119,120]. Excitation current I_{ac1} dependences of resonant spectra of single vortex and two neighboring vortices are shown Fig. 5.5. Within the region of measurements 1.3 mA $\leq I_{ac1} \leq 2.8$ mA, the resonance line of single vortex in Fig. 5.5 (a) keeps a constant eigenfrequency at 230 MHz with a constant bandwidth. The results shows the core dynamics surely belong to the linear region where parabolic form of potential approximation in Thiele equation is effective. Spectra of two neighboring vortices also keep constant splitting amplitude for both configurations of polarities $p_1 p_2 = \pm 1$, except for small broadening above 2.5 mA for $p_1 p_2 = +1$. Hereby frequency splitting in Fig. 5.4 and Fig. 5.5 can be explained as a unique effect in two neighboring vortices.
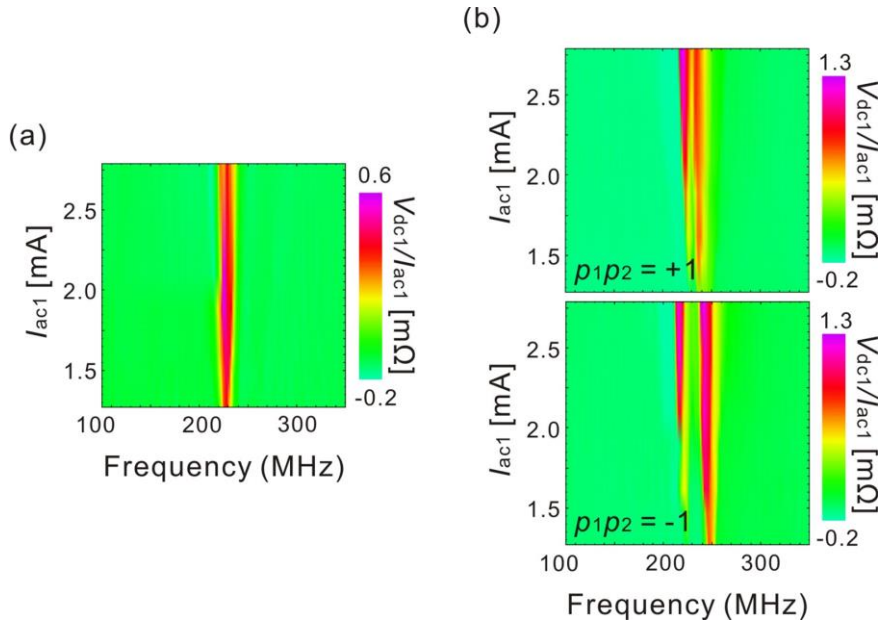

FIG. 5.5: Excitation amplitude dependences of resonant spectra of (a) single vortex and (b) two coupled vortices by means of local excitation.

Experimental results are reproduced our micromagnetic simulation and it also gives practical insights of actual core dynamics obtained by local excitation method. Frequency properties of excitation amplitude are summarized in Fig. 5.6. Simulated results can be directly comparable with resonant spectra of Fig. 5.4, except for small tailing in experimental spectra. The unique eigenfrequency of single vortex splits into higher antibonding states and lower bonding states just like experimental results. Chirality dependencies are also examined in simulation in Fig. 5.7 (b) and chirality configuration $c_1 c_2$ itself does not affect the excitation amplitude. In addition difference of excitation amplitude at each resonant condition is also reproduced by simulations, except for the largest excitation amplitude of single vortex.
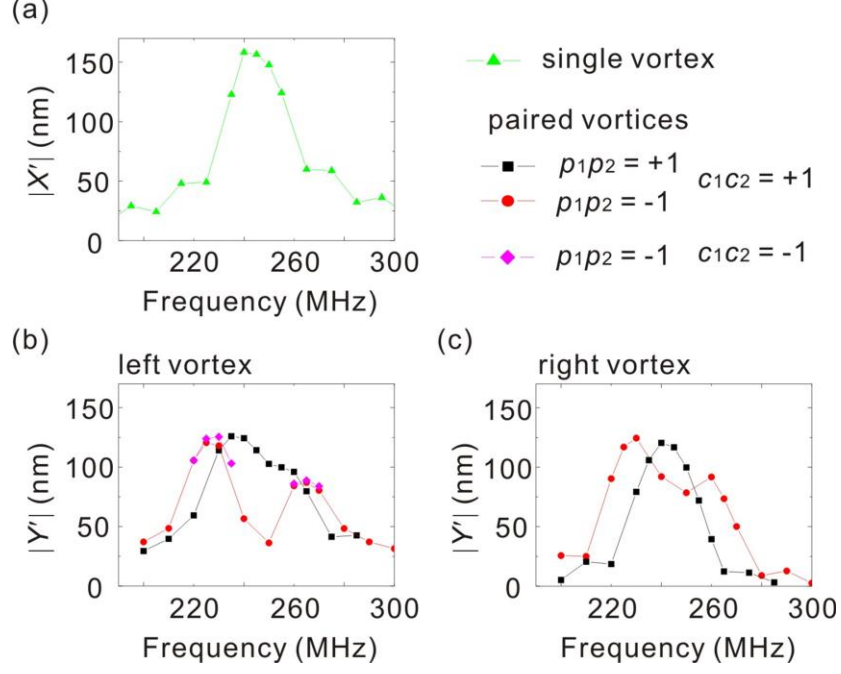
FIG. 5.6: Micromagnetic simulation results of the excitation amplitude along the current direction (a) for single magnetic vortex, (b) two neighboring vortices with $(p_1p_2, c_1c_2) = (-1, \pm 1)$ and (c) two vortices with $(p_1p_2, c_1c_2) = (+1, +1)$. Results of (b) and (c) are obtained by local excitation alignment.

Details of core dynamics at each resonant condition are shown in Fig. 5.7: the bonding mode with $p_1p_2 = -1$ ($\frac{\omega_{\gamma,-1}}{2\pi} = 225$ MHz) in Fig. 5.7 (a), the antibonding mode with $p_1p_2 = -1$ ($\frac{\omega_{\gamma,-1}^*}{2\pi} = 265$ MHz) in Fig. 5.7 (b), the bonding mode with $p_1p_2 = +1$ ($\frac{\omega_{\gamma,+1}}{2\pi} = 235$ MHz) in Fig. 5.7 (c), and the antibonding mode with $p_1p_2 = +1$ ($\frac{\omega_{\gamma,+1}^*}{2\pi} = 255$ MHz) in Fig. 5.7 (d). The time evolution of two cores of vortex 1 (blue lines) and vortex 2 (red lines) are plotted in the left sides of each figures. Simulation results directly shows two neighboring vortices coupled via magnetic dipolar interaction. After several decades nanoseconds from the start of excitation, the directly excited core 1 settles on steady precession, and the indirectly excited core 2 also starts gyration with about 10 ns retarded from core 2. Both two cores settle on steady precession at 40 to 50 ns from start, and excitation amplitude of core 2 is 20 % smaller than that of core1. Focusing on the phase difference between two cores, one can find out that two cores rotate with in-phase at bonding modes in Fig. 5.7 (a) and (c) while cores rotates with opposite phase at antibonding modes in Fig. 5.7 (b) and (d). Thus, the phase difference between two cores $\Delta\Phi$ determines the stability of two coupled vortices via magnetic dipolar interaction. Here stable bonding modes are written as $\Delta\Phi = 0$ and metastable antibonding mode are written as $\Delta\Phi = \pi$. Note that any intermediate modes with $0 < \Delta\Phi < \pi$ does not excited, thus eigenfrequencies

62

of two coupled vortices forms four distinctive states predicted in Eq. 5.4 $\omega_{\gamma,\pm 1}$ and $\omega_{\gamma,\pm 1}^{*}$. Apart from the phase difference of two cores, insights about excitation amplitude can be seen from core trajectories. Excitation amplitudes at antibonding modes are necessarily decrease from those at bonding mode since side magnetic charges act repulsively and energetically unstable. The distortion of core trajectory reflects on alignment of side magnetic charges: at bonding modes, side charges attracts each other that core trajectories somehow extended to coupling direction, and result in clear elliptical form different from trajectory of single vortex in Fig. 4.9 (b). On the contrary, repulsive side charges shrink core trajectories orthogonal to bonding at anti bonding mode. Such distorted core trajectories can be a reason that larger signal amplitude at two couple vortices rather than single vortex in Fig. 5.4, nevertheless simulated excitation amplitude itself becomes smaller (see Fig. 5.6). As treated in the chapter 4, homodyne detection method is originated from additional 1st order harmonic oscillation of AMR generated by symmetry breaking. Therefore enhanced anisotropy of elliptical trajectory at two coupled vortices surely increases the rectifying voltage of homodyne detection.

In these ways, collective particle like magnetization dynamics has been excited by means of local excitation at neighboring two circular disks. Analytically predicted four distinctive modes are written by the phase difference $\Delta\Phi$ and rotation direction, determined by $p_1 p_2$, of two cores.
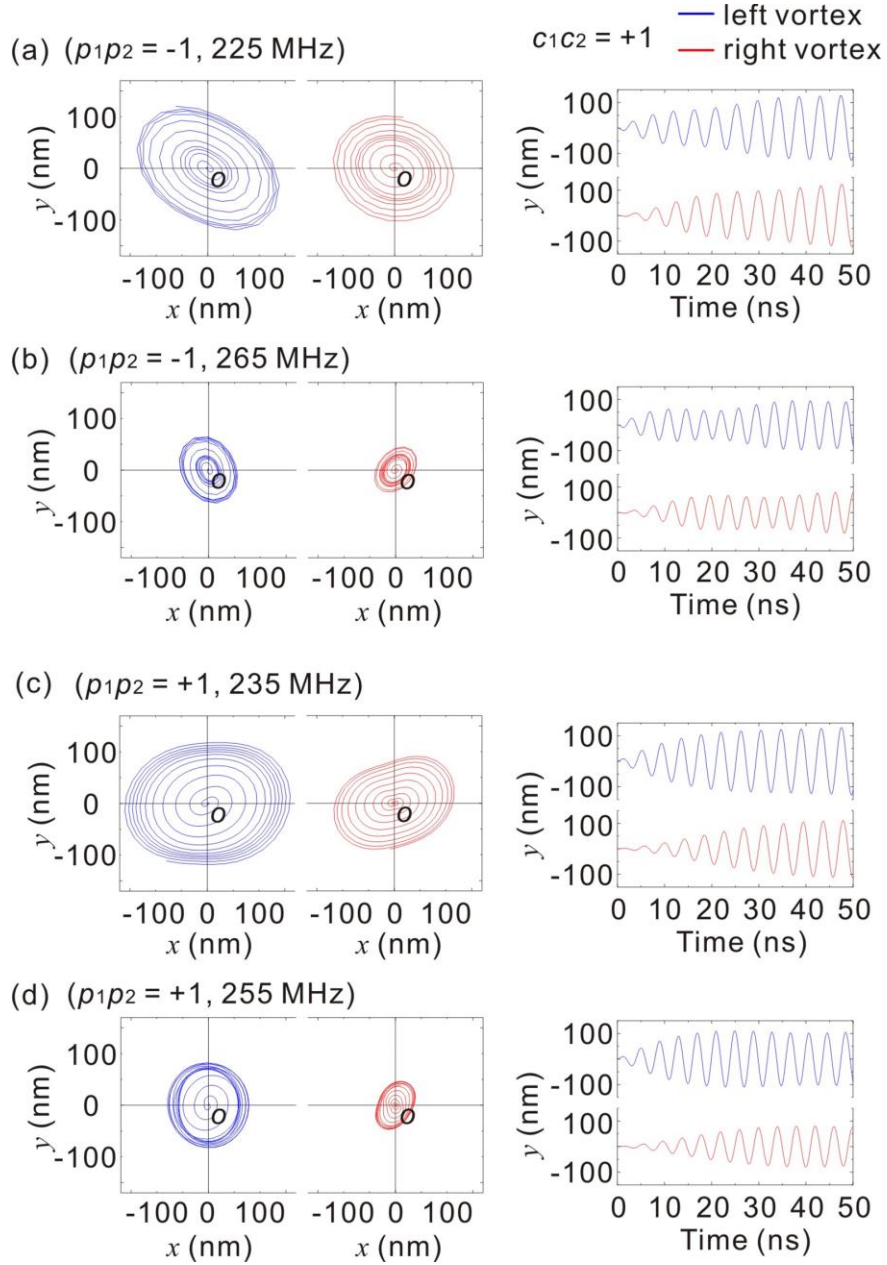
FIG. 5.7: Micromagnetic simulation results of time evolutions of vortex cores at resonant conditions: (a) 225 MHz for the bonding mode with $p_1 p_2 = -1$, (b) 265 MHz for the antibonding mode with $p_1 p_2 = -1$, (c) 235 MHz for the bonding mode with $p_1 p_2 = +1$, and (d) 255 MHz for the antibonding mode with $p_1 p_2 = +1$. Chiralities are fixed as $c_1 c_2 = +1$. All results are obtained by local excitation alignment.

5.2.3. Global excitation

Effect of chiralities is difficult to be observed experimentally in resonant spectra (see Fig. 5.4 and Fig. 5.6). As introduced in Sec. 2.7, chirality switch can be complimented by changing position of the core in stray field distribution. Thus the phase free local excitation is not convenient to discuss chiralities. Therefore, uniform excitation named as global excitation alignment is demonstrated. The current induced torque excites two cores at same phase thus chirality information can be seen in energetic stability, which the spin torque diode sensor can convert into resonant frequencies.

Figure 5.8 (a) shows resonant spectra obtained by means of global excitation, both the left and right cores here excited by same amplitude of current $I_{ac1} = 2.5$ mA. Different from local excitation, the ac current induced torque applied synchronously onto two vortices, there should be limitations on phase difference of cores. A clear sole resonant peak appears depending on the not only polarities $p_1 p_2$ but also chiralities $c_1 c_2$. Antibonding modes $\omega_{\gamma, p_1 p_2}{}^*$ are excited with opposite chiralities $c_1 c_2 = -1$ (open symbols in Fig. 5.8 (a)) whereas bonding modes $\omega_{\gamma, p_1 p_2}$ are observed with same chiralities
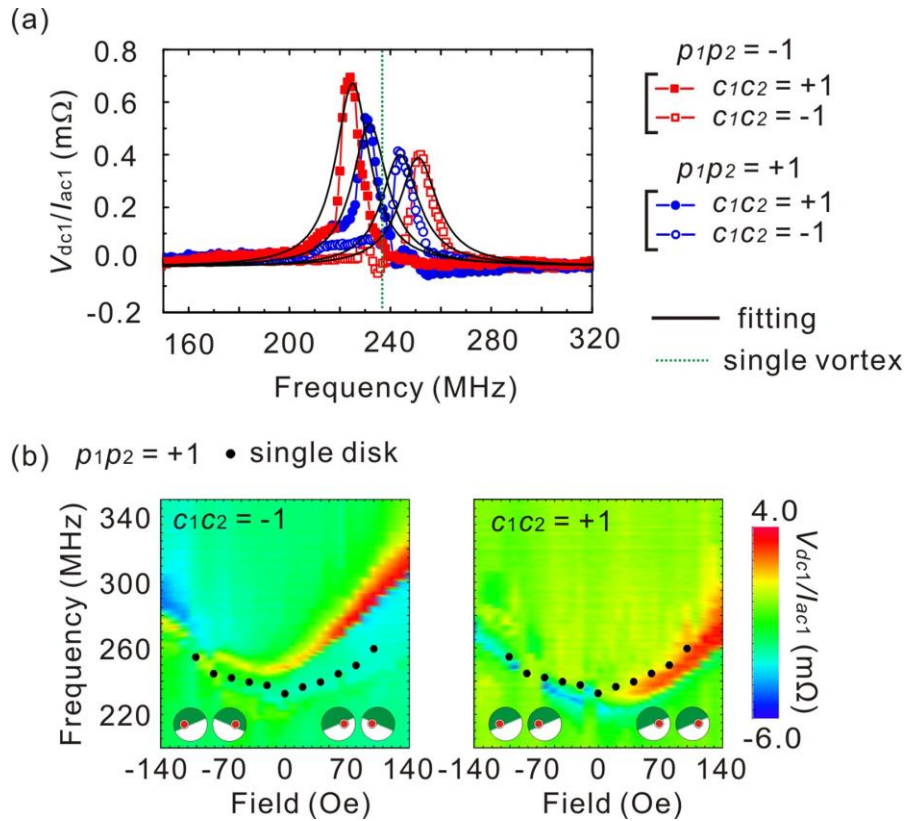
FIG. 5.8: (a) Resonant spectra of two coupled vortices by means of local excitation. (b) External field dependence of resonant spectra $(p_1 p_2, c_1 c_2) = (+1, \pm 1)$. The external field is applied orthogonal to coupling direction. Cartoons of core shits are inserted at positive and negative sides of external field.

$c_1 c_2 = +1$ (closed symbols in Fig. 5.8 (a)). The excitation amplitude at each mode is also different from results of local excitation. The amplitude $|V_{dc1}/I_{ac1}|$ decreases with increase of eigenfrequency

of coupled modes, and falls to minimum at $\omega_{\gamma,-1}{}^*$. The chiralities $c_1 c_2$ of the remanent state were separately checked by in-plane field dependence of resonant spectra. Two examples with parallel polarities $p_1 p_2 = +1$ are shown in Fig. 5.8 (b). Using the same frame with field tunings of single vortex in Sec.4.2, a monotonic increase of eigenfrequency is observed with increasing external field. Different from single vortex, in-plane field tuning of neighboring vortices also affect magnetic dipolar interaction via side magnetic charges. When the external field applied orthogonal to coupling direction, two cores shift parallel to coupling direction depending on chiralities $c_1 c_2$. In a case of chiralities are same $c_1 c_2 = +1$, two cores are deflected a same direction and core to core distance is almost constant, thus the filed dependence of spectra becomes a symmetric curve with respect to zero magnetic field similar with that of the single vortex (see right graph in Fig. 5.8 (b)). On the contrary, Different chiralities $c_1 c_2 = -1$ cause cores shit onto opposite direction. Thus core to core distance is tuned by direction of external field and magnetic dipolar coupling is also modified by field tuning. It results in the asymmetry resonant curve in the left graph of Fig. 5.8 (b). In this manner, chiralities $c_1 c_2$ of remanent state can be read out from field tuning.

$(p_1 p_2, c_1 c_2)$ depending selective excitation results in Fig. 5.8 (a) enable to discuss not only the effect of chiralities but also details of current-induced excitation torque qualitatively. Figure 5.9 shows schematic image of possible core dynamics for given $(p_1 p_2, c_1 c_2)$ by means of global excitation. Firstly, only the current-induced Oersted ac field is considered as a torque in Fig. 5.9 (a). The field induced torque $-cq\boldsymbol{e}_z \times \boldsymbol{H}$ is proportional to chirality of each vortex but independent from polarity, and drives cores orthogonal to in-plane field direction. For $(p_1 p_2, c_1 c_2) = (+1, +1)$, this field induced torque drive two cores same and parallel to current direction and two cores rotate in-phase $(\Delta\Phi = 0)$ at the steady state. Such configuration corresponds to bonding mode with $p_1 p_2 = +1: \omega_{\gamma,+1}$. On the contrary, for $(p_1 p_2, c_1 c_2) = (+1, -1)$, i.e. the chirality of the vortex 2 is reversed, two cores are first driven opposite but parallel to current direction thus they rotate opposite phase $(\Delta\Phi = \pi)$ at steady state. Note that this configuration is energetically identical with a case of $(p_1 p_2, c_1 c_2) = (+1, +1)$, i.e. bonding mode with $p_1 p_2 = +1: \omega_{\gamma,+1}$. As discussed in Sec. 2.7, stray field distributions are identical with opposite chiralities and opposite directions of core shit. In all rotating process of $p_1 p_2 = +1$ and $\Delta\Phi = \pi$, the core position of vortex 2 locates symmetric positions with respect to the core compared with that of $p_1 p_2 = +1$ and $\Delta\Phi = 0$. Therefore, The field induced torque $-cq\boldsymbol{e}_z \times \boldsymbol{H}$ excites only the bonding mode for $p_1 p_2 = +1: \omega_{\gamma,+1}$ with any configurations of chiralities $c_1 c_2 = \pm 1$. Using the same manner, the field induced torque $-cq\boldsymbol{e}_z \times \boldsymbol{H}$ excites also bonding mode for $p_1 p_2 = -1: \omega_{\gamma,-1}$ independent from chiralities $c_1 c_2 = \pm 1$ (see lower two states in Fig. 5.9 (a)). These results are obviously conflict with experimental report in Fig. 5.8 (a), where both the bonding and antibonding modes are excited by switching chiralities $c_1 c_2$. Secondly, only the adiabatic spin transfer torque is considered as current-induced torque (Fig. 5.9 (b)). The adiabatic spin transfer torque causing gyroforce $\boldsymbol{G}(p_i) \times \boldsymbol{u}$ switches with polarities p_i while the field induced torque $-cq\boldsymbol{e}_z \times \boldsymbol{H}$ switches with chiralities c_i. For $(p_1 p_2, c_1 c_2) = (+1, +1)$, the spin torque drive two cores same but orthogonal to current direction, i.e. initially deflected direction is

orthogonal to that by field induced torque. However, two cores rotate in phase ($\Delta\Phi = 0$) and the coupling energy at steady state is identical with a case of field excitation: bonding mode with $p_1p_2 = +1$: $\omega_{\gamma,+1}$. The clear difference appears for $(p_1p_2, c_1c_2) = (+1, -1)$. Since the spin torque is independent from chiralities, initially deflected direction is same with $(p_1p_2, c_1c_2) = (+1, +1)$ and two cores rotates in phase ($\Delta\Phi = 0$) at steady state. However, this configuration is energetically unfavourable since neighboring chiralities are different $c_1c_2 = -1$. Consequently, Antibonding mode $\omega_{\gamma,+1}{}^*$ is excited for $(p_1p_2, c_1c_2) = (+1, -1)$. Using the same manner for antiparallel polarities $p_1p_2 = -1$, bonding mode $\omega_{\gamma,-1}$ for same chiralities $c_1c_2 = +1$ and antibonding mode $\omega_{\gamma,-1}{}^*$ for opposite chiralities $c_1c_2 = -1$ are excited. As a consequent, the adiabatic spin torque can excite all four coupled modes with means of global excitation while field induced torque can only excite two bonding modes. Experimental results are well described in the frame of adiabatic spin
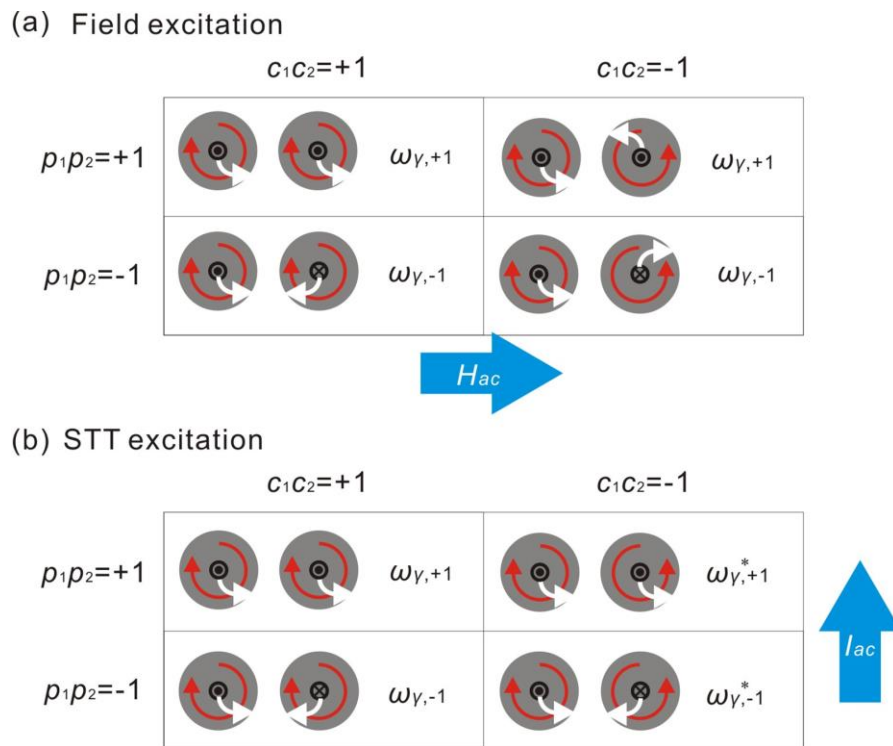
FIG. 5.9: Schematic image of current-induced core dynamics by means of global excitation for different combinations of (p_1p_2, c_1c_2), (a) by Oersted ac field or (b) by adiabatic spin transfer torque.

torque excitation. These insights are consistency with early works of spin torque diode effect in chapter 4, where the adiabatic spin transfer torque is estimated as the more dominant factor of excitation torque.

5.2.4. Phase detection

Studies of local and global excitation enable to discuss roles of polarities $p_1 p_2$, chiralities $c_1 c_2$ and phase difference $\Delta\Phi$ onto the dynamics of two coupled vortices via magnetic dipolar interaction. Their results indicate the chiralities $c_1 c_2$ and phase difference $\Delta\Phi$ take a complementary relation and phase detectable measurement is required to directly discuss details of coupled dynamics determined by $(p_1 p_2, c_1 c_2, \Delta\Phi)$.

By using return loss measurement circuit, the phase relation of injected current I_{ac1} and I_{ac2} are precisely coordinated with the same manner of heterodyne detection in Sec. 4.2. A large current is injected to the left disk ($I_{ac1} = 2.7$ mA) enough for excitation while a small current is used to the right disk ($I_{ac2} = 0.5$ mA) for detecting the core motion without disturbing the induced gyration motion. It is worth mentioning the excitation condition of phase detection is identical with early local excitation except for small detection current flowing in vortex 2.

Firstly, directly excited spectra at the left vortex 1 are discussed. Figures 5.10 (a) and (b) show frequency dependences of normalized rectified voltage V_{dc1}/I_{ac1} for two different combinations of polarities $p_1 p_2 = -1$ and $p_1 p_2 = +1$, respectively. Two resonant peaks were observed at the low (f_L) and high (f_H) frequencies for each combination. In this situation, the degree of freedom for the two chiralities $c_1 c_2 = \pm 1$ is still degenerated at the eigenfrequency. The splitting amplitude of the resonant frequency ($f_H - f_L$) depends only on polarities $p_1 p_2$. Naturally these results are exactly same with resonant spectra of local excitation method (Fig. 5.4), assuring additional detection current I_{ac2} does not affect the whole coupled dynamics. The degeneracy in chiralities $c_1 c_2$ can be lifted in spectra at the right vortex 2. Figures 5.10 (c) and (d) show spectra at the vortex 2 V_{dc2}/I_{ac2} for the two different combinations of chiralities $c_1 c_2 = -1$ and $c_1 c_2 = +1$, respectively. Two resonant lines are observed at f_L and f_H, showing neighboring vortex 2 is surely excited via magnetic dipolar interaction between vortex 1 as predicted micromagnetic simulations in Fig. 5.7. However, signs at resonant lines differ from left spectra in Fig. 5.10 (a): dip and peak are respectively observed at f_L and f_H for $c_1 c_2 = -1$ whereas peak and dip are observed for $c_1 c_2 = +1$. The core rotation results in a resistance change via the AMR of ferromagnetic disk and observed through homodyne detection. Due to the small asymmetry of a sample, resistance of disk 2 has sinusoidally varied component in AMR with ω as discussed in Sec. 4.2. Therefore rectified voltage at vortex 2 is simplified as

$$V_{dc2} \approx \int \Delta R \sin(2\pi f t + \Delta\Phi) \cdot I_{ac2} \sin(2\pi f t + \Delta\varphi)\, dt. \tag{5.6}$$

If I_{ac1} and I_{ac2} are injected without any phase difference ($\Delta\varphi = 0$), the rectifying voltage V_{dc2} should have a positive sign with $\Delta\Phi = 0$, or a negative sign with $\Delta\Phi = \pi$. Therefore sign inversion at f_L and f_H in Fig. 5.10 (c), (d) and (e) can be regarded that the coupled precessions of two cores changes from in phase mode $\Delta\Phi = 0$ to opposite phase mode $\Delta\Phi = \pi$, as predicted micromagnetic simulation in Fig. 5.7. A complementary relation of chiralities $c_1 c_2$ and phase difference $\Delta\Phi$ is also explained using this frame. Sings at f_L and f_H changes by switching chiralities $c_1 c_2$ (see Fig. 5.10 (c) and (d)). Note that chirality themselves affect neither the core dynamics nor AMR, thus sign inversion of f_L between Fig. 5.10 (c) and (d) indicate that in-phase precession with same chiralities
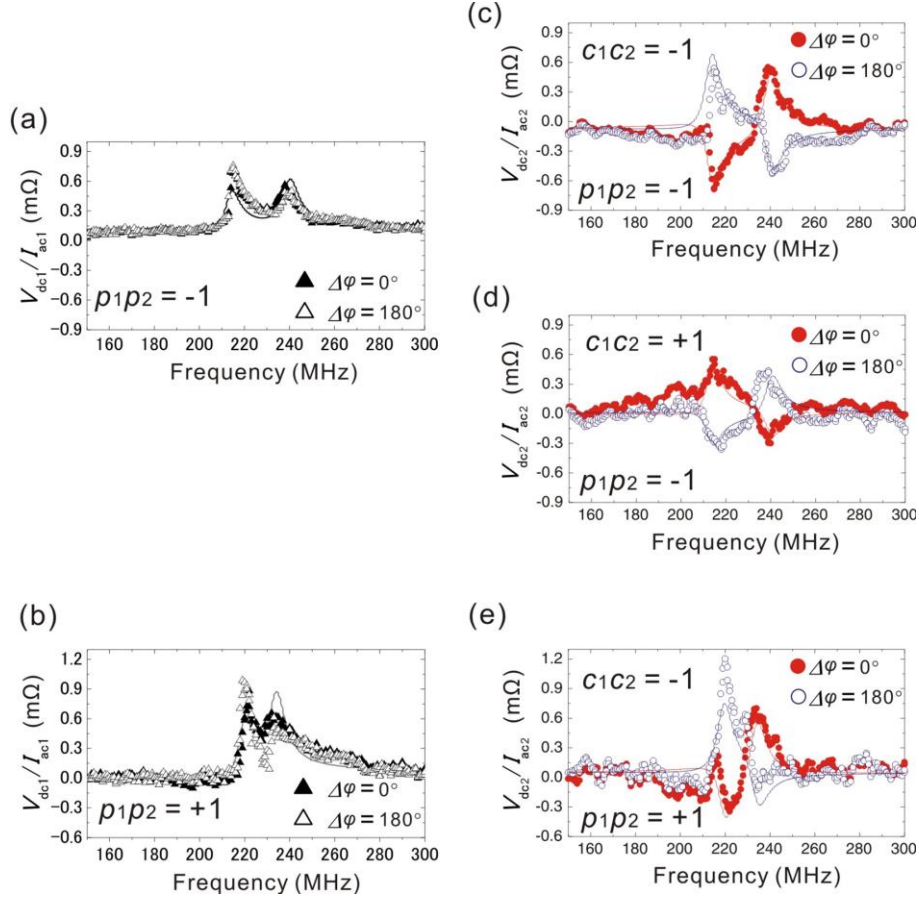
FIG. 5.10: (a) and (b) Resonant spectra of the two-coupled vortices measured at the left vortex 1 by means of local excitation. The polarity combination is parallel $p_1 p_2 = -1$ for (a) and antiparallel $p_1 p_2 = +1$ for (b). Closed and open symbols indicate the data obtained with $\Delta\varphi = 0$ and $\Delta\varphi = \pi$, respectively. The solid lines are the best fits of the experimental data. (c)-(e) Resonant spectra of the two-coupled vortices measured at the right disk. $p_1 p_2 = -1$ for (c) and (d) and $p_1 p_2 = +1$ for (e) while $c_1 c_2 = -1$ for (c) and (e) and $c_1 c_2 = +1$ for d). Closed and open symbols and solid lines in (c)-(e) have the same meanings with those in (a) and (b).

$(c_1 c_2, \Delta\Phi) = (+1, 0)$ (red plots in (d)) is energetically identical with opposite phase precession with different chiralities $(c_1 c_2, \Delta\Phi) = (-1, \pi)$ (red plots in (c)), corresponding a boding mode $\omega_{\gamma, -1}$. Completely using same manner, opposite phase precession with same chiralities $(c_1 c_2, \Delta\Phi) = (+1, \pi)$ is equal to in-phase precession with different chiralities $(c_1 c_2, \Delta\Phi) = (-1, 0)$, corresponding a boding mode $\omega_{\gamma, -1}^*$ at f_H. Apart from these magnetization property, the phase difference of current $\Delta\varphi$ also cause sign inversion at f_L and f_H. Compare blue and red symbol in Fig. 5.10 (c)-(d).

Consequently all roles of polarities $p_1 p_2$, chiralities $c_1 c_2$ and phase difference $\Delta\Phi$ onto the dynamics of two coupled vortices are experimentally demonstrated. In other words, the energy scheme of coupled vortices can be uniquely identified by selecting these characteristics, polarities and chiralities, and phase difference $(p_1 p_2, c_1 c_2, \Delta\Phi)$. Since each characteristic takes two degrees identically, there are in total eight different states for the two-coupled vortices.
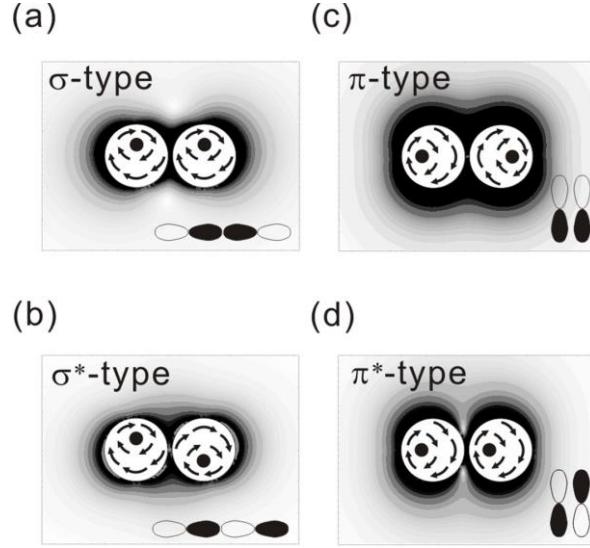
FIG. 5.11: Dipolar field distributions of two-coupled magnetic vortices for different core positions calculated with micromagnetic simulator. The intensity of the dipolar field is expressed by gray scale. Black dots and arrows indicate the positions of cores (not including the polarity directions) and the in-plane magnetization directions, respectively. Since the dipolar field distribution resembles the p-orbital wave function of a diatomic molecule, the gyration processes depicted in (a), (b), (c), and (d) can be named as the σ-, $\sigma*$-, π-, and $\pi*$-type states of the p-like orbits, respectively. As can be seen later on, all the eigenstates in the two-coupled vortices can be well described with the analogy of the energy scheme of these states.

To help understanding of relations of core phases and coupling energy, dipolar field distributions of two-coupled magnetic vortices for different core positions are calculated with micromagnetic simulator in Fig. 5.11. The relation of all energy levels and vortex dynamics in Fig. 5.10 can be explained from these calculations. As an example, in a case with $p_1 p_2 = -1$, $c_1 c_2 = +1$ (Fig. 5.10 (d)) at $f = f_L$ is considered. In this case, the two vortex cores rotate with $f = f_L$ keeping in phase together, i.e., $\Delta\Phi = 0$ (see Fig. 5.11 (b)). Since the vortex core always rotates in the counterclockwise direction for the polarization direction, Fig. 5.11 (b) changes into Fig. Fig. 5.11 (d) after a quarter cycle (t $= 1/(4f_L)$) and comes back to the same state in one cycle (t $= 1/f_L$). When $f = f_H$, another eigenstate appears where the two vortex cores rotate keeping $\Delta\Phi = \pi$ (see Fig. 5.11 (c)). As in the case of $f = f_L$, Fig. 5.11 (c) changes into Fig. 5.11 (e) after a quarter cycle (t $= 1/(4f_H)$) and comes back to the same state in one cycle $1/f_H$).

Using this frame, coupled modes can be labeled fairly by combining four types of states those show same bonding symmetry with p-states in homo nuclear diatomic molecules. In the p-orbits, there exist
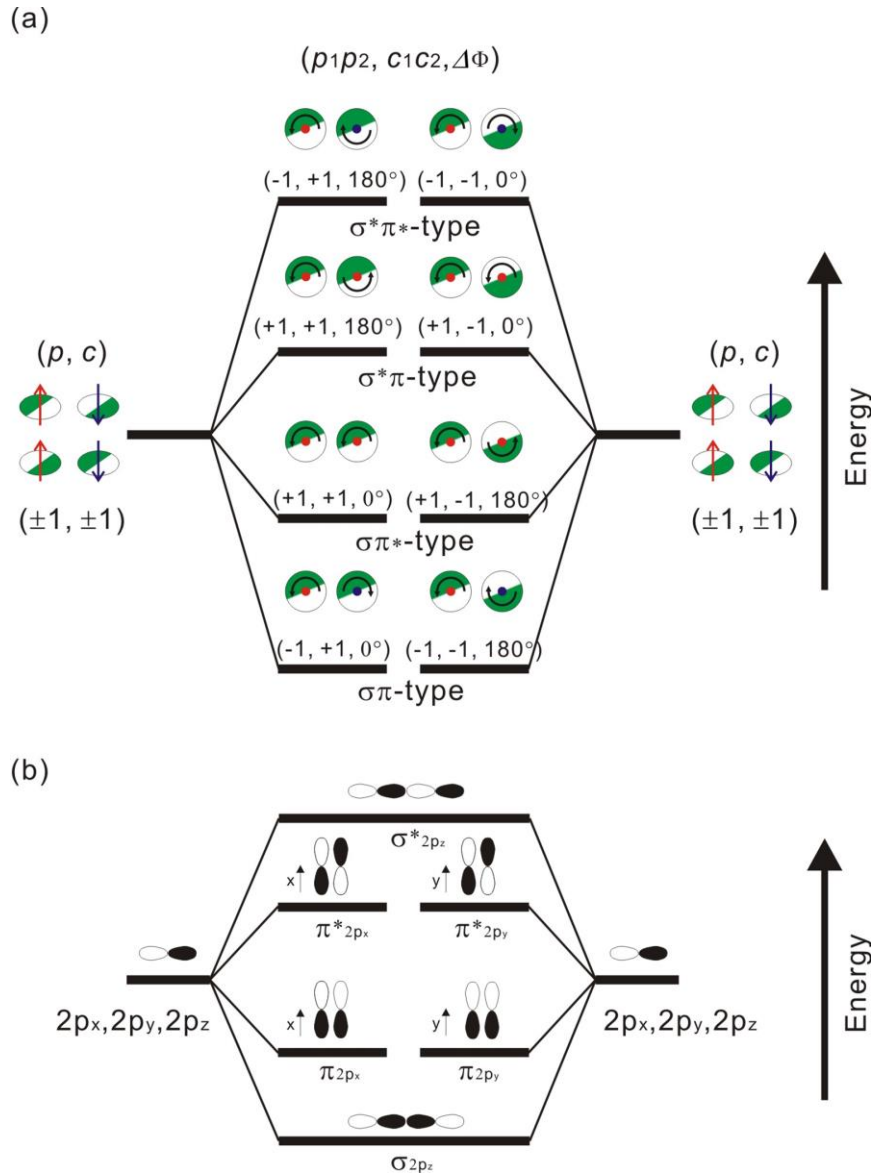

FIG. 5.12: (a) Energy levels of two-coupled magnetic vortices. There are in total eight different states depending on the combinations of polarities ($p_1 p_2 = \pm 1$), chiralities ($c_1 c_2 = \pm 1$), and the phase difference between the two cores ($\Delta \Phi = 0, \pi$). (b) Bonding and anti-bonding states of $2p$-orbits of diatomic molecules.

σ- and π-bonding states as well as their anti-bonding states ($\sigma*$ and $\pi*$). For example, Fig. 5.11 (a) corresponds to the σ-type state since the stray field (regarded as a wave function in p-states) distributes orthogonal to the binding axis. After a quarter cycle, for $p_1 p_2 = -1$, Fig. 5.11 (a) changes into Fig. 5.11 (c) which corresponds to the π-type state (parallel to the binding axis). For $p_1 p_2 = +1$, on the other hand, Fig. 5.11 (a) changes into Fig. 5.11 (d) which corresponds to the $\pi*$-type state. This

$\pi*$-type state has a node in between the two vortices like an anti-bonding state in diatomic molecules. The reason why the $p_1 p_2 = -1$ state ($\sigma\pi$-type: equal to $\omega_{\gamma,-1}$) takes a lower energy than the $p_1 p_2 = +1$ state ($\sigma\pi*$-type: equal to $\omega_{\gamma,+1}$) can be explained in such a manner. In fact, all energy states in Fig. 5.10 can be explained by the combinations of the σ- or $\sigma*$-, and π- or $\pi*$-type states. The energy scheme of two coupled vortices via magnetic dipolar interaction is shown in Fig. 5.12 (a), using the manner. As comparison, energy scheme of $2p$-orbits of diatomic molecules with atomic number $Z \geq 8$ is also shown in Fig. 5.12 (b). Note that there exists surely geometric analogy in Fig. 5.12 (a) and Fig. 5.12 (b) while energy scales are totally different, the former is coupled via magnetic dipolar interaction whereas the latter is coupled via covalent Interaction. Interesting point of magnetic diatomic molecules of two coupled vortices in Fig. 5.12 (a) is that the bonding symmetry, which decides coupling energy, is systematically tuned by selecting independent unique three parameters of vortex structure, polarities, chiralities and phase difference of core dynamics. These three degrees of freedoms are degenerated in single vortex, just like directionality of $2p$-orbits, p_x, p_y, p_z. Once two elements are coupled these degenerations are resolved and 2 bonding and 2 antibonding states are formed, respectively.

5.2.5. Free excitation

So far, all eigenstates of two coupled vortices are found out to be labelled by three independent parameters $(p_1 p_2, c_1 c_2, \Delta\Phi)$. In other word, any eigenstates can be selectively excited by determined theses parameters. Figure 5.13 shows resonant spectra measured at the left and right disks for $I_{ac1} = I_{ac2} = 1.4$ mA but phase difference of current $\Delta\varphi$ is freely rotated. Obviously, one peak is quite suppressed but instead the other peak is enhanced both for the left and right vortex, showing specific eigenstate is selectively excited. For $(p_1 p_2, c_1 c_2, \Delta\varphi) = (-1, -1, 0)$ plotted by red closed symbols in Figure 5.13, antibonding mode $\sigma*\pi*$-type state in Fig. 5.12 is excited. For $(p_1 p_2, c_1 c_2, \Delta\varphi) = (-1, -1, \pi)$ plotted by blue open symbols, bonding mode $\sigma\pi$-type state in Fig.
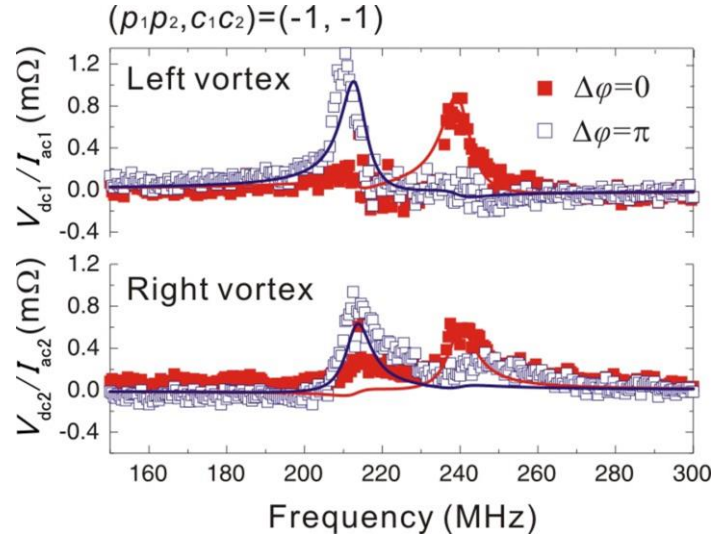

FIG. 5.13: Resonant spectra detected at the left vortex 1 (upper) and right vortex 2 (lower panel) by means of free excitation (i.e., $I_{ac1} = I_{ac2}$). The polarity and chirality combinations are $p_1 p_2 = -1$ and $c_1 c_2 = -1$, respectively. Closed and open squares correspond to results of in-phase excitation $\Delta\Phi = 0$ and opposite phase excitation $\Delta\Phi = \pi$.

5.12 is excited. Its selection principle is followed by energy scheme in Fig. 5.12.

Results of continuous phase tuning $0 \leq \Delta\varphi \leq 2\pi$ of free excitation spectra are plotted as functions of excitation frequency and the phase difference $\Delta\varphi$. Each modes are selectively excited by following selection principles in Fig. 5.12, even though changing chiralities $c_1 c_2 = \pm 1$ (see (a) and (b), or (d) and (e), in Fig. 5.14) and polarities $p_1 p_2 = \pm 1$ (see (a) and (c), or (d) and (e) in Fig. 5.14). By changing $\Delta\varphi$ systematically, it turns out that the splitting amplitude between bonding mode and antibonding mode stays constant even though at intermediate region, i.e. $0 < \Delta\varphi < \pi$ and $\pi < \Delta\varphi < 2\pi$. Suppose the core rotation would synchronize with current rotation, the magnetic dipolar interaction energy could decrease at this region and bonding and antibonding modes have to be degenerated to the original eigenstate of single vortex at $\Delta\varphi = \pi/2$ and $\Delta\varphi = 3\pi/2$. In other words, the relative phase between the two vortices $\Delta\Phi$ is locked at $0 < \Delta\varphi < \pi$ and $\pi < \Delta\varphi < 2\pi$; it can be said as a kind of a mutual phase lock[121] of the coupled gyration mode. Such a mutual phase lock

had already been studied in spin torque nano-oscillators where a direct exchange coupling of ferromagnetic layers plays an important role[122]. In the present system, the magnetic dipolar coupling is the origin of the interaction[123]. One can suppress the energy dissipation with scale expansion because of the long-range interaction and also select a specific eigenfrequency state by modulating the phase difference. Furthermore, it is meaningful for device application that the phase locking has been demonstrated under the zero magnetic field.
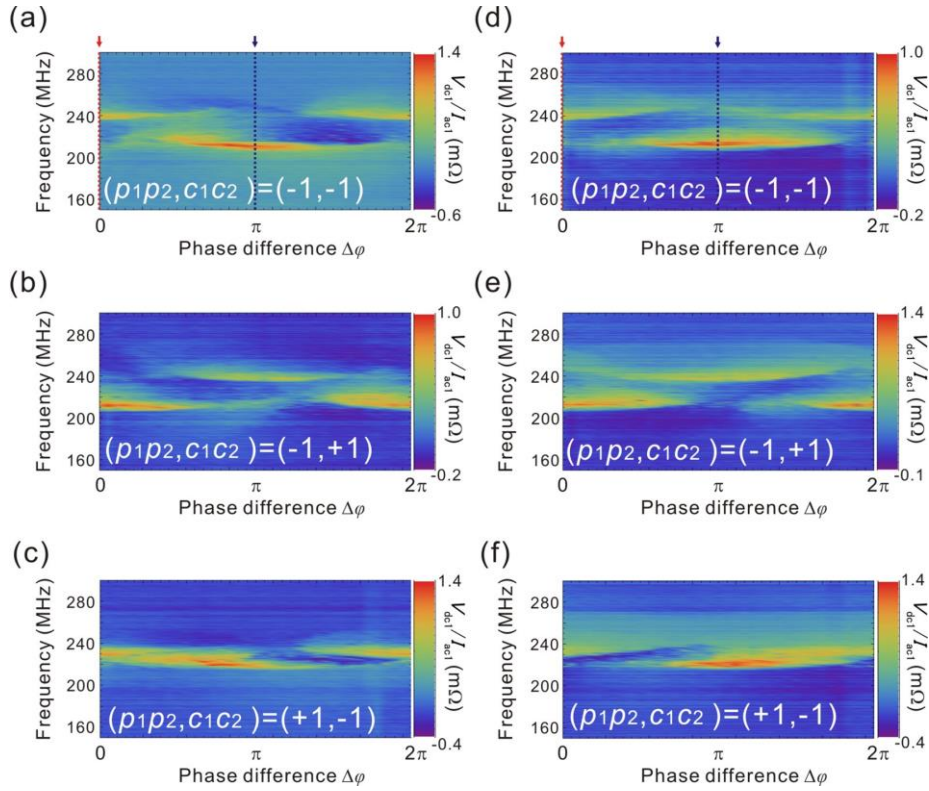
FIG. 5.14: (a)-(f) Color plots of resonant spectra as a function of phase difference of current $\Delta\varphi$ detected at the left vortex 1 (a)-(c) and right vortex 2 (d)-(f). Red and blue arrows in (a) and (d) indicate spectra shown in Fig. 5.13.

5.2.6. Energy scheme as magnetic diatomic molecules

Separate distance dependence of the coupling energy

The more quantitative discussions are held in this section. Normalized center to center dependence $d = D/R$ of eigenfrequencies of coupled modes is plotted in Fig. 5.15. The center to center distance is varied from 1075 nm to 1200 nm (from 75 nm to 200 nm in edge to edge distance). The frequency splits are spoiled with increase the distance by necessity and $\sigma\pi*$- and $\sigma*\pi$-type modes (smaller splits with parallel polarities $p_1 p_2 = +1$) become to be degenerated at $d = 2.25$ (125 nm). Results of Fig. 5.15 (a) are further converted to the coupling integrals (η_x, η_y), throughout fittings of spectra at each distance (see solid curves in Fig. 5.4). Note that coupling integrals are theoretically predicted in Eq. 5.3 but treated as fitting parameters in Fig. 5.4 (b). Other physical quantities use for these fittings are listed in Table B in Sec. 4.2. Reflecting linear directionality of dipolar field, values of η_y keeps larger more than twice values of η_x, and they monotonically increase with decrease separate distance. Separate distance dependence of η_x is nicely fitted using distance to minus fourth power d^{-4} and that of η_y can be fitted by distance to minus sixth power d^{-6}, just as predicted in theory in
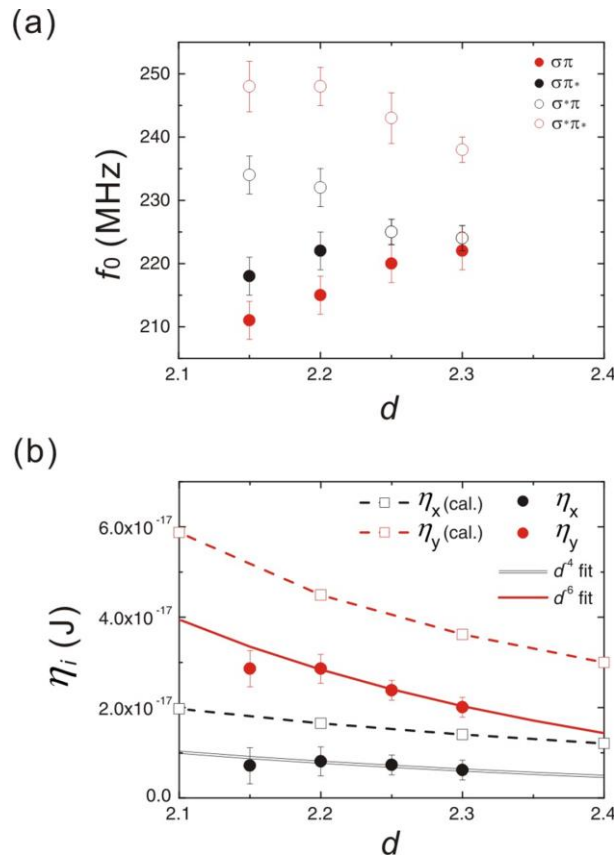
FIG. 5.15: (a) Separate distance dependence of resonant frequencies of four coupled modes. (b) Separate distance dependence of the coupling integrals (η_x, η_y) estimated from fittings at each distance of Fig. 5.15 (a) (solid symbols). The analytical estimations of coupling integrals (η_x, η_y) are plotted by blank symbols. These results are obtained by means of local excitation with $I_{ac1} = 2.5$ mA

Eq. 5.3. Therefore dipolar coupled magnetic vortices show more analogy with the van der Waals molecular coupling rather than covalent coupling on the point of coupling intensity of system. Analytical calculations of coupling integrals (η_x, η_y) are plotted using open symbols in Fig. 5.15 (b). There exist small increase from experimental results showing magnetization configuration at side surface slightly relax from complete circular alignment supposed in rigid vortex model. A small decrease at the shortest separate distance ($d = 2.05$) may be caused by surface defect or higher-order multipole terms[123].

Zeeman like effect

In the energy scheme in Fig. 5.12 (a), chiralities c_1c_2 are degenerated at all four energy levels of the
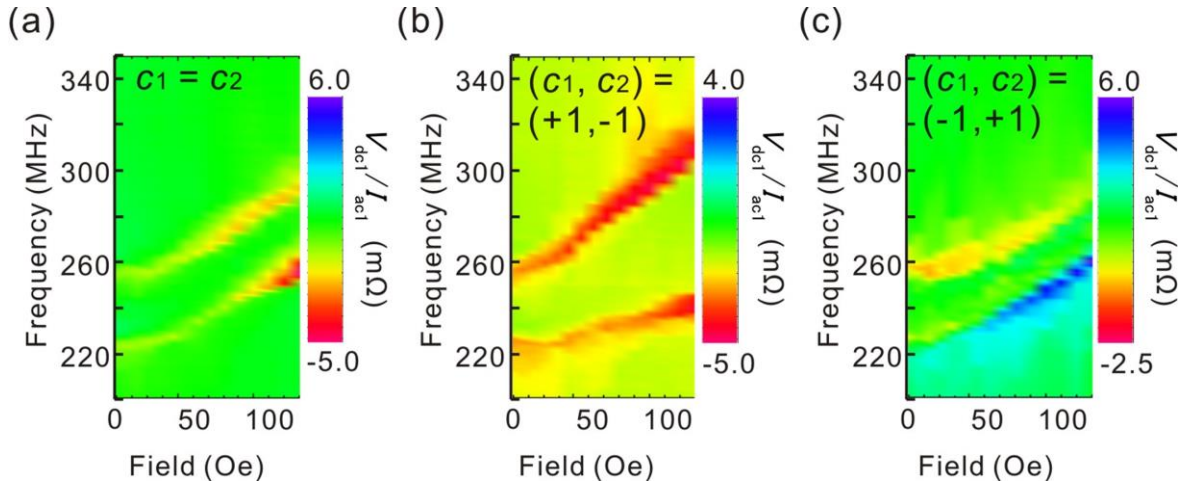
FIG. 5.16: In plane field dependencies of spectra with three different combinations of chiralities: (a) $c_1 = c_2$, (b) $(c_1c_2) = (+1, -1)$ and (c) $(c_1c_2) = (-1, +1)$. The static field is orthogonally applied to the coupling direction. These results are obtained by means of local excitation with $I_{ac1} = 2.5$ mA

artificial molecular system. Here in-plane static field h tuning for degenerated chiralities c_1c_2, such like Zeeman effect in real molecules, is demonstrated and further discussions are held showing analogy of chiralities c_1c_2 with pseudospin. Figure 5.16 (a)-(c) shows in plane field dependencies applied orthogonal to bonding axis. Besides the usual monotonic blue shift of vortices with $c_1 = c_2$ in Fig. 5.16 (a), resonant frequencies f_0 additionally show asymmetric shifts in cases of different
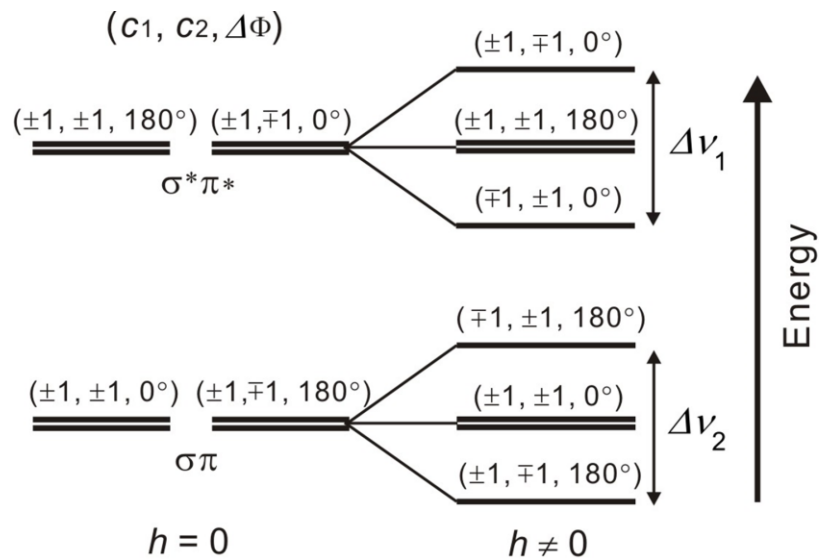
FIG. 5.17: Energy splitting labeling by signs of chiralities: (c_1c_2) with $p_1p_2 = -1$.
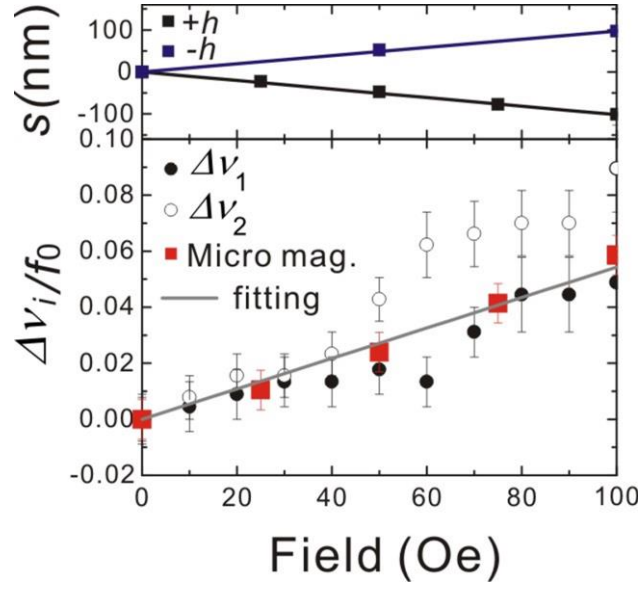
FIG. 5.18: Field dependencies of simulated distances of core shift s under the static field (upper part) and frequency splits of $\sigma*\pi*$-type mode ($v_1$) and $\sigma\pi$-type (v_2) (lower part). The simulation resonant frequencies under static field are plotted by red squares and fitting results using Eq. 5.7 is shown by grey line.

chiralities $(c_1 c_2) = (\pm 1, \mp 1)$. Under the static field, external field shifts equilibrium positions of cores so as to suppress increments of magnetostatic energy. Directions of core shifts only depend on signs of chiralities $c_i = \pm 1$ thus different chiralities results in effective increase with closer cores (larger frequency spit with $(c_1 c_2) = (+1, -1)$ in Fig. 5.16 (b)) or decrease with farther cores (smaller split with $(c_1 c_2) = (-1, +1)$ in Fig. 5.16 (c)) of dipolar interaction.

Figure 5.17 shows frequency splits with antiparallel polarities $p_1 p_2 = -1$. When distances of core shifts ($-ah$ for $h > 0$ and $+bh$ for $h < 0$) are quite small rather than radii of disks and excitation amplitudes, tuned resonant frequencies (f_{+i} for $h < 0$ and f_{-i} for $h > 0$, here $i = 1$ for $\sigma*\pi*$-type mode and $i = 2$ for $\sigma\pi$-type mode) are assumed to show distance dependency of molecular system $f_{\pm i} \propto d^{-6}$ for effective core to core distances $d - ah$ or $d + bh$. The dimensionless parameter $\Delta v_i / f_0 \equiv (f_{+i} - f_{-i})/f_0$ is approximated using first order Taylor expansion as

$$\frac{\Delta v_i}{f_0} \sim \frac{((d-ah)^{-6} - (d+bh)^{-6})}{d^{-6}} = \frac{6(a+b)}{d} h + O\left(\left|\frac{ah}{d}\right|^2\right) + O\left(\left|\frac{bh}{d}\right|^2\right). \tag{5.7}$$

Our micromagnetic simulations enable us to estimate liner response of core shift for applied field as $a = b = (1.0 \pm 0.0)$ (see upper part of Fig. 6(b)) as predicted Thiele equation in Sec. 2.6. Experimental and simulation results of $\Delta v_i / f_0$ in Fig. 6(b) are both proportional to static field h as introduced by Eq. 5.7 especially at small field range $h < 100$ Oe. Such linear field dependency shows similarity to Zeeman effect in molecular system and degenerated chiralities in coupled vortices effectively act as nuclear spins quantum number under the existence of static field.

5.3. Time domain measurements

The damping process of two coupled vortices has been also investigated via time-resolved MOKE measurement. Device structures are basically same with those of the single vortex sample in Sec. 4.3,
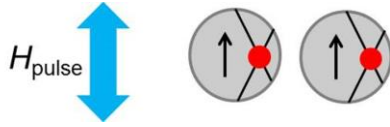
FIG. 5.19: Illustration of the excitation direction of time resolved MOKE measurement for coupled two vortices.

two neighboring ferromagnetic disks are deposited along the excitation stripline, i.e. excitation linear field pulse is applied orthogonal to the coupling direction (Fig.5.19). Using frames of Fig. 5.12, one can notice that this alignment cannot excite all four coupled modes but only two $\sigma\pi*$ -type mode for parallel polarities $p_1 p_2 = +1$ and $\sigma*\pi*$-type mode for antiparallel polarities $p_1 p_2 = -1$. In

this section, polarities are set to be the parallel alignment $p_1 p_2 = +1$ and the coupling effect is discussed via frequency shifts from the eigenstate of the single vortex.

Figure 5.20 shows time-resolved Kerr rotation measured by two neighboring vortices with different separate distances, from 300 nm to 600 nm in edge to edge distance. All results can be fitted by
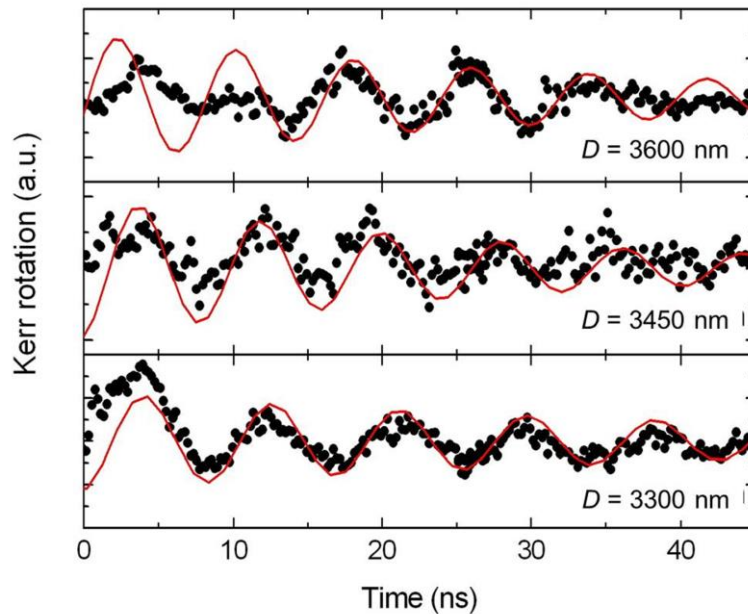
FIG. 5.20: Time-resolved Kerr rotation signals detected at left disks with various center to center separation distance: $D = 3600\ \text{nm}, 3450\ \text{nm}, 3300\ \text{nm}$. Polarities are set to be parallel alignment $p_1 p_2 = +1$.

exponentially decayed sinusoidal curves (Eq. 4.5 in Sec.4.3), showing damping processes are observed.

Obtained eigenfrequencies of the $\sigma\pi*$-type mode from these fittings are plotted as a function of normalized separate distance d in Fig, 5.21. The $\sigma\pi*$-type mode appears lower frequency side from the original eigenstate of single vortex. As predicted, the shorter separation distance results in slower core precession. Coupling integrals (η_x, η_y) are also derived from these frequency shift (lower panel of Fig. 5.21, and shows same distance dependence with results of frequency domain measurements in
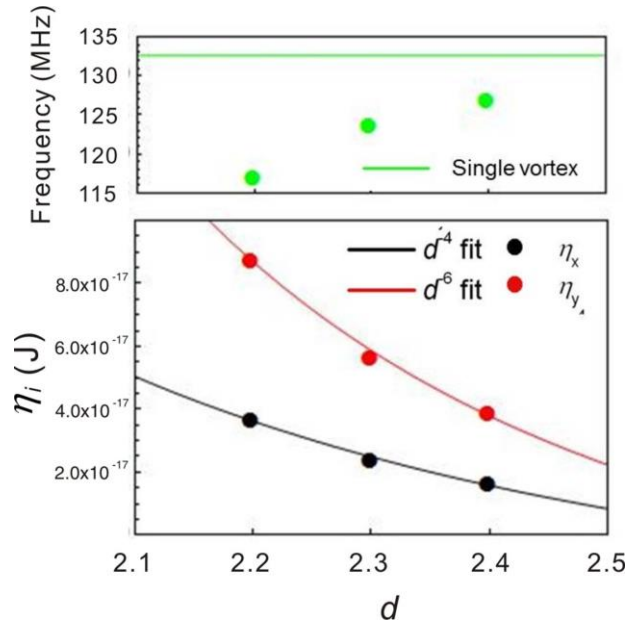
FIG. 5.21: Separation distance dependence of the eigenfrequency of $\sigma\pi*$-type mode (upper) and the coupling integral (η_x, η_y) (lower panel).

Fig. 5.15. Therefore, observed blue shift in neighboring two vortices is revealed to be caused by the magnetic dipolar coupling.

Apart from such frequency properties, time-resolved measurement enables to discuss the velocity of the energy dissipation process directly. Experimentally estimated the damping parameter Γ is shown in Fig. 5.22 as a function of separate distance. The parameter Γ does not explicitly depend on the separation distance, i.e. coupling intensity, showing energy dissipation process eventually has little relation with the coupling mechanism and damping of permalloy film can be crucial factor for dissipation. Suppose large numbers of coupled vortices, even though 1- or 2 dimensional coupled vortices with an infinite length, possess comparable values of Γ with single vortex. This property suggests the vortex structure is good for scalability as spin wave propagation media[8].
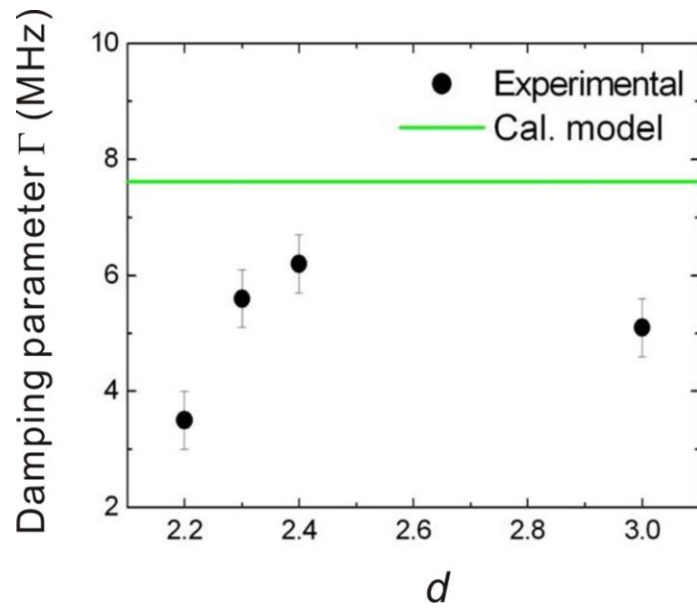
FIG. 5.22: Separation distance dependence of the damping parameter Γ estimated using Eq. 4.5 from results of Fig. 5.20.

6. 1 dimensional Magnonic crystal via coupled vortices

After discussing two coupled magnetic vortices as a unit of vortex used magnonic crystal, this chapter finally deal with dynamics of 1 dimensionally coupled chained vortices.

In Sec. 6.1, experimental results of 3 chained vortices are first introduced. The dynamics is examined using phase detectable frequency sensor in chapter 5. From insights of 3 chained vortices, a principle of system expansions onto the 1 dimensionally system is discussed. In Sec. 6.2, the generalized Thiele equation with magnetic dipolar interaction term is resolved and energy scheme of 1 dimensionally coupled vortices is analytically determined.

6.1. 1 dimensional magnonic crystal

The simplest extension of two coupled system is investigated: 3chinaed magnetic vortices with uniform dimensions in dot shapes and center to center separate distances $(R_i, L_i, D_i) = (500 \text{ nm}, 30 \text{ nm}, 1100 \text{ nm})$. Figure 6.1 shows experimental circuit which works as same manner of phase detection / free excitation. Here the microwave antennas attached to the right vortex 1 and the left vortex 3. The resonant spectra obtained by phase detection manner are shown in Figs. 6.2 (a) and (b), i.e. the vortex 1 is locally excited by $I_{ac1} = 2.0 \text{ mA}$ and the phase detection current $I_{ac2} = 0.5 \text{ mA}$ is injected into the vortex 3. Polarities and chiralities are set as $(p_1, p_2, p_3) = (+1, -1, +1)$ and $(c_1, c_2, c_3) = (+1, +1, +1)$. Obviously different from results of two coupled
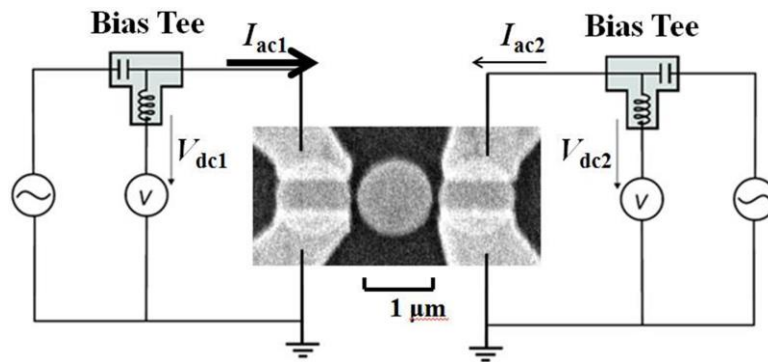
FIG. 6.1: Schematic image of measurement set up for 3 chained vortices including SEM image of a sample.

vortices are observed, 3 resonant modes are observed at the excitation spectra (at vortex 1) and detection spectra (at vortex 3), one is same frequency with the original eigenfrequency ($f_M \cong$ 230 MHz) and the others two are resonantly excited at both lower frequency f_L and higher frequency

f_H with around 20 MHz intervals $(f_L \cong 210$ MHz, $f_H \cong 250$ MHz). Signs of detection spectra in Fig. 6.2 (b) show positive peaks at f_L and f_H while a negative dip at f_M for same phase detection $\Delta\varphi = 0$, showing vortices 1 & 3 rotate at a same phase at f_L and f_H while they rotate at an opposite phase at f_M. By taking into account a complementarity relation of core phases $\Delta\Phi_i$ $(i = 1,2,3)$ between neighboring vortices and chiralities, coupled core dynamics at this alignment can be discussed in the same frame with 2 coupled vortices. Three cores rotate uniformly same phase at f_L $(\Delta\Phi_i = 0)$, with finite phase delays $\Delta\Phi_i = \pi/2$ at f_M (Magnetostatic energetically, completely identical with non-coupled vortex), and opposite phase delay $\Delta\Phi_i = \pi$ at f_H. The energy scheme of 3 chained vortices and a phase relation of 3 cores are illustrated in Fig. 6.3.
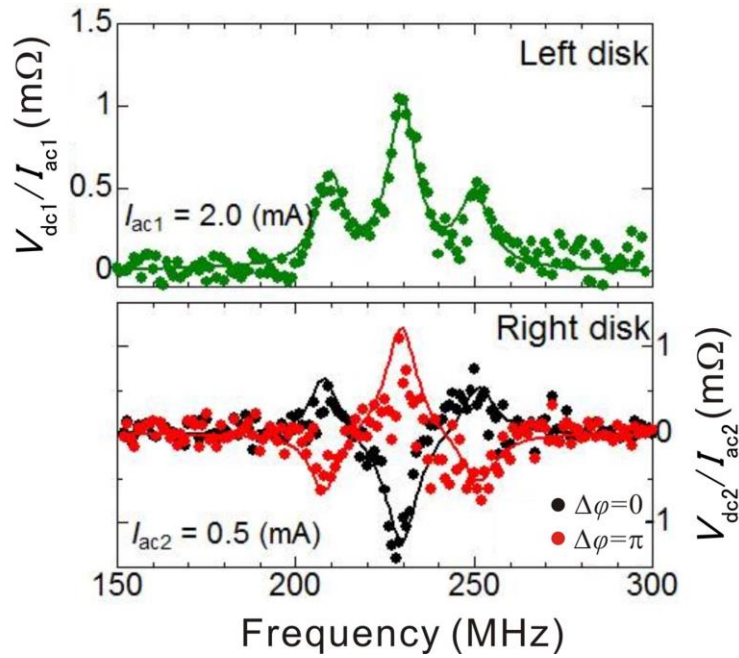
FIG. 6.2: Resonant spectra of 3 chained vortices. (a) The excitation spectra at the vortex 1 and (b) the detection spectra at the vortex 3. Same current phase detection $\Delta\varphi = 0$ and opposite current phase detection are plotted by black and red symbols, showing sign inversion same with Fig. 5.10. Fitting results using Thiele equation are given by solid curves.

Results of 3 chained vortices enable to derive general from of collective spin wave propagation in the 1 dimensionally coupled N vortices. For simplicity, Uniform chiralities $c_i = +1$ and uniform polarities $p_i = +1$ are assumed. The differential of wave number between neighboring vortices Δk_i shall be constant $\Delta k_i = \frac{\Delta\Phi_i}{D} = const. \left(= \Delta k = \frac{\Delta\Phi}{D}\right)$ since the uniform coupling intensity in cases of same shapes of ferromagnets. The minimum of Δk can be $\Delta k_{min} = 0$ (in-phase rotation) and the maximum is $\Delta k_{max} = \frac{\pi}{D}$ since the opposite phase $\Delta\Phi_i = \pi$ is energetically most unstable. Beside, whole phase difference from the left edge to the right edge $(N-1)\Delta\Phi$ should be equal to the integral multiple of the value of π: $(N-1)\Delta\Phi = M\pi$ $(M \in \aleph)$ owning to excitation of the spin

standing wave as collective precession of core dynamics. As a result, a relation of vortex number N and antinode number M is written as

$$0 \leq M \leq N - 1. \tag{6.1}$$
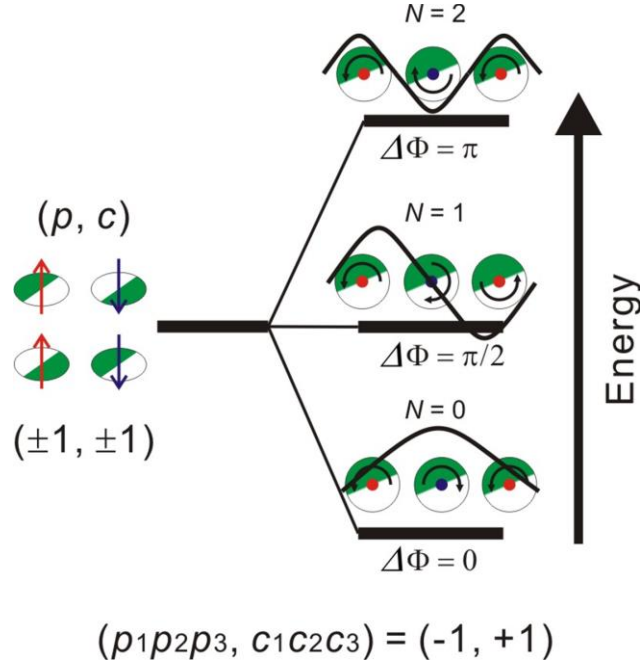
FIG. 6.3: The schematic image of energy scheme of 3 chained vortices with cartoons of a phase relation of 3 cores and the standing spin wave. For simplicity, polarities and chiralities are set to be $(p_1 p_2 p_3, c_1 c_2 c_3) = (-1, +1)$.

In a case of two coupled vortices in the chapter 5, the Eq. 6.1 requires $M = \{0,1\}$ and $\Delta\Phi = \{0, \pi\}$, the former exhibits the excitation of the bonding modes and the latter does the antibonding modes. Apart from chiralities and the phase dependent mode stability, the coupling energy is also tuned by polarities $p_1 p_2 = \pm 1$, thus totally 4 different states are possible. Using the same manner, $M = \{0,1,2\}$ and $\Delta\Phi = \{0, \pi/2, \pi\}$ are required for 3 chained system from Eq. (6.1), as exactly same with experimental results in Fig. 6.3.

Continuous phase tuning result is plotted in Fig.6.4 by means of free excitation. The selective excitations are observed for given parameters of 3 coupled vortices, bonding (f_L) and antibonding (f_H) for $\Delta\varphi = 0$ and intermediate mode (f_M) for $\Delta\varphi = \pi$. The phase differences of cores $\Delta\Phi$ stays constant at intermediate region, just like results of two coupled vortices in Fig. 5.14. The analytical prediction by Eq. (6.1) is plotted in solid white curves. Since coupling energy takes maximum at $\Delta\Phi_i = \pi$ and minimum as $\Delta\Phi_i = 0$, splitting amplitudes in frequency is independent from N. The more vortex number N increases, possible number of nodes M, i.e. possible phase differences $\Delta\Phi = \left\{0, \frac{\pi}{N-1}, \frac{2\pi}{N-1}, ..., \frac{(N-2)\pi}{N-1}, \pi\right\}$ also increases. It results in filling up intermediate region of frequencies ($f_L < f < f_H$) for 1 dimensionally coupled vortices, and forms a finite band width.
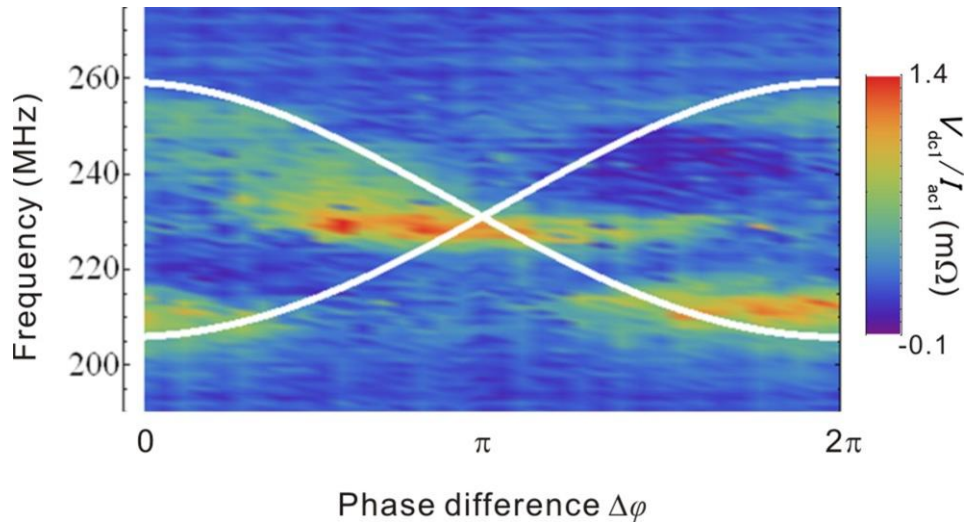
FIG. 6.4: Phase tuning of resonant spectra of 3 chained vortices by means of free excitation, i.e. $I_{ac1} = I_{ac2} = 2.0$ mA. Polarities and chiralities are $(p_1, p_2, p_3) = (+1, -1, +1)$ and $(c_1, c_2, c_3) = (+1, +1, +1)$, respectively. A frequency property of 1 dimensionally coupled vortices is plotted by solid white lines.

6.2. Band structure of 1 dimensionally coupled magnonic crystal

Studies of 3 chained system give insights of finite band structure for1 dimensionally coupled vortices. To discuss 1 dimensional system more precisely, analytical approach of 1 dimensionally coupled vortices reported by Han *et al.*[124] is introduced. The magnetic dipolar energy at the nth vortex $(n = ,1, \dots, N)$ is described as

$$U_{int} = \frac{c_{n-1}c_n}{R^2}\left(\eta_x x_{n-1}x_n - \eta_y y_{n-1}y_n\right) + \frac{c_n c_{n+1}}{R^2}\left(\eta_x x_n x_{n+1} - \eta_y y_n y_{n+1}\right) \tag{6.2}$$

for $n = 2,3, \dots, N-1$. The edge effect $(n = 1, N)$ is neglected here. Here magnetic dipolar interaction only from neighboring two disks is taken into account. For simplicity, the damping process (no current $\boldsymbol{u} = 0$, and no external field $\boldsymbol{H} = 0$) is assumed to obtain the dispersion relation of system. The Thiele equation is rewritten as

$$-p_n G_0 \frac{dy_n}{dt} - \alpha D_0 \frac{dx_n}{dt} + \kappa x_n + \frac{\eta_x c_n}{R^2}(c_{n+1}x_{n+1} + c_{n-1}x_{n-1}) = 0, \tag{6.3}$$

$$p_n G_0 \frac{dx_n}{dt} - \alpha D_0 \frac{dy_n}{dt} + \kappa y_n - \frac{\eta_y c_n}{R^2}(c_{n+1}y_{n+1} + c_{n-1}y_{n-1}) = 0.$$

Here a symmetric form of potential $\kappa_x = \kappa_y = \kappa$ is assumed. A general form of propagation wave is written as

$$\begin{pmatrix} x_n \\ y_n \end{pmatrix} = \begin{pmatrix} X_n e^{i(ka_n - \omega t)} \\ Y_n e^{i(ka_n - \omega t + p_n(\pi/2))} \end{pmatrix} \tag{6.4}$$

Here the position at *n*th core is given by $a_n = nD$. By substituting Eq. 6.4 into Eq. 6.3, simultaneous equations about $\boldsymbol{R} = (X_n, Y_n)$ is obtained as form of $\boldsymbol{R} \cdot A(k, \omega) = 0$. Thus the general form of dispersion relation is written as

$$\omega^2 = {\omega_\gamma}^2(1 + \tilde{\alpha}^2) \tag{6.5}$$

$$\times \left[1 + \frac{i\omega\tilde{\alpha}}{\left(\omega_\gamma(1 + \tilde{\alpha}^2)\right)} + c_n\left(c_{n+1}e^{ikD} + c_{n-1}e^{-ikD}\right)\left(\frac{\eta_x}{\kappa R^2}\right)\right]$$

$$\times \left[1 + \frac{i\omega\tilde{\alpha}}{\left(\omega_\gamma(1 + \tilde{\alpha}^2)\right)} - c_n\left(c_{n+1}p_n p_{n+1}e^{ikD} + c_{n-1}p_n p_{n-1}e^{-ikD}\right)\left(\frac{\eta_y}{\kappa R^2}\right)\right]$$

Eq. 6.5 can be further simplified at the limitation of zero damping $(\tilde{\alpha} = 0)$ and parallel or anti parallel orderings of polarities and chiralities, i.e. $(p_n p_{n+1}, c_n c_{n+1}) = (+1, +1)$. In such cases, ω^2 can be expressed as

$$\omega^2 = \omega_\gamma{}^2 \varsigma_x{}^2 \varsigma_y{}^2 \tag{6.6}$$

with

$$\varsigma_x{}^2 = 1 + 2c_n c_{n+1} \left(\frac{\eta_x}{\kappa R^2}\right) \cos kD \tag{6.7}$$

$$\varsigma_y{}^2 = 1 - 2c_n c_{n+1} p_n p_{n+1} \left(\frac{\eta_y}{\kappa R^2}\right) \cos kD$$

Calculation results in cases of specific 4 types of alignments are shown in Fig. 6.5: Type A for $(p_n p_{n+1}, c_n c_{n+1}) = (+1, +1)$, Type B for $(p_n p_{n+1}, c_n c_{n+1}) = (+1, -1)$, Type C for $(p_n p_{n+1}, c_n c_{n+1}) = (-1, +1)$ and Type D as $(p_n p_{n+1}, c_n c_{n+1}) = (-1, -1)$. Switches of polarities change the interaction energy with neighbouring vortices and change the band width: the uniformly parallel polarities (including Type A and B) result in narrowest widths and fully anti-parallel ones (including Type C and D) cause widest widths here. Besides, Overall shape of band structure is affected by alignment of chiralities. Here the sign of $p_n p_{n+1} c_n c_{n+1}$ is the crucial parameter: the dispersion curve is concave down with $p_n p_{n+1} c_n c_{n+1} = +1$ (Type A or D) while it concave up with $p_n p_{n+1} c_n c_{n+1} = -1$ (Type B or C). For all combinations of (p_n, c_n), group velocity $\partial \omega / \partial k$ takes zero value at Γ and X points. At the former all cores precess uniformly whereas they precess opposite phase and take repulsive alignment at the latter. Therefore, these vortex-based magnonic crustal is certainly a model case where both the directionality of wave propagations and band width are tunable simply by changing polarities and chiralities.
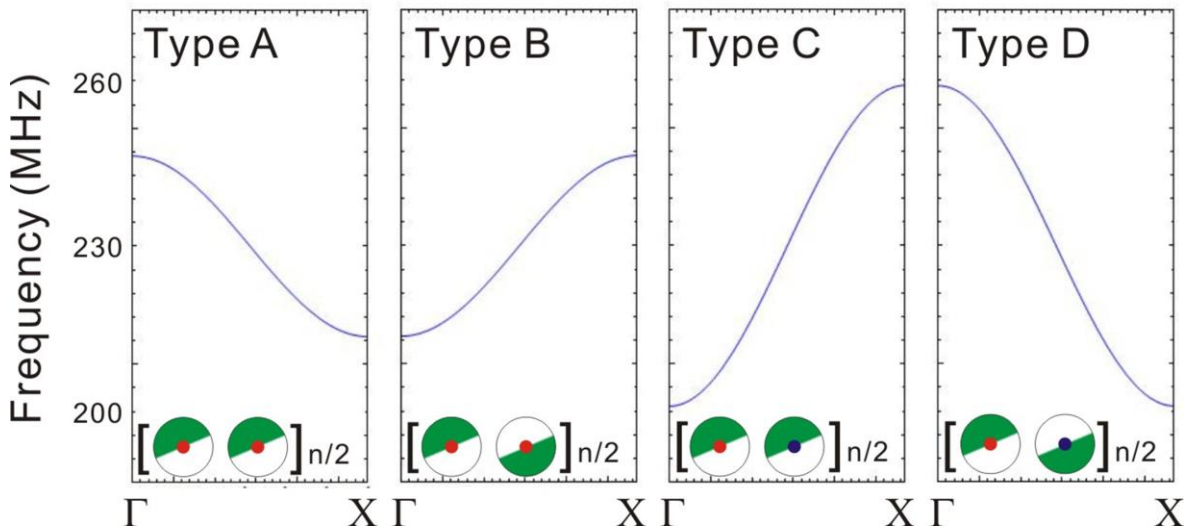

FIG. 6.5: Band structure of 1 dimensionally coupled vortices with 4 types of (p_n, c_n) combinations. A:$(p_n p_{n+1}, c_n c_{n+1}) = (+1, +1)$, B:$(p_n p_{n+1}, c_n c_{n+1}) = (+1, -1)$, C:$(p_n p_{n+1}, c_n c_{n+1}) = (-1, +1)$, and D:$(p_n p_{n+1}, c_n c_{n+1}) = (-1, -1)$.

7.   Conclusion

In this thesis, collective magnetization dynamics of vortex structure interacted by the stray field has been studies, with prospects of forming new type of magnonic crystal via 1- or 2- dimensionally coupled magnetic vortices. Electrical frequency sensor exploiting spin torque diode effect and time resolved-magneto-optic Kerr magnetometer have been employed to access the magnetization dynamics on the nanosecond in time space and micro-meter in real space. The effect of vortex's two independent degrees of freedom as magnetization configuration, polarity and chirality, have been systematically investigated using static imaging technique using magnetic force microscopy and micromagnetic simulations.

Rectified voltage measurements exploiting in-plane anisotropic magnetoresistance (AMR) oscillation enable to observe frequency properties from single vortex structure. Smaller magnetoresistance ratio of AMR compared with giant or tunnel magnetoresistance effect is normally difficult to pick up the small magnetization dynamics at the core region with exchange length scale. As an answer to this problem, symmetry has been intentionally broken and rectified voltage can be enhanced by deflecting vortex core from the very center of symmetric shape of sample, a circular disk in this thesis. Such deflection is usually inserted with external field of sample design. By tuning detection current independent from excitation current, non-distorted core dynamics has been also studied. Both dynamics of non-distorted and intentionally distorted forms show comparable frequency properties within regions of our interests, and their energy scale can be well described by Thiele equation where the core is approximated as a rigid quasiparticle and circularly carling magnetization (chirality) cannot be relaxed at the edge region (rigid vortex model). These studies also indicate adiabatic spin transfer torque is dominant as excitation torque, rather than current induced Oersted field torque under current-induced dynamics. These diode detections are quite conventional way to detect core dynamics sensitively as electrical measurement, and especially suitable for studies of coupled vortices since vortices in single layer ferromagnet is easy to check and switch its remanent state, polarity and chirality configuration. Besides, the time evolution of the vortex core at the energy dissipation process, i.e. damping from the excited position, has been detected by using time resolved magneto-optic Kerr effect (MOKE). This time space measurements can be explained by particle-approximated model in Thiele equation, and shows a consistency with frequency space measurement

Next, as a unit of vortex used magnonic crystal, dynamics of two neighboring vortices has been investigated. Collective magnetization dynamics associated with core gyration at the excitation process results in emergence of strong magnetic dipolar filed at the surface strong enough to excite neighboring vortex structure with sub-micro meter in edge to edge distance. The dipolar field shows linear directionality tuned by selecting polarity and chirality of vortex, and energy scheme of coupled vortices can be affected by tuning these two parameters. As an experimental approach,

current-induced dynamics of coupled vortices has been first studied by means of rectified measurement with small asymmetry in circular disks. The eigenstate of single vortex independent from polarity and chirality splits into 4 distinctive eigenstates in two coupled modes, and each modes can be uniquely labelled by configuration of polarities (parallel or antiparallel), chiralities (same direction or opposite direction) and the phase difference of core precession (in-phase precession of opposite phase precession). Interaction energy scale shows analogy with van der Waals interaction in separate distance dependence. The phase difference of cores is mutually locked depending on the number of coupled vortices. Apart from frequency properties, the damping process of coupled cores has been detected by same means of time resolved-measurement of the single magnetic cortex. Observed damping velocity is independent from the coupling intensity, showing there is no additional energy dissipation process even in magnetostatically coupled system.

The more the coupled number increase, the number of nodes also increase then additional eigenstates can be excited at intermediate levels between bonding and antibonding modes observed in 2 coupled vortices. For 1 dimensionally coupled vortices with infinite length, a finite band width is formed. The band structure of coupled vortices can be tunable by selecting polarities and chiralities. Several examples are calculated, and polarities tune the coupling intensity, i.e. band width and chirality affect the shape of band structure, respectively.

Even though experiments of this thesis were entirely focused on up to only 3 coupled magnetic vortices, several pieces for future prospect.

In this thesis, circular permalloy disks are adopted for vortex confining material, and possible frequency band in coupled vortices are also limited. However, such energy scale can be somehow modulated by engineering; sample design[77] and field tuning[118] even if using a same material. Arrayed vortices with different aspect ratio (thickness/radius) varied eigenfrequencies from MHz up to GHz in the frequency band only by shape engineering, and band gaps can be formed between slower core gyrating modes (small aspect ratio) and faster gyrating modes (large aspect ratio)[125]. In these ways, a fine tunablity only by changing parameters property make coupled vortices as a possible candidate for future spintronics devices.

The observed vortex gyration propagation endurance will be also convenient for extension of coupled systems. One can replace lower damping material instead of permalloy in this these to obtain higher propagation efficiency, such as NiMnSb with $\alpha \sim 0.002$[126] or some Heusler alloys with extremely low damping constant[127,128].

In terms of more applicational area, mutual phase locking observed by means of free excitation alignment may be an answer for developing the quality factor of vortex used dc spin torque nano oscillator[11], which has been attracting attentions for high power active oscillator[129]. Our results only observed the phase coordination at linear region thus an experimental report using spin torque oscillator with magnetostatically coupled vortices as a free layer shall be further required.

Publication list

[p1] <u>S. Sugimoto</u>, Y. Fukuma, S. Kasai, T. Kimura, A, Barman, and Y. Otani. *Dynamics of coupled vortices in a pair of ferromagnetic disks.* Phys. Rev. Lett. **106**, 197203 (2011).

[p2] <u>S. Sugimoto,</u> Y. Fukuma, and Y. Otani, *Manipulation of the excitation state of the coupled vortices in a pair of magnetic disks. IEEE Trans.* Magn. **47**, 2951 (2011).

[p3] B. Rana, D. Kumar, S. Barman, S. Pal, R. Mandal, Y. Fukuma, Y. Otani, <u>S. Sugimoto</u>, and A. Barman. *Anisotropy in collective precessional dynamics in arrays of $Ni_{80}Fe_{20}$ nanoelements.* J. Appl. Phys. **111**, 07D503 (2012).

[p4] S. Saha, R. Mandal, S. Barman, D, Kumar, B. Rana, Y. Fukuma, <u>S. Sugimoto</u>, Y. Otani, and A. Barman. *Tunable magnonic spectra in two-dimensional magnonic crystals with variable lattice symmetry.* Adv. Funct. Mater. **23**, 2378 (2013).

[p5] <u>S. Sugimoto</u>, N. Hasegawa, Y. Niimi, Y. Fukuma, S. Kasai, and Y. Otani. *Detection of a Symmetric Circular Gyration of the Vortex Core via the Second Order Harmonic Magnetoresistance Oscillation.* Appl. Phys. Express **7**, 023006 (2014).

Report

RIKEN RESEARCH, Sep. 2011. *Rotation of paired magnetic vortices.* <u>S. Sugimoto</u>, A. Barman, T. Kimura, K. Shinya F. Fukuma, and Y. Otani.

Conference contributions

International conference

[p6] <u>S. Sugimoto</u>, Y. Fukuma, S. Kasai, and Y. Otani. *Coupled vortex dynamics in Permalloy submicron disk pairs* (oral, invited). International Conference of AUMS (ICAUMS2010), Jeju Island, Korea, December 2010.

[p7] <u>S. Sugimoto</u>, Y. Fukuma, and Y. Otani. *Current excitation of translational modes in magnetostatically coupled magnetic vortices* (poster). IEEE 7th International Symposium on Metallic Multilayers (MML2010), Berkeley, USA, September 2010.

[p8] <u>S. Sugimoto</u>, Y. Fukuma, and Y. Otani. *Dynamics of coupled magnetic vortices via magnetic dipolar interaction* (oral). InterMag 2011, Taipei, Taiwan, April 2011.

[p9] <u>S. Sugimoto</u>, Y. Fukuma, H. Fujimori, Y. Niimi, and Y. Otani. *The current induced nonlinear mode splitting of the magnetic vortex* (oral). International
Conference of the Asian Union of Magnetics Societies (ICAUMS), Nara, Japan, October 2012.

[p10] <u>S. Sugimoto</u>, Y. Fukuma, H. Fujimori, Y. Niimi, and Y. Otani. *Study of the nonlinear effect in current induced core oscillations of a single magnetic vortex* (poster). The 21th International
Colloquium on Magnetic Films and Surfaces (ICMFS), Shanghai, China, September 2012.

[p11] <u>S. Sugimoto</u>, H. Fujimori, Y. Niimi, Y. Fukuma, S. Kasai, and Y. Otani. *Controlled excitation of the collective dynamics in coupled magnetic vortices* (oral). The 12th Joint MMM/Intermag
Conference, Chicago, USA, January 2013.

[p12] <u>S. Sugimoto</u>, N. Hasegawa, Y. Niimi, Y. Fukuma, and Y. Otani. *The development of the non-perturbing electrical detection method of the sole vortex gyration* (poster). The 8th International
Symposium on Metallic Multilayers (MML2013), Kyoto, Japan, May 2013.

Domestic conference (JPN)

[p13] <u>S. Sugimoto</u>, Y. Fukuma, and Y. Otani. *Spin dynamics of the magnetostatically coupled magnetic vortices* (poster). The Physical Society of Japan (JPS) 2009 Fall Meetings, Kumamoto, Japan, Sep. 2009.

[p14] <u>S. Sugimoto</u>, Y. Fukuma, and Y. Otani. *Detection of current-induced dynamics of low frequency mode in paired magnetic vortices* (oral). JPS 2010 65th Annual Meeting, Okayama, Japan, Mar. 2010.

[p15] <u>S. Sugimoto</u>, Y. Fukuma, and Y. Otani. *Splitting of the low frequency mode in magnetostgatically coupled neighboring vortices* (poster). Conference in specific region "Generation and Manipulation of Spin Current", Kyoto, Japan, June 2010.

[p16] <u>S. Sugimoto</u>, Y. Fukuma, S. Kasai and Y. Otani. *The effect of magnetic dipolar interaction in spin dynamics of vortices* (oral). The 35th Annual Conference on Magnetics in Japan , Niigata, Japan, Sep. 2011.

[p17] <u>S. Sugimoto</u>, Y. Fukuma, S. Kasai and Y. Otani. *Collective dynamics of vortex cores in the two-dimensional array of magnetic vortices* (oral). JPS 2011 Fall Meetings, Toyama, Japan, Sep. 2011.

[p18] <u>S. Sugimoto</u>, Y. Fukuma, and Y. Otani. *Spin dynamics of the one-dimensional chain of magnetic vortices* (oral). JPS 2011 66th Annual Meeting, Niigata, Japan, Mar. 2011.

[p19] <u>S. Sugimoto</u>, Y. Fukuma, and Y. Otani. *Time domain measurement of magnetostatically coupled array of magnetic vortices* (oral). JPS 2012 67th Annual Meeting, Osaka, Japan, Mar. 2012.

[p20] <u>S. Sugimoto</u>, H. Fujimori, N, Hasegawa, Y. Niimi, Y. Fukuma, and Y. Otani. *Electrical operation of collective modes excited in magnetostatically coupled paired vortices* (oral). JPS 2013 68th Annual Meeting, Hiroshima, Japan, Mar. 2013.

Appendix

A. Process parameters

Permalloy nanodisks

Step	Process	Product/Machine	Parameters
1.1	Spin coat	MMA EL9	1500 rpm, 90 s
	Bake	Hotplate	180 °C, 90 s
1.2	Spin coat	PMMA 950K A4	5000 rpm, 40s
	Bake	Hotplate	180 °C, 90 s
1.3	Spin coat	Espacer	3000 rpm, 30s
2	e- beam lithography	Elionix 7700	100 kV, 100 pA 4.0 μCcm^{-2} Step size 2.5 nm
3.1	Rinse for 1.3	Water	60 s
3.2	Develop for 1.1, 1.2	1:3 MIBK to IPA	30 s
3.3	Rinse for 1.1, 1.2	Isopropanol	60 s
4	e-beam evaporation	UHV chamber	30 nm – 50 nm Ni$_{80}$Fe$_{20}$ $0.7 – 2.0 \times 10^{-7}$ Torr
5	Lift-off	Acetone	4 – 12 h
6	clean	Isopropanol	Ultrasonic cleaning

Contact pads (e-beam lithography)

Step	Process	Product/Machine	Parameters
1	Spin coat	MMA EL9	1500 rpm, 90 s
	Bake	Hotplate	180 °C, 90 s
2	e- beam lithography	Elionix 7700	100 kV, 500 pA 4.0 μCcm^{-2} Step size 2.5 nm
3.1	Develop	1:3 MIBK to IPA	30 s
3.2	Rinse	isopropanol	60 s
5	Thermal evaporation	UHV chamber	50 nm – 150 nm Cu $1.0 – 3.0 \times 10^{-6}$ Torr
6	Lift-off	Acetone	8 – 18 h
7	clean	Isopropanol	Ultrasonic cleaning

Striplines, and coplanar waveguide (photolithography)

Step	Process	Product/Machine	Parameters
1.1	Spin coat	Promoter	4000 rpm, 40s
	Bake	Oven	80 °C, 300 s
1.2	Spin coat	AZ 1500	4000 rpm, 40s
	Bake	Oven	80 °C, 600 s
2	Photo beam lithography	D-light DL-1000RS	Step size 1.0 μm 100 mJ/cm^2
3.1	Develop	1:1 AZ Developer to Water	90 s
3.2	Rinse	Water	120 s
4	Thermal evaporation	UHV chamber	5 nm Ti 50 nm – 100 nm Cu 50 nm – 150 nm Au $1.0 – 3.0 \times 10^{-6}$ Torr
6	Lift-off	Acetone	8 – 18 h
7	clean	Isopropanol	Rinse

Insulator (photolithography)

Step	Process	Product/Machine	Parameters
1.1	Spin coat	Promoter	4000 rpm, 40s
	Bake	Oven	80 °C, 300 s
1.2	Spin coat	AZ 1500	4000 rpm, 40s
	Bake	Oven	80 °C, 600 s
2	Photo beam lithography	D-light DL-1000RS	Step size 1.0 μm 100 mJ/cm^2
3.1	Develop	1:1 AZ Developer to Water	90 s
3.2	Rinse	Water	120 s
4	Rf-magnetron sputtering	SHINKO SEIKI STV4321	50 nm Al_2O_3 200 W $1.0 – 3.0 \times 10^{-6}$ Torr
6	Lift-off	Acetone	8 – 18 h
7	clean	Isopropanol	Rinse

B. Current calibration

Fig. B (b) shows diagram of set up to measure the return loss. A sample is connected to the input side of the directional bridge and the excitation voltage V_1^+ is injected from output side, and leak voltage V_3 is measured. The reflectance factor of sample Γ is written as

$$\Gamma = \frac{V_2}{V_1} = \frac{Z - Z_0}{Z + Z_0} = \frac{V_2^-}{V_2^+} = \frac{V_3}{V_2^+} \times 10^{+16/20}. \qquad (B.1)$$

Here V_3 is directly measurable and V_2^+ can be estimated usual set up in Fig. B (a). Therefore reflectance factor Γ is calculated. Subsequently impedance of sample $Z = Z_0(1 + \Gamma)/(1 - \Gamma)$ is obtained and corrected current flowing in sample $I(t)$ is calculated from injected voltage V_2^+ as

$$I(t) = \frac{2Z}{Z + Z_0} V_2^+. \qquad (B.2)$$

Values of Z of all samples for current excitation typically lie in $130 \sim 150 \ \Omega$ in chapter 4-6.
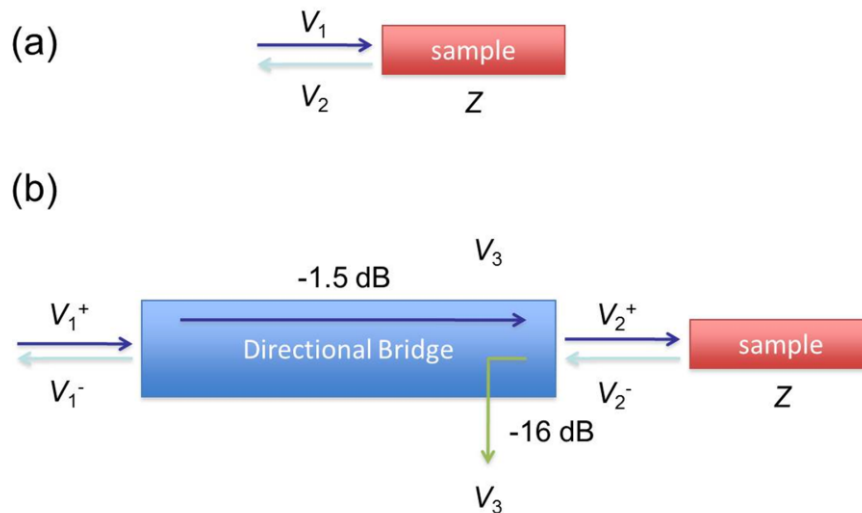

FIG. B: Diagram of (a) usual and (b) correction circuit to estimate return loss of ac current.

Bibliography

[1] T. Ritz, S. Adem, and K. Schulten. *A model for photoreceptor-based magnetoreception in birds.* Biophys. J. **78**,

[2] M. Lewin, N. Carlesso, C.-H. Tung, X.-W. Tang, D. Cory, D. T. Scadden, and R. Weissleder. *Tat peptide-derivatized magnetic nanoparticles allow in vivo tracking and recovery of progenitor cells.* Nat. Biotech. **18**, 410 (2000).

[3] Q. A. Pankhurst, J. Connolly, S. K. Jones, and J. Dobson. *Applications of magnetic nanoparticles in biomedicine.* J. Phys. D: Appl. Phys. **36**, R167 (2003).

[4] J.-H. Lee, Y.-M. Huh, Y.-W. Jun, J.-W. Seo, J.-T. Jang, H.-T. Song, S. Kim, E.-J. Cho, H.-G. Yoon, J.-S. Suh, and J. Cheon. *Artificially engineered magnetic nanoparticles for ultra-sensitive molecular imaging.* Nat. Med. **13**, 95 (2007).

[5] B. N. Engel, J. Åkerman, B. Butcher, R. W. Dave, M. DeHerrera, M. Durlam, G. Grynkewich, J. Janesky, S. V. Pietambaram, N. D. Rizzo, J. M. Slaughter, K. Smith, J. J. Sun, and S. Tehrani. *A 4-Mb toggle MRAM based on a novel bit and switching method.* IEEE Trans. Magn. **41**, 132 (2005).

[6] S. S. P. Parkin, M. Hayashi, and L. Thomas. *Magnetic Domain-Wall Racetrack Memory.* Science **320**, 190 (2008).

[7] V. V. Kruglyak, S. O. Demokritov, and D. Grundler. *Magnonics.* J. Phys. D: Appl. Phys. **43**, 264001 (2010).

[8] S. Barman, A. Barman, & Y. Otani. *Controlled propagation of locally excited vortex dynamics in linear nanomagnet arrays.* J. Phys. D: Appl. Phys. **43**, 335001 (2010).

[9] D. A. Allwood, G. Xiong, M. D. Cooke, C. C. Faulkner, D. Atkinson, N. Vernier, and R. P. Cowburn. *Submicrometer ferromagnetic NOT gate and shift register.* Science **296**, 2003 (2002).

[10] A. Imre, G. Csaba, L. Ji, A. Orlov, G. H. Bernstein, and W. Porod. *Majority Logic Gate for Magnetic Quantum-Dot Cellular Automata.* Science **311**, 205 (2006).

[11] V. S. Pribiag, I. N. Krivorotov, G. D. Fuchs, P. M. Braganca, O. Ozatay, J. C. Sankey, D. C. Ralph, and R. A. Buhrman. *Magnetic vortex oscillator driven d.c. spin-polarized current.* Nat. Phys. **3**, 498 (2007).

[12] Q. Mistral, M. van Kampen, G. Hrkac, Joo-Von Kim, T. Devolder, P. Crozat, C. Chappert, L. Lagae, and T. Schrefl. *Current-Driven Vortex Oscillations in Metallic Nanocontacts.* Phys. Rev. Lett. **100**, 257201 (2008).

[13] T. Shinjo, T. Okuno, R. Hassdorf, K. Shigeto, and T. Ono. *Magnetic Vortex Core Observation in Circular Dots of Permalloy.* Science **289**, 930 (2000).

[14] A. Wachowiak, J. Wiebe, M. Bode, O. Pietzsch, M. Morgenstern, and R. Wiesendanger. *Direct Observation of Internal Spin Structure of Magnetic Vortex Cores.* Science **298**, 577 (2002).

[15] S.-B. Choe, Y. Acremann, A. Scholl, A. Bauer, A. Doran, J. Stöhr, and H. A. Padmore. *Vortex Core-Driven Magnetization Dynamics.* Science **304**, 420 (2004).

[16] V. Novosad, F. Y. Fradin, P.E. Roy, K. S. Buchanan, K. Yu. Guslienko, and S. D. Bader. *Magnetic vortex resonance in patterned ferromagnetic dots.* Phys. Rev. B **72**, 024455 (2005).

[17] S. Bohlens, B. Krüger, A. Drews, M. Bolte, G. Meier, and D. Pfannkuche. *Current controlled random-access memory based on magnetic vortex handedness.* Appl. Phys. Lett. **93**, 142508 (2008).

[18] K. Nakano, D. Chiba, N. Ohshima, S. Kasai, T. Sato, Y. Nakatani, K. Sekiguchi, K. Kobayashi, and T. Ono. *All-electrical operation of magnetic vortex core memory cell.* Appl. Phys. Lett. **99**, 262505 (2011).

[19] K. Tanabe, D. Chiba, J. Ohe, S. Kasai, H. Kohno, S. E. Barnes, S. Maekawa, K. Kobayashi, and T. Ono. *Spin-motive force due to a gyrating magnetic vortex.* Nat. Commun. **3**, 845 (2012).

[20] B. Pigeau, G. de Loubens, O. Klein, A. Riegler, F. Lochner, G. Schmidt, L. W. Molenkamp, V. S. Tiberkevich, and A. N. Slavin. *A frequency-controlled magnetic vortex memory.* Appl. Phys. Lett. **96**, 132506 (2010).

[21] J. Shibata, K. Shigeto, and Y. Otani. *Dynamics of magnetostatically coupled vortices in magnetic nanodisks.* Phys. Rev. B **67**, 224404 (2003).

[22] J. Shibata, and Y. Otani. *Magnetic vortex dynamics in a two-dimensional square lattice of ferromagnetic nanodisks.* Phys. Rev. B **70**, 012404 (2004).

[23] Y. A. Galkin, B. A. Ivanov, and C. E. Zaspel. *Collective modes for an array of magnetic dots in the vortex state.* Phys. Rev. B **74,** 144419 (2006).

[24] S. A. Nikitov, Ph. Tailhades, and C.S. Tsai. *Spin waves in periodic magnetic structures - magnonic crystals.* J. Magn. Magn. Mater. **236**, 320 (2001).

[25] G. Gubbiotti, S. Tacchi, G. Carlotti, N. Singh, S. Goolaup, A. O. Adeyeye, and M. Kostylev. *Collective spin modes in monodimensional magnonic crystals consisting of dipolarly coupled nanowires.* Appl. Phys. Lett. **90**, 092503 (2007).

[26] J. Topp, D. Heitmann, M. P. Kostylev, and D. Grundler. *Making a Reconfigurable Artificial Crystal by Ordering Bistable Magnetic Nanowires.* Phys. Rev. Lett. **104**, 207205 (2010).

[27] K.-S. Lee, D.-S. Han, and S.-K. Kim. *Physical Origin and Generic Control of Magnonic Band Gaps of Dipole-Exchange Spin Waves in Width-Modulated Nanostrip Waveguides.* Phys. Rev. Lett. **102**, 127202 (2009).

[28] A. A. Tulapurkar, Y. Suzuki, A. Fukushima, H. Kubota, H. Maehara, K. Tsunekawa, D. D. Djayaprawira, N. Watanabe, and S. Yuasa. *Spin-torque diode effect in magnetic tunnel junctions.* Nature **438**, 339 (2005).

[29] J. C. Sankey, P. M. Braganca, A. G. F. Garcia, I. N. Krivorotov, R. A. Buhrman, and D. C. Ralph. *Spin-Transfer-Driven Ferromagnetic Resonance of Individual Nanomagnets.* Phys. Rev. Lett. **96**, 227601 (2006).

[30] J. Kerr. *On rotation of the plane of light from the equatorial surface of a magnet.* Philos. Mag. **5**, 161 (1878).

[31] K. Y. Guslienko, V. Novosad, Y. Otani, H. Shima, and K. Fukamichi. *Magnetization reversal due to vortex nucleation, displacement, and annihilation in submicron ferromagnetic dot arrays.* Phys. Rev. B **65**, 024414 (2001).

[32] W. Heisenberg. *Zur Theorie des Ferromagnetismus.* Z. Phys. **49**, 619 (1928).

[33] G. Nahrwold, J. M. Scholtyssek, S. Motl-Ziegler, O. Albrecht, U. Merkt, and G. Meier. *Structural, magnetic, and transport properties of permalloy for spintronic experiments.* J. Appl. Phys. 108, 013907 (2010).

[34] J. Fassbender, T. Strache, M. O. Liedke, D. Marko, S. Wintz, K. Lenz, A. Keller, S. Facsko, I. Mönch, and J . McCord. *Introducing artificial length scales to tailor magnetic properties.* New J. Phys. **11**, 125002 (2009).

[35] S. Lepadatu, J. S. Claydon, C. J. Kinane, T. R. Charlton, S. Langridge, A. Potenza, S. S. Dhesi, P. S. Keatley, R. J. Hicken, B. J. Hickey, and C. H. Marrows. *Domain-wall pinning, nonadiabatic spin-transfer torque, and spincurrent polarization in permalloy wires doped with vanadium.* Phys. Rev. B **81**, 020413 (2010).

[36] L. F. Yin, D. H. Wei, N. Lei, L. H. Zhou, C. S. Tian, G. S. Dong, X. F. Jin, L. P. Guo, Q. J. Jia, and R. Q.Wu. *Magnetocrystalline Anisotropy in Permalloy Revisited.* Phys. Rev. Lett. **97**, 067203 (2006).

[37] L. W. McKeehan & P. P. Cioffi. *Magnetostriction in Permalloy.* Phys. Rev. **28**, 146 (1926).

[38] W. F. Brown. *Micromagnetics.* Krieger, Huntingdon N. Y., 1978.

[39] A. Hubert & R. Schäfer. *Magnetic Domains.* Springer Verlag Berlin, 1998.

[40] C. Castelnovo, R. Moessner, and S. L. Sondhi. *Magnetic monopoles in spin ice.* Nature (London) **451**, 42 (2008).

[41] B. A. Lilley. *Energies and widths of domain boundaries in ferromagnetics.* Philos. Mag. **41**, 792 (1950).

[42] L. D. Landau and E. Lifshitz. *On the theory of the dispersion of magnetic permeability in ferromagnetic bodies.* Phys. Z. Sowjetunion **8**, 153 (1935).

[43] T. Gilbert, A. Found, and I. Chicago. *A phenomenological theory of damping in ferromagnetic materials.* IEEE Trans. Magn. **40**, 3443 (2004).

[44] W. K. Hiebert, A. Stankiewicz, and M. R. Freeman. *Direct Observation of Magnetic Relaxation in a Small Permalloy Disk by Time-Resolved Scanning Kerr Microscopy.* Phys. Rev. Lett. **79**, 1134 (1997).

[45] C. Kittel. *On the Theory of Ferromagnetic Resonance Absorption.* Phys. Rev. **73**, 155 (1948).

[46] L. Berger. *Low-field magnetoresistance and domain drag in ferromagnets.* J. Appl. Phys. **49**, 2156 (1978).

[47] L. Berger. *Emission of spin waves by a magnetic multilayer traversed by a current.* Phys. Rev. B **54**, 9353 (1996).

[48] J. C. Slonczewski. *Current-driven excitation of magnetic multilayers.* J. Magn. Magn. Mat. **159**, L1 (1996).

[49] M. Tsoi, A. G. M. Jansen, J. Bass, W.-C. Chiang, M. Seck, V. Tsoi, and P. Wyder. *Excitation of a Magnetic Multilayer by an Electric Current.* Phys. Rev. Lett. **80**, 4281 (1998).

[50] E. B. Myers, D. C. Ralph, J. A. Katine, R. N. Louie, and R. A. Buhrman. *Current-Induced Switching of Domains in Magnetic Multilayers Devices.* Science **285**, 867 (1999).

[51] J. A. Katine, F. J. Albert, and R. A. Buhrman. *Current-Driven Magnetization Reversal and Spin-Wave Excitations in Co /Cu / Co Pillars.* Phys. Rev. Lett. **84**, 3149 (2000).

[52] F. J. Albert J. A. Katine, R. A. Burman and D. C. Ralph. *Spin-polarized current switching of a Co thin film nanomagnet.* Appl. Phys. Lett. **77**, 3809 (2000).

[53] S. I. Kiselef, J. C. Sankey, I. N. Krivorotov, N. C. Emley, R. J. Schoelkopf, R. A. Buhrman, and D. C. Ralph. *Microwave oscillations of a nanomagnet driven by a spin-polarized current.* Nature **425**, 380 (2003).

[54] F. J. Albert N. C. Emley, E. B. Myers, D. C. Ralph and R. A. Buhrman. *Quantitative Study of Magnetization Reversal by Spin-Polarized Current in Magnetic Multilayer Nanopillars.* Phys. Rev. Lett. **89**, 226802 (2002).

[55] J. C. Slonczewski. *Currents, torques, and polarization factors in magnetic tunnel junctions.* Phys. Rev. B **71**, 024411 (2005).

[56] A. Yamaguchi, T. Ono, S. Nasu, K. Miyake, K. Mibu, and T. Shinjo. *Real-Space observation of Current-Driven Domain Wall Motion in Submicron Magnetic Wires.* Phys. Rev. Lett. **92**, 077205 (2004).

[57] G. Tatara, and H. Kohno. *Theory of Current-Driven Domain Wall Motion: Spin Transfer versus Momentum Transfer.* Phys. Rev. Lett. **92**, 086601 (2004).

[58] M. Hayashi, L. Thomas, C. Rettner, R. Moriya, Y. B. Bazaliy, and S. S. P. Parkin. *Current Driven Domain Wall Velocities Exceeding the Spin Angular Momentum Transfer Rate in Permalloy.* Phys. Rev. Lett. **98**, 037204 (2007).

[59] T. Koyama, D. Chiba1, K. Ueda1, K. Kondou, H. Tanigawa, S. Fukami, T. Suzuki, N. Ohshima, N. Ishiwata, Y. Nakatani, K. Kobayashi and T. Ono *Observation of the intrinsic pinning of a magnetic domain wall in a ferromagnetic nanowire.* Nat. Mater. **10**, 194 (2011).

[60] S. Zhang and Z. Li. *Roles of Nonequilibrium Conduction Electrons on the Magnetization Dynamics of Ferromagnets.* Phys. Rev. Lett. **93**, 127204 (2004).

[61] H. Kohno, G. Tatara, and J. Shibata. *Microscopic Calculation of Spin Torques in Disordered Ferromagnets.* J. Phys. Soc. Jpn. **75**, 113706 (2006).

[62] G. Tatara, H. Kohno, J. Shibata, Y. Lemaho, and K.-J. Lee. *Spin Torque and Force due to Current for General Spin Textures.* J. Phys. Soc. Jpn. **76**, 054707 (2007).

[63] M. Hayashi, L. Thomas, Ya. B. Bazaliy, C. Rettner, R. Moriya, X. Jiang, and S. S. P. Parkin. *Influence of Current on Field-Driven Domain Wall Motion in Permalloy Nanowires from Time Resolved Measurements of Anisotropic Magnetoresistance.* Phys. Rev. Lett. **96**, 197207 (2006).

[64] G. Meier M. Bolte, and R. Eiselt. *Direct Imaging of Stochastic Domain-Wall Motion Driven by Nanosecond Current Pulses.* Phys. Rev. Lett. **98**, 187202 (2007).

[65] L. Heyne, M. Kläui, D. Backes, T. A. Moore, S. Krzyk, U. Rüdiger, L. J. Heyderman, A. F. Rodríguez, F. Nolting, T. O. Mentes, M. Á. Niño, A. Locatelli, K. Kirsch, and R. Mattheis. *Relationship between Nonadiabaticity and Damping in Permalloy Studied by Current Induced Spin Structure Transformations.* Phys. Rev. Lett. **100**, 066603 (2008).

[66] L. Thomas, M. Hayashi, X. jiang, R. Moriya, C. Rettner, and S. S. P. Parkin. *Oscillatory dependence of current-driven magnetic domain wall motion on current pulse length.* Nature (London) **443**, 197 (2006).

[67] B. Krgüer, M. Najafi, S. Bohlens, R. Frömter, D. P. F. Möller, and D. Pfannkuche. *Proposal of a Robust Measurement Scheme for the Nonadiabatic Spin Torque Using the Displacement of Magnetic Vortices.* Phys. Rev. Lett. **104**, 077201 (2010).

[68] M. Bolte, G. Meier, B. Krüger, A. Drews, R. Eiselt, L. Bocklage, S. Bohlens, T. Tyliszczak, A. Vansteenkiste, B. V. Waeyenberge, K. W. Chou, A. Puzic, and H. Stoll. *Time-Resolved X-Ray Microscopy of Spin-Torque-Induced Magnetic Vortex Gyration.* Phys. Rev. Lett. **100**, 176601 (2008).

[69] L. Heyne, J. Rhensius, D. Ilgaz, A. Bisig, U. Rüdiger, and M. Kläui, L. Joly, F. Nolting, L. J. Heyderman, J. U. Thiele, and F. Kronast. *Direct Determination of Large Spin-Torque Nonadiabaticity in Vortex Core Dynamics.* Phys. Rev. Lett. **105**, 187203 (2010).

[70] S. D. Pollard, L. Huang, K. S. Buchanan, D. A. Arena, and Y. Zhu. *Direct dynamic imaging of non-adiabatic spin torque effects.* Nat. Commun. **3**, 1028 (2012).

[71] N. F. Mott. *The Electrical Conductivity of Transition Metals.* Proc. R. Soc. Lond. A **153**, 699 (1936).

[72] T. R. McGuire and R. I. Potter. *Anisotropic Magnetoresistance in Ferromagnetic 3d Alloys*. IEEE Trans. Magn. **11**, 1018 (1975).

[73] I. Dzyaloshinsky. *A thermodynamic theory of "weak" ferromagnetism of antiferromagnetics*. J. Phys. Chem. Sol. **4**, 241 (1958).

[74] T. Moriya. *Anisotropic Superexchange Interaction and Weak Ferromagnetism*. Phys. Rev. **120**, 91 (1960).

[75] W. Scholz, K. Yu. Guslienko, V. Novosad, D. Suess, T. Schrefl, R. W. Chantrell, and J. Fidler. *Transition from single-domain to vortex state in soft magnetic cylindrical nanodots*. J. Magn. Magn. Mater. **266**, 155 (2003).

[76] M. Goto, H. Hata, A. Yamaguchi, Y. Nakatani, T. Yamaoka, Y. Nozaki, and H. Miyajima. *Electric spectroscopy of vortex states and dynamics in magnetic disks*. Phys. Rev. B **84**, 064406 (2011).

[77] K. Yu. Guslienko, B. A. Ivanov, V. Novosad, Y. Otani, H. Shima, and K. Fukamichi. *Eigenfrequencies of vortex state excitations in magnetic submicron-size disks*. J. Appl. Phys. **91**, 8037 (2002).

[78] A. A. Thiele. *Steady-State Motion of Magnetic Domains*. Phys. Rev. Lett. **30**, 230 (1973).

[79] D. L. Huber. *Dynamics of spin vortices in two-dimensional planar magnets*. Phys. Rev. B **26**, 3758 (1982).

[80] J. Shibata, Y. Nakatani, G. Tatara, H. Kohno, and Y. Otani. *Current-induced magnetic vortex motion by spin-transfer torque*. Phys. Rev. B **73**, 020403 (2006).

[81] J. He, Z. Li, and S. Zhang. *Current-driven vortex domain wall dynamics by micromagnetic simulations*. Phys. Rev. B **73**, 184408 (2006).

[82] B. Krüger, A. Drews, M. Bolte, U. Merkt, D. Pfannkuche, and G. Meier. *Harmonic oscillator model for current- andfield-driven magnetic vortices*. Phys. Rev. B **76**, 224426 (2007).

[83] B. Krüger, A. Drews, M. Bolte, U. Merkt, D. Pfannkuche, and G. Meier. *Vortices and antivortices as harmonic oscillators*. J. Appl. Phys. **103**, 07A501 (2008).

[84] K. Yu. Guslienko. *Low-frequency vortex dynamic susceptibility and relaxation in mesoscopic ferromagnetic dots*. Appl. Phys. Lett. **89**, 022510 (2006).

[85] T. Kamionka, M. Martens, K.W. Chou, M. Curcic, A. Drews, G. Schütz, T. Tyliszczak, H. Stoll, B.V. Waeyenberge, and Guido Meier. *Magnetic Antivortex-Core Reversal by Circular-Rotational Spin Currents*. Phys. Rev. Lett. **105**, 137204 (2010).

[86] D. Bedau, M. Kläui, S. Krzyk, and U. Rüdiger. *Detection of Current-Induced Resonance of Geometrically Confined Domain Walls*. Phys. Rev. Lett. **99**, 146601 (2007).

[87] S. Kasai, Y. Nakatani, K. Kobayashi, H. Kohno, and T. Ono. *Current-Driven Resonant Excitation of Magnetic Vortices*. Phys. Rev. Lett. **97**, 107204 (2006).

[88] R. Moriya, L. Thomas, M. Hayashi, Y. B. Bazaliy, C. Rettner, and S. S. P. Parkin. *Probing vortex-core dynamics using current-induced resonant excitation of a trapped domain wall*. Nat. Phys. **4**, 368 (2008).

[89] V. Novosad, K. Yu. Guslienko, H. Shima, Y. Otani, S. G. Kim, K. Fukamichi, N. Kikuchi, O. Kitakami, and Y. Shimada. *Effect of interdot magnetostatic interaction on magnetization reversal in circular dot arrays*. Phys. Rev. B **65**, 060402 (2002).

[90] M. Bolte, R. Eiselt, G. Meier, D.-J. Kim, and P. Fischer. *Real space observation of dipolar interaction in arrays of Fe microelements*. J. Appl. Phys. **99**, 08H301 (2006).

[91] G. Gubbiotti, M. Madami, S. Tacchi, G. Carlotti, and T. Okuno. *Normal mode splitting in interacting arrays of cylindrical permalloy dots.* J. Appl. Phys. **99**, 08C701 (2006).

[92] E. Yablonovitch. *Inhibited Spontaneous Emission in Solid-State Physics and Electronics.* Phys. Rev. Lett. **58**, 2059 (1987).

[93] R. L. Carter, J. M. Owens, C. V. Smith Jr., and K. W. Reed. *Ionimplanted magnetostatic wave reflective array filters.* J. Appl. Phys. **53**, 2655 (1982).

[94] Y. Au , M. Dvornik , O. Dmytriiev , V. V. Kruglyak. *Nanoscale spin wave valve and phase shifter.* Appl. Phys. Lett. **100**, 172408 (2012).

[95] D. S. Deng, X. F. Jin, and R. Tao. *Magnon energy gap in a periodic anisotropic magnetic superlattice.* Phys. Rev. B **66**, 104435 (2002).

[96] M. P. Kostylev, A. A. Stashkevich, and N. A. Sergeeva. *Collective magnetostatic modes on a one-dimensional array of ferromagnetic stripes.* Phys. Rev. B **69**, 064408 (2004).

[97] J. O. Vasseur, L. Dobrzynski, B. D.-Rouhani, and H. Puszkarski. *Magnon band structure of periodic composites.* Phys. Rev. B **54**, 1043 (1996).

[98] M. Krawczyk, and H. Puszkarski. *Plane-wave theory of three-dimensional magnonic crystals.* Phys. Rev. B **77**, 054437 (2008).

[99] G. N. Kakazei , Yu. G. Pogorelov , M. D. Costa , T. Mewes , P. E. Wigen , P. C. Hammel , V. O. Golub , T. Okuno , V. Novosad. *Origin of fourfold anisotropy in square lattices of circular ferromagnetic dots.* Phys. Rev. B, **74**, 060406(R) (2006).

[100] V. V. Kruglyak , P. S. Keatley , A. Neudert , R. J. Hicken , J. R. Childress , J. A. Katine. *Imaging Collective Magnonic Modes in 2D Arrays of Magnetic Nanoelements.* Phys. Rev. Lett. **104**, 027201 (2010).

[101] S. Saha, R. Mandal, S. Barman, D. Kumar, B. Rana, Y. Fukuma, S. Sugimoto, Y. Otani, and A. Barman. *Tunable magnonic spectra in two-dimensional magnonic crystals with variable lattice symmetry.* Adv. Funct. Mater. **23**, 2378 (2013).

[102] T. Okuno, K. Shigeto, T. Ono, K. Mibu, and T. Shinjo. *MFM study of magnetic vortex cores in circular permalloy dots: behavior in external field.* J. Magn. Magn. Mater. **240**, 1 (2002)

[103] B. V. Waeyenberge, A. Puzic, H. Stoll, K. W. Chou, T. Tyliszczak, R. Hertel, M. Fähnle, H. Brückl, K. Rott, G. Reiss, I. Neudecker, D. Weiss, C. H. Back, and G. Schütz. *Magnetic vortex core reversal by excitation with short bursts of an alternating field.* Nature **444**, 461 (2006).

[104] K. Yamada, S. Kasai, Y. Nakatani, K. Kobayashi, H. Kohno, A. Thiaville, and T. Ono. *Electrical switching of the vortex core in a magnetic disk.* Nat. Mater. **6**, 270 (2007).

[105] S.-K. Kim, K.-S. Lee, Y.-S. Yu, and Y.-S. Choi. *Reliable low-power control of ultrafast vortex-core switching with the selectivity in an array of vortex states by in-plane circular-rotational magnetic fields and spin-polarized currents.* Appl. Phys. Lett. **92**, 022509 (2008).

[106] S. P.-Watelot, J.-V. Kim, A. Ruotolo, R. M. Otxoa, K. Bouzehouane, J. Grollier, A.Vansteenkiste, B.V. de Wiele, V. Cross, and T. Devolder, *Commensurability and chaos in magnetic vortex oscillations.* Nat. Phys. **8**, 682 (2012).

[107] S. Jain, V. Novosad, F. Y. Fradin1, J. E. Pearson, V. Tiberkevich, A. N. Slavin, and S.D. Bader. *From chaos to selective ordering of vortex cores in interacting mesomagnets.* Nat. Commun. **3**, 1330 (2012).

[108] R. Antos, and Y. Otani. *Simulations of the dynamic switching of vortex chirality in magnetic nanodisks by a uniform field pulse.* Phys. Rev. B **80**, 140404 (2009)

[109] S. Yakata, M. Miyata, S. Honda, H. Itoh, H. Wada, and T. Kimura. *Chirality control of magnetic vortex in a square Py dot using current-induced Oersted field.* Appl. Phys. Lett. **99**, 242507 (2011).

[110] M. Jaafar, R. Yanes, D. P. de Lara, O. C.-Fesenko, A. Asenjo, E. M. Gonzalez, J. V. Anguita, M. Vazquez, and J. L. Vicent. *Control of the chirality and polarity of magnetic vortices in triangular nanodots.* Phys. Rev. B **81**, 054439 (2010).

[111] T. J. Silva, C. S. Lee, T. M. Crawford, and C. T. Rogers. *Inductive measurement of ultrafast magnetization dynamics in thin-film permalloy.* J. Appl. Phys. **85**, 7849 (1999).

[112] Z. Q. Qiu and S. D. Bader. *Surface magneto-optic Kerr effect.* Rev. Sci. Instrum. **71**, 1243 (2000).

[113] P. Kasiraj, M. Shelby, J. S. Best, and D. E. Horne. *Magnetic domain imaging with a scanning Kerr effect microscope.* IEEE Trans. Magn. **22**, 837 (1986).

[114] A. Barman, T. Kimura, Y. Otani, Y. Fukuma, K. Akahane, and S. Meguro. *Benchtop time-resolved magneto-optical Kerr Magnetometer.* Rev. Sci. Instrum. **79**, 123905 (2008).

[115] LLG Micromagnetic Simulator, http://llgmicro.home.mindspring.com (1997).

[116] G. Schütz, W. Wagner, W. Wilhelm, P. Kienle, R. Zeller, R. Frahm, and G. Materlik. *Absorption of circularly polarized x rays in iron.* Phys. Rev. Lett. **58**, 737 (1987).

[117] C. T. Chen, F. Sette, Y. Ma, and S. Modesti. *Soft-x-ray magnetic circular dichroism at the $L_{2,3}$ edges of nickel.* Phys. Rev. B **42**, 7262 (1990).

[118] K. S. Buchanan, P. E. Roy, M. Grimsditch, F. Y. Fradin, K. Yu. Guslienko, S. D. Bader, and V. Novosad. *Magnetic-field tunability of the vortex translational mode in micron-sized permalloy ellipses: Experiment and micromagnetic modelling.* Phys. Rev. B **74**, 064404 (2006).

[119] K. S. Buchanan, M. Grimsditch, F. Y. Fradin, S. D. Bader, and V. Novosad. *Driven Dynamic Mode Splitting of the Magnetic Vortex Translational Resonance.* Phys. Rev. Lett. **99**, 267201 (2007).

[120] A. Drews, B. Krüger, G. Selke, T. Kamionka, A. Vogel, M. Martens, U. Merkt, D. Möller, and G. Meier. *Nonlinear magnetic vortex gyration.* Phys. Rev. B **85**, 144417 (2012).

[121] S. Kaka, M. R. Pufall, W. H. Rippard, T. J. Silva, S. E. Russek, and J. A. Katine. *Mutual phase-locking of microwave spin torque nano-oscillators.* Nature. **437**, 389 (2005).

[122] A. Ruotolo, V. Cros, B. Georges, A. Dussaux, J. Grollier, C. Deranlot, R. Guillemet, K. Bouzehouane, S. Fusil, and A. Fert. *Phase-locking of magnetic vortices mediated by antivortices.* Nat. Nanotech. **4**, 528 (2009).

[123] A. D. Belanovsky, N. Locatelli, P. N. Skirdkov, F. A. Araujo, J. Grollier, K. A. Zvezdin, V. Cros, and A. K. Zvezdin. *Phase locking dynamics of dipolarly coupled vortex-based spin transfer oscillators.* Phys. Rev. B **85**, 100409(R) (2012).

[124] D.-S. Han, A. Vogel, H. Jung, K.-S. Lee, M. Weigand, H. Stoll, G. Schütz, P. Fischer, G. Meier, and S.-K. Kim. *Wave modes of collective vortex gyration in dipolar-coupled-dot-array magnonic crystals.* Sci. Rep. **3**, 2262 (2013).

[125] R. Antos, Y. Otani, and J. Shibata. *Magnetic Vortex Dynamics.* J. Phys. Soc. Jpn. **77**, 031004 (2008).

[126] H. Jung, K.-S. Lee, D.-E. Jeong, Y.-S. Choi, Y.-S. Yu, D.-S. Han, A. Vogel, L. Bocklage, G. Meier, M.-Y. Im, P. Fischer, and S.-K. Kim. *Tunable negligible-loss energy transfer between dipolar-coupled magnetic disks by stimulated vortex gyration.* Sci. Rep. **1**, 59 (2011).

[127] C. Liu, C. K. A. Mewes, M. Chshiev, T. Mewes, and W. H. Butler. *Origin of low Gilbert damping in half metals.* Appl. Phys. Lett. **95**, 022509 (2009).

[128] S. Mizukami, D. Watanabe, M. Oogane, Y. Ando, Y. Miura, M. Shirai, and T. Miyazaki. *Low damping constant for Co_2FeAl Heusler alloy films and its correlation with density of states.* J. Appl. Phys. **105**, 07D306 (2009).

[129] A. Dussaux, B. Georges, J. Grollier, V. Cros, A.V. Khvalkovskiy, A. Fukushima, M. Konoto, H. Kubota, K. Yakushiji, S. Yuasa, K.A. Zvezdin, K. Ando, and A. Fert. *Large microwave generation from current-driven magnetic vortex oscillators in magnetic tunnel junctions.* Nat. Commun. **1**, 8 (2010).

Acknowledgements

This work would never have been possible without the fruitful collaborations and the continuous support of many people. I would like to express my sincere gratitude to all of the following:

- Prof. YoshiChika Otani for all his continuous educational and financial supports to make this thesis possible.
- Prof. Christopher Marrows for his agreement to be the second referee of this thesis.
- Prof. Teruo Ono for his agreement to be the second referee of this thesis.
- Ass. Prof. Toshihiro Okamoto for his agreement to be the second referee of this thesis.
- Ass. Prof. Takatsugu Masuda for his agreement to be the second referee of this thesis.
- Ass. Prof. Yasuhiro Fukuma for his continuous support, the excellent guidance, and many fruitful discussions.
- Dr. Yasuhiro Niimi for his continuous support, the excellent guidance, and many fruitful discussions.
- Dr. Shinya Kasai for his continuous support, the excellent guidance of microwave devices, and many fruitful discussions.
- Ass. Prof. Anjan Barman for his great support for developing time resolved-magneto optical Kerr magnetometer, and many fruitful discussions.
- Prof. Takashi Kimura for great support for developing microwave probe station.
- My current and former colleagues Dr. Kohei Ohnishi, Hiroshi Idzuchi, Fujimori Hiroaki, and Norinobu Hasegawa for good and pleasant cooperation in sample fabrication, development of experimental facilities, and many fruitful discussions.
- All the current and former members of Quantum Nano-Scale Magnetism Team and Otani laboratory for the good collaboration and nice atmosphere.
- Dr. Kouichi Akahane and the staff of NEOARK for superb technical assistance of their work on time resolved- magneto optical Kerr magnetometer.
- Dr. Hikota Akimoto and the staff of Emergent Matter Science Research Support Team, CEMS, RIKEN for superb technical assistance for sample fabrications and maintenance of equipment.
- My family and my friends for their patience and the unlimited support at all times.